ADVANCES IN UNCERTAINTY QUANTIFICATION AND INVERSE PROBLEMS IN COMPUTATIONAL MECHANICS

A Dissertation

Presented to the Faculty of the Graduate School

of Cornell University

in Partial Fulfillment of the Requirements for the Degree of

Doctor of Philosophy

by

James E. Warner

May 2014

ADVANCES IN UNCERTAINTY QUANTIFICATION AND INVERSE PROBLEMS IN COMPUTATIONAL MECHANICS

James E. Warner, Ph.D.

Cornell University 2014

This dissertation is composed of three chapters, each of which addresses a specific topic and has been, or is in the process of being published in a research journal. Though relatively diverse, the topics in each chapter fall broadly under the theme of advancing research in uncertainty quantification and inverse problems within the field of computational mechanics. The first chapter is based on the stochastic reduced order model (SROM) concept for propagating uncertainty in engineering simulations. Here, the algorithm for constructing SROMs of random vectors is modified and significantly enhanced, yielding more accurate models in substantially less computational time. The second chapter focusses on inverse material identification in coupled acoustic-structure interaction (ASI) systems using either solid displacement or fluid pressure measurement data. This work represents the first time the modified error in constitutive equation (MECE) approach for inverse problems has been formulated and applied to elasticity imaging problems in ASI. Finally, the third chapter combines elements of the first two chapters and presents a novel approach to solve inverse problems under uncertainty using SROMs. The method provides a practical and efficient means of incorporating the effects of model and measurement uncertainties in inverse estimates of unknown system parameters. At the beginning of each chapter there is a separate abstract that has been prepared for the respective journal publication that introduces each project in detail.

BIOGRAPHICAL SKETCH

James comes from a modest upbringing in the small town of Warwick, New York. The product of a working-class, blue-collar family, he and his sisters represent a proud first generation of college students. After graduating from Warwick Valley High School in 2004, James began his studies at Binghamton University where he majored in Mechanical Engineering. During his tenure at Binghamton, he completed internships as an undergraduate researcher at the National Institute of Standards and Technology (NIST) in 2007 and as a Structural Engineering Intern for the New York State Department of Transportation (NYSDOT) in 2008.

James graduated from Binghamton University in May 2008 and joined Cornell University in August 2008 as a PhD student in Civil and Environmental Engineering. Under the guidance of Dr. Wilkins Aquino, he performed his doctoral research in the areas of uncertainty quantification and inverse problems in the field of computational mechanics. Through coursework and side projects, he also gained considerable expertise in the disciplines of computational science, applied mathematics, and machine learning. In Spring 2012, James relocated with his research group to Duke University, where he completed his PhD as a visiting graduate student. Upon graduating from Cornell University, James will begin his professional career as a Research Computer Engineer at NASA in March 2014.

Grit: The disposition to pursue very long-term goals with passion and perseverance... - A. L. Duckworth

My PhD is dedicated to my family: Mom, Dad, Jess & Ninette,
together raising the bar for our future generations.

ACKNOWLEDGEMENTS

I need to begin by thanking those whose guidance and mentorship was the most instrumental in my journey through graduate school - my doctoral committee. Under the direction of Dr. Mircea Grigoriu, I began my exploration of the areas of uncertainty quantification and stochastic computations, which proved to be the cornerstone of my dissertation and was fundamental in allowing my publication record to take off. It was Dr. David Bindel who helped spark my continuing interest in computer science through both his guidance and the coursework (my two favorite CU courses) I took under him. It is largely because of him that my first job title contains the word "computer", and I could not be happier. Last but certainly not least, I must thank my thesis adviser, Dr. Wilkins Aquino, without his counsel and support over the last five years, my research accomplishments would not be possible. I have grown and gained so much under his guidance and am very thankful to have taken the journey from Ithaca to Durham to continue solving problems together.

I must further thank others who contributed to my academic and intellectual growth: Dr. Steve Koutsourelakis and the Cornell Structural Engineering Department, as well as Manuel Diaz and Swarnavo Sarkar for our research collaboration. I must also give thanks to the Mechanical Engineering Department at Binghamton University, where I truly began my transformation into the knowledge-seeker and problem-solver that I am today.

I am grateful for all the friends I have made along the way - the Fancher Posse of Warwick, NY; the 224 Crew, Back Row Posse, and BUCrew at Binghamton, NY; and the CU/DU CEE grads & CMIP from the final graduate leg.

Finally, much love & thanks to my family, just knowing you were proud was all the fuel I needed to finish this race.

TABLE OF CONTENTS

LIST OF TABLES

LIST OF FIGURES

CHAPTER 1

STOCHASTIC REDUCED ORDER MODELS FOR RANDOM VECTORS: APPLICATION TO RANDOM EIGENVALUE PROBLEMS

Co-authors: Mircea Grigoriu and Wilkins Aquino

Paper published in *Probabilistic Engineering Mechanics*, Volume 31, Pages 1-11, 2013.

Abstract

An improved optimization algorithm is presented to construct accurate reduced order models for random vectors. The stochastic reduced order models (SROMs) are simple random elements that have a finite number of outcomes of unequal probabilities. The defining SROM parameters, samples and corresponding probabilities, are chosen through an optimization problem where the objective function quantifies the discrepancy between the statistics of the SROM and the random vector being modeled. The optimization algorithm proposed shows a substantial improvement in model accuracy and significantly reduces the computational time needed to form SROMs, as verified through numerical comparisons with the existing approach. SROMs formed using the new approach are applied to efficiently solve random eigenvalue problems, which arise in the modal analysis of structural systems with uncertain properties. Analytical bounds are established on the discrepancy between exact and SROM-based solutions for these problems. The ability of SROMs to approximate the natural frequencies and modes of uncertain systems as well as to estimate their dynamics in time is illustrated through comparison with Monte Carlo simulation in

numerical examples.

1.1 Introduction

All physical systems and their corresponding computational models have inherent associated randomness. In practice, this uncertainty manifests itself in the input data (material properties, boundary or initial conditions, etc.) to a deterministic simulation that describes a particular physical system. Understanding and quantifying the impact of uncertainty on the simulation results is critical for successfully characterizing the system response. Despite advances in the field of stochastic computation, it remains a challenge to accurately and efficiently propagate uncertainty in computational models. Generally speaking, this is the problem of characterizing the statistics of the output $\mathbf{Y} \in \mathcal{Y} \subset \mathbb{R}^{d'}$ to a given forward mapping $\mathcal{M}$:

$$\mathcal{M} : \mathcal{X} \mapsto \mathcal{Y} \tag{1.1}$$

with random input parameters $\mathbf{X} \in \mathcal{X} \subset \mathbb{R}^{d}$. We note that models depending on random fields can also be described by this general form after an appropriate parameterization.

The most common and general approach to the solution of Equation (1.1) is Monte Carlo simulation. Monte Carlo is non-intrusive and simple to implement, but due to its slow convergence becomes infeasible for computationally intensive mappings $\mathcal{M}$. Variants such as Latin hypercube sampling and quasi Monte Carlo sampling have been developed to accelerate convergence, but their applicability is often limited [15]. Intrusive approaches such as perturbation methods, operator-based methods (Neumann expansions), and the method of

moments are among common non-sampling techniques. An inherent drawback of these methods is that they are difficult to implement for complex systems and are limited to problems with small magnitudes of uncertainties. Two techniques developed more recently based on generalized polynomial chaos (gPC) expansions [16], the stochastic Galerkin method [2] and the stochastic collocation method [1], have achieved success in several applications ([10],[12],[5],[11]). Stochastic collocation is non-intrusive and therefore easier to implement than the stochastic Galerkin method, but its computational cost grows rapidly with the dimension of the random input.

As a general alternative to these approaches, stochastic reduced order models (SROMs) were introduced in [7] and subsequently applied to determine effective conductivity for random microstructures and to calculate statistics of the states of linear dynamic systems in [8] and [9], respectively. A SROM $\tilde{\mathbf{X}}$ of a random input $\mathbf{X}$ is a random element with a finite and small number of samples which in general are not equally likely. The defining parameters of the SROM, its range and corresponding probabilities, are selected through an optimization problem with an objective function measuring the discrepancy between the statistics of $\tilde{\mathbf{X}}$ and $\mathbf{X}$. Although the ability of SROMs to efficiently solve stochastic problems like Equation (1.1) has been demonstrated, the algorithm employed for SROM construction in these works is suboptimal in that it considers only a finite search space for optimum parameters and results in the need to solve several reduced optimization problems in sequence.

In this work, we propose an improved optimization algorithm for constructing SROMs that results in models that are both formed more efficiently and provide a more accurate representation of the random vector being modeled. The

approach is described in detail and then compared with the existing method in a numerical example illustrating the significant improvement in computational efficiency and accuracy achieved. The performance of SROMs formed with the new algorithm is demonstrated in the solution of random eigenvalue problems with application to modal analysis of structural systems with uncertain properties. We develop analytical bounds on SROM-based solutions to these problems. Furthermore, the ability to approximate the natural frequencies and modes of uncertain systems as well as to estimate their dynamics in time using SROMs is then demonstrated in numerical examples.

Section 2 introduces SROMs and describes both the construction of the models and how they are applied to obtain solutions to general stochastic problems. The newly proposed and existing SROM optimization algorithms are compared and contrasted here. In Section 3, the random eigenvalue problem is formulated and bounds are established on the discrepancy between SROM-based and exact solutions. Section 4 presents results from three numerical examples solved using SROMs. Finally, conclusions are drawn on the effectiveness of the new SROM optimization algorithm and the performance of SROMs for stochastic problems in Section 5.

1.2 Stochastic reduced order models (SROMs)

Let $(\Omega, \mathcal{F}, P)$ and $(\Psi, \mathcal{G})$ denote a probability space and a measurable space, respectively. A function $X : \Omega \mapsto \Psi$ is a random element if it is measurable from $(\Omega, \mathcal{F})$ to $(\Psi, \mathcal{G})$, that is, if $X^{-1}(G) = \{\omega : X(\omega) \in \mathcal{G}\} \in \mathcal{F}, \quad \forall G \in \mathcal{G}$ [6]. In our discussion, $\Psi = \mathbb{R}^d$ and $\mathcal{G} = \mathcal{B}(\mathbb{R}^d)$ is the Borel σ-algebra on $\mathbb{R}^d$, and so

$\mathbf{X} : \Omega \mapsto \mathbb{R}^d$ is a d-dimensional random vector. We will assume that the probability law of $\mathbf{X}$ is fully specified with known expressions for its joint distribution, joint moments, and correlation matrix

$$F(\mathbf{x}) = P\left(\bigcup_{i=1}^{d} X_i \leq x_i\right) \tag{1.2}$$

$$\mu(q_1, ..., q_d) = E\left[\prod_{i=1}^{d} X_i^{q_i}\right] \tag{1.3}$$

$$\mathbf{r} = E[\mathbf{X}\mathbf{X}^T], \tag{1.4}$$

provided the moments of order $q_1 + ... + q_d$ in Equation (1.3) exist and are finite for integers $q_i \geq 0, i = 1, ...d$. Similarly, the expressions for the marginal distributions and moments of order q are denoted as

$$F_i(x_i) = P(X_i \leq x_i) \tag{1.5}$$

$$\mu_i(q) = E[X_i^q] \tag{1.6}$$

1.2.1 Generalities on SROMs

A stochastic reduced order model (SROM) $\tilde{\mathbf{X}}$ for $\mathbf{X}$ is a simple random element with a finite set of samples $\{\tilde{\mathbf{x}}^{(1)}, ..., \tilde{\mathbf{x}}^{(m)}\}$ and corresponding probabilities $(p^{(1)}, ..., p^{(m)})$ such that $p^{(k)} \geq 0 \ \forall k$ and $\sum_{k=1}^{m} p^{(k)} = 1$ [8]. Hence, the SROM $\tilde{\mathbf{X}}$ is completely defined by the model size m and sample-probability pairs $(\tilde{\mathbf{x}}^{(k)}, p^{(k)}), k = 1, ..., m$. With these SROM parameters specified, the distributions and moments of $\tilde{\mathbf{X}}$ corresponding to those of $\mathbf{X}$ given in Equations (1.2) - (1.6) are

$$\tilde{F}(\mathbf{x}) = \sum_{k=1}^{m} p^{(k)} \mathbf{1}(\mathbf{x} \in R^{(k)}) \tag{1.7}$$

$$\tilde{\mu}(q_1, ..., q_d) = \sum_{k=1}^{m} p^{(k)} \left(\prod_{i=1}^{d} (\tilde{x}_i^{(k)})^{q_i} \right) \tag{1.8}$$

$$\tilde{r}(i, j) = \sum_{k=1}^{m} p^{(k)} \tilde{x}_i^{(k)} \tilde{x}_j^{(k)} \tag{1.9}$$

$$\tilde{F}_i(x_i) = \sum_{k=1}^{m} p^{(k)} \mathbf{1} \left(\tilde{x}_i^{(k)} \leq x_i \right) \tag{1.10}$$

$$\tilde{\mu}_i(q) = \sum_{k=1}^{m} p^{(k)} (\tilde{x}_i^{(k)})^q, \tag{1.11}$$

where $R^{(k)} = \times_{i=1}^{d} [\tilde{x}_i^{(k)}, \infty)$ is a rectangle in $\mathbb{R}^d$ and $\mathbf{1}(\cdot)$ is the indicator function. Throughout this study, the shorthand notation used when referring to the SROM samples or probabilities is $\{\tilde{\mathbf{x}}\}$ and $\mathbf{p}$, respectively, in place of $\{\tilde{\mathbf{x}}^{(\mathbf{k})}\}_{k=1}^{m} = \{(\tilde{x}_1^{(1)}, ..., \tilde{x}_d^{(1)}), ..., (\tilde{x}_1^{(m)}, ..., \tilde{x}_d^{(m)})\}$ and $(p^{(1)}, ..., p^{(m)})$.

1.2.2 SROM Construction

According to the definition in the previous section, any m samples of $\mathbf{X}$ with probabilities summing to unity define a SROM $\tilde{\mathbf{X}}$. For practical purposes, however, we seek an optimal reduced order representation of $\mathbf{X}$ by imposing the condition that $\tilde{\mathbf{X}}$ and $\mathbf{X}$ have similar probability laws. Hence, for a given model size m, we choose the defining SROM parameters $\{\tilde{\mathbf{x}}\}$ and $\mathbf{p}$ as the solution to an optimization problem where the objective function quantifies the discrepancy between statistics of $\tilde{\mathbf{X}}$ and $\mathbf{X}$. In this study, we consider an objective function with three components representing differences between SROM and target

marginal distributions, marginal moments up to order $\bar{q} \geq 1$, and correlation matrices

$$e_1(\{\tilde{\mathbf{x}}\}, \mathbf{p}) = \frac{1}{2} \sum_{i=1}^{d} \int_{I_i} \left(\tilde{F}_i(x_i) - F_i(x_i) \right)^2 dx_i \tag{1.12}$$

$$e_2(\{\tilde{\mathbf{x}}\}, \mathbf{p}) = \frac{1}{2} \sum_{i=1}^{d} \sum_{q=1}^{\bar{q}} \left(\frac{\tilde{\mu}_i(q) - \mu_i(q)}{\mu_i(q)} \right)^2 \tag{1.13}$$

$$e_3(\{\tilde{\mathbf{x}}\}, \mathbf{p}) = \frac{1}{2} \sum_{i,j=1; j>i}^{d} \left(\frac{\tilde{r}(i,j) - r(i,j)}{r(i,j)} \right)^2, \tag{1.14}$$

where I_i denotes the support of F_i and the SROM statistics $\tilde{F}_i(x_i)$, $\tilde{\mu}_i(q)$, and $\tilde{r}(i,j)$ have been defined in Equations (1.9)-(1.11).

The optimization problem for the construction of $\tilde{\mathbf{X}}$ is stated as follows

$$\begin{aligned} \tilde{\mathbf{X}} \equiv & \underset{\{\tilde{\mathbf{x}}\}, \mathbf{p}}{\operatorname{argmin}} \left(\sum_{i=1}^{3} \alpha_i e_i(\{\tilde{\mathbf{x}}\}, \mathbf{p}) \right) \\ \text{s.t. } & \sum_{k=1}^{m} p^{(k)} = 1 \text{ and } p^{(k)} \geq 0, \ k = 1, ..., m, \end{aligned} \tag{1.15}$$

where $\{\alpha_i \geq 0\}_{i=1}^{3}$ are weighting factors to ensure that each error component have similar order of magnitude or to emphasize the SROM's ability to represent a particular statistic of $\mathbf{X}$. For example, we can set $\alpha_1 \gg \alpha_2, \alpha_3$ if the marginal distributions of $\mathbf{X}$ need to be represented accurately for a particular application. Note that the model size m is not included in the optimization and is selected beforehand based on computational considerations.

In order to motivate a new approach to SROM construction, we now outline the simplified algorithm to solving the SROM optimization problem in Equation (1.15) as proposed in [8],[9]. First, a collection of n independent samples $\{\mathbf{x}^{(1)}, ..., \mathbf{x}^{(n)}\}$ of $\mathbf{X}$ is generated and stored. It is assumed that n is large enough to accurately characterize the probability law of $\mathbf{X}$. Then, N_X distinct trial subsets of size m are drawn from $\{\mathbf{x}^{(1)}, ..., \mathbf{x}^{(n)}\}$. For each trial subset, the optimization problem in Equation (1.15) is solved for $\mathbf{p}$ while holding the trial samples constant. The defining SROM range $\{\tilde{\mathbf{x}}\}$ is chosen as the trial subset with the smallest optimal value of $\mathbf{e}(\{\tilde{\mathbf{x}}\}, \mathbf{p})$ and the SROM probabilities are set to the corresponding optimum values of $\mathbf{p}$. It is noted that this existing approach is suboptimal since (1) the search space for optimum SROM samples $\{\tilde{\mathbf{x}}\}$ is limited to a finite set, (2) only a relatively small number N_X of subsets of the original set are examined, and (3) the defining SROM parameters $\{\tilde{\mathbf{x}}\}$ and $\mathbf{p}$ are determined sequentially rather than jointly.

In this study we look to achieve improved SROM performance by optimizing over $\{\tilde{\mathbf{x}}\}$ and $\mathbf{p}$ jointly rather than sequentially. In doing so, the ability of $\tilde{\mathbf{X}}$ to accurately represent $\mathbf{X}$ benefits from a search over the entire probability space for SROM samples rather than being limited to a finite subset. In addition to increased accuracy, we also seek to reduce the computation time required for SROM construction. By combining the selection of the defining SROM parameters into one algorithm run, significant computational speedup is expected over the existing approach where N_X reduced optimization problems must be solved.

In order to facilitate the use of efficient gradient-based optimization algorithms, closed-form expressions for derivatives of the objective function with re-

spect to the SROM parameters are now derived. Due to the presence of discontinuities in the SROM cumulative distribution function (CDF) given by Equation (1.10), we must utilize a smooth approximation to $\tilde{F}(x)$ with well-defined derivatives. For this, we use

$$\tilde{F}(x) \approx \tilde{F}^s(x;\sigma) = \sum_{k=1}^{m} \frac{1}{2} p^{(k)} \left(1 + \text{erf}\left(\frac{x - \tilde{x}^{(k)}}{\sqrt{2}\sigma}\right)\right), \tag{1.16}$$

where $\text{erf}(x)$ is the Gauss error function:

$$\text{erf}(x) = \frac{2}{\sqrt{\pi}} \int_0^x e^{-t^2} dt \tag{1.17}$$

Note that we have introduced an additional free parameter σ which controls the degree of smoothing present in $\tilde{F}^s(x;\sigma)$. It can be easily verified that the approximate CDF $\tilde{F}^s$ is monotone increasing, right-continuous, and satisfies $\lim_{x\to-\infty} \tilde{F}^s(x) = 0$ and $\lim_{x\to+\infty} \tilde{F}^s(x) = 1$. Furthermore, $\tilde{F}^s$ becomes equal to the original CDF $\tilde{F}$ as $\sigma \to 0$. The smoothed CDF, however, has the advantage that its derivative with respect to a given SROM sample is well-defined. That is,

$$\frac{\partial \tilde{F}^s}{\partial \tilde{x}_j} = -\frac{p_j}{\sqrt{2\pi\sigma^2}} \exp\left(-\frac{1}{2\sigma^2}\left(x - \tilde{x}_j\right)^2\right) \tag{1.18}$$

Substituting $\tilde{F}^s$ for $\tilde{F}$ in the CDF error component e_1, explicit expressions for the derivatives of the objective function in (1.15) with respect to the SROM parameters can be derived as

$$\frac{\partial}{\partial \tilde{x}_n^{(l)}}[e(\{\tilde{\mathbf{x}}\}, \mathbf{p})] = -\alpha_1 \frac{p^{(l)}}{\sqrt{2\pi\sigma^2}} \int_{I_n} \left(\tilde{F}_n^s(x_n) - F(x_n)\right) \exp\left(-\frac{1}{2\sigma^2}\left(x_n - \tilde{x}_n^{(l)}\right)^2\right) dx_n + \tag{1.19}$$

$$+ \alpha_2 \sum_{q=1}^{\bar{q}} \left(\frac{\tilde{\mu}_q(n) - \mu_q(n)}{\mu_q(n)^2}\right) \left(q p^{(l)} (\tilde{x}_n^{(l)})^{q-1}\right) + \alpha_3 \sum_{i,j=1;j>i}^{d} \left(\tilde{r}(i,j) - r(i,j)\right) p^{(l)} \left(\delta_{in}\tilde{x}_j^{(l)} + \delta_{jn}\tilde{x}_i^{(l)}\right)$$

$$\frac{\partial}{\partial p^{(l)}}[e(\{\tilde{\mathbf{x}}\},\mathbf{p})] = \alpha_1 \frac{1}{2}\sum_{i=1}^{d}\int_{I_i}\left(\tilde{F}_i^s(x_i) - F(x_i)\right)\left(1+\text{erf}\left(\frac{x_i-\tilde{x}_i^{(l)}}{\sqrt{2}\sigma}\right)\right)dx_i + \tag{1.20}$$

$$+\alpha_2\sum_{i=1}^{d}\sum_{q=1}^{\bar{q}}\left(\frac{\tilde{\mu}_q(i)-\mu_q(i)}{\mu_q(i)^2}\right)\left(\tilde{x}_i^{(l)}\right)^q + \alpha_3\sum_{i,j=1;j>i}^{d}\left(\tilde{r}(i,j)-r(i,j)\right)\left(\tilde{x}_i^{(l)}\tilde{x}_j^{(l)}\right)$$

where δ_{ij} is the Kronecker delta.

We note that the most computationally intensive part of the SROM optimization problem defined in (1.15) is the numerical evaluation of the integral appearing in the CDF error term e_1 and its corresponding derivatives. This cost can become especially prohibitive when the CDF support is large or as d and m are increased. Therefore, for larger scale problems, we replace the integral in Equation (1.12) with a summation and evaluate the CDF error pointwise to speed up the optimization using

$$\bar{e}_1 = \frac{1}{2}\sum_{i=1}^{d}\sum_{j=1}^{m}\left(\tilde{F}_i^s(\tilde{x}_i^{(j)}) - F_i(\tilde{x}_i^{(j)})\right)^2 \tag{1.21}$$

We mention that in this case a relatively inaccurate SROM CDF $\tilde{F}_i^s(x)$ may yield a small value for $\bar{e}_1$ and so in practice it can be necessary to increase the value of α_1 in Equation (1.15) to offset this effect.

Example: Beta random variable

In this subsection, the proposed optimization algorithm is used to construct a SROM for a random variable described by a beta probability distribution. The purpose of this simple example is to demonstrate the ability of a SROM with

Percent error in SROM moment estimates					
Moment order	1	2	3	4	5
% Error	0.592	0.244	0.292	0.016	0.074

Table 1.1: SROM moment errors for the beta random variable example.

small model size to represent a given random variable and to compare the accuracy and computational efficiency of the new and previously proposed optimization algorithms. To implement the new approach, the derivatives in Equations (1.19) and (1.20) are supplied to a gradient-based optimization algorithm in MATLAB [13] for the minimization of the objective function in (1.15). Constraints requiring $p^{(k)} \geq 0$, $k = 1, ..., m$, and $\sum_{k=1}^{m} p^{(k)} = 1$ are specified.

The probability density function (pdf) of the beta distribution is

$$f(x; \alpha, \beta) = \frac{x^{\alpha-1}(1-x)^{\beta-1}}{B(\alpha, \beta)}, \quad x \in I = (0, 1), \tag{1.22}$$

where $B(\cdot, \cdot)$ is the beta function and it can be seen that the distribution is fully described by two shape parameters α and β. We examine the SROM for the case where $(\alpha, \beta) = (2, 5)$. The size of the SROM is specified as $m = 5$. We consider moments up to order five ($\bar{q} = 5$) in the moment error component e_2 (Equation (1.13)). The q^{th} moment of a beta random variable is computed as

$$\mu_q = E[X^q] = \frac{B(\alpha + q, \beta)}{B(\alpha, \beta)} \tag{1.23}$$

The CDF and moment error components of the objective function are given equal weight ($\alpha_1 = \alpha_2 = 1$) while the correlation error component is not present in the $1D$ case. The initial guess for the optimization is five independently drawn samples from the beta distribution with equal probability $p = 1/m = 0.2$.

The results from the construction of the beta random variable SROM using

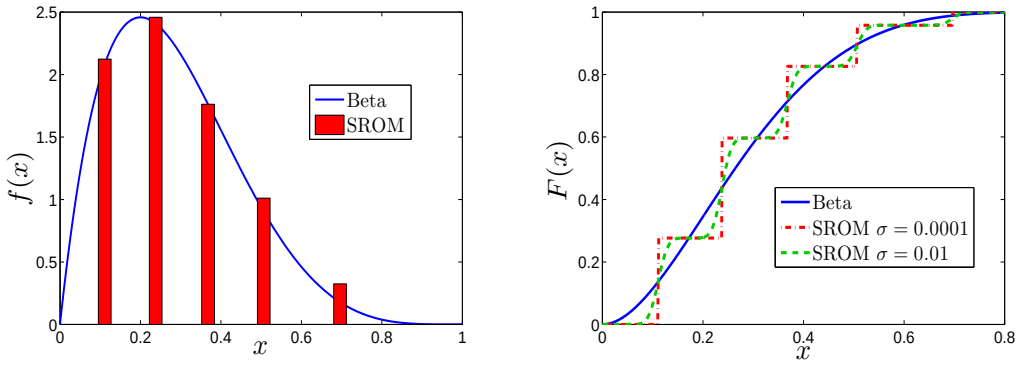

(a) (b)

Figure 1.1: Comparison of the pdf (a) and CDF (b) of the original beta distribution $(\alpha = 2, \beta = 5)$ and the SROM formed by solving Equation (1.15) with $m = 5$. Note: the SROM probabilities in (a) are scaled such that $\max(\mathbf{p}) = \max\{\text{beta pdf}\}$ for illustration.

the newly proposed algorithm are shown in Figure 1.1 and Table 1.1. In Figure 1.1(a), the true beta pdf is plotted verse a bar graph illustrating the defining SROM samples and probabilities chosen via the optimization problem. Note that the height of the bars representing the probability of each sample are scaled such that $\max(\mathbf{p}) = \max\{\text{beta pdf}\}$ for illustration purposes. Figure 1.1(b) compares the true beta CDF and the SROM CDF as computed by Equation (1.16) for the optimum SROM parameters and two different values of the smoothing parameter σ. It is noted that the optimization was performed separately for each value of σ and yielded nearly identical SROM parameters. The percent error between the SROM moments computed by Equation (1.11) and the true moments given in (1.23) are displayed in Table 1.1. It is seen that the error is well below 1% for all five moments and less than 0.1% for the $4th$ and $5th$ moments.

In order to compare the performance of the SROM optimization algorithm with the approach proposed in [8], we now construct a SROM for the beta random variable using this existing framework. All problem parameters specified

above remain unchanged. Recall that in this approach the SROM probabilities $\mathbf{p}$ are chosen to minimize Equation (1.15) for N_X trial subsets of independent samples of X. The subset that results in the smallest objective function value is chosen as the SROM range $\{\tilde{x}\}$. Here, we store the optimum objective function value and CPU time taken to complete the optimization for $N_X = 1 : 1000$. For comparative purposes, we assume the group of N_X trial subsets is grown as N_X increases by first randomly drawing a new subset of size m and then adding it to the previously selected subsets. In this way, we record a new optimum objective function value only when the current subset results in the smallest observed value thus far. Similarly, the CPU time for the current value of N_X is computed as the sum of times for all the previous optimization trials. Due to the random nature of the algorithm, three trials of this experiment are performed and compared with results generated using the new joint optimization approach.

The results comparing CPU times and accuracy of SROMs formed using both optimization algorithms are shown in Figure 1.2(a) and 1.2(b), respectively. The solid line displaying CPU time for the new algorithm (2.16 seconds) is taken as the average from five optimization runs with randomly selected initial SROM ranges. The final objective function value shown in Figure 1.2(b) was the same in each trial. Figure 1.2(a) shows that the existing algorithm takes more CPU time to carry out except in the case of considering only a very small number of trial subsets ($N_X \lesssim 7$). For the value of N_X where the CPU times are roughly equal, it can be seen in Figure 1.2(b) that the optimum objective function value obtained by the new algorithm is about two orders of magnitude smaller than that of the existing algorithm. The figure also shows that none of the three trials of the existing algorithm achieve the same degree of accuracy as the new algorithm when considering up to 1000 trial subsets. It is further noted

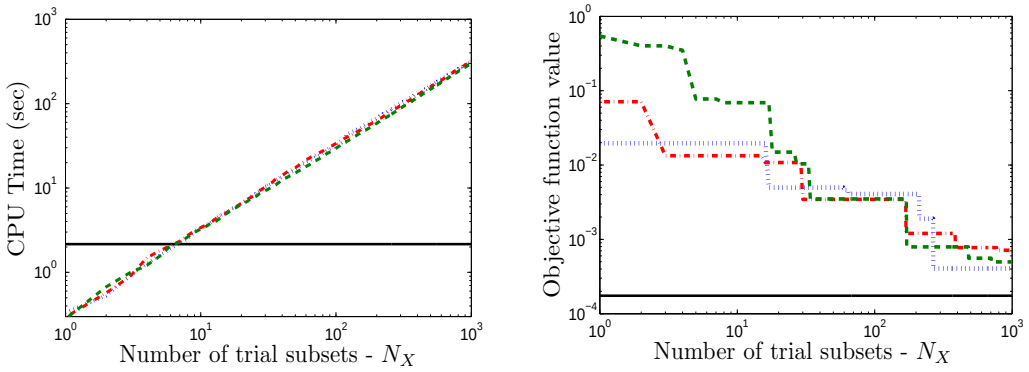

(a) (b)

Figure 1.2: Comparison of the performance of the new SROM optimization algorithm (solid line) versus three trials of the approach proposed in [8] (dashed lines). Figure (a) compares the computation time taken to solve the optimization problem in Equation (1.15), while Figure (b) compares the final objective function value obtained through each algorithm.

that the existing algorithm takes over 100 times longer to perform the optimization when $N_X = 1000$.

The results shown in this section demonstrate the ability of a SROM to provide a satisfactory representation of a random variable with just a small number of defining parameters. Through comparisons with the existing approach, it is seen that the optimization algorithm proposed here for SROM construction provides a substantial improvement in performance. By expanding the search space for the SROM samples from a finite set to the entire support and optimizing jointly over both samples and probabilities, the new algorithm shows a 100-fold improvement in speed and accuracy in this example. The sub-optimal performance of the existing algorithm is most likely a consequence of the SROM range being chosen as independently drawn samples of X. Thus, the samples tend to be clustered in highly likely regions of the range of X without adequate representation for less probable areas. Optimum samples chosen via the new

optimization algorithm, however, are seen to be evenly spread throughout the entire support of X in the results presented.

1.2.3 Solutions by SROMs

For a general stochastic problem given in Equation (1.1), our goal is to use SROMs to efficiently characterize the statistics of the output $\mathbf{Y} \in \mathcal{Y} \subset \mathbb{R}^{d'}$ given the probability law of the random input $\mathbf{X} \in \mathcal{X} \subset \mathbb{R}^d$ and a deterministic mapping $\mathcal{M}$. The construction of a SROM $\tilde{\mathbf{Y}}$ from which the statistics of $\mathbf{Y}$ can be estimated involves two steps. First, a SROM $\tilde{\mathbf{X}}$ is formed for the input $\mathbf{X}$ through the solution of the optimization problem in Equation (1.15). Second, the range for $\tilde{\mathbf{Y}}$ is obtained by evaluating the forward mapping m times with $\mathbf{X} = \tilde{\mathbf{x}}^{(k)}$:

$$\mathcal{M} : \tilde{\mathbf{x}}^{(k)} \mapsto \tilde{\mathbf{y}}^{(k)}, \quad k = 1, ..., m \tag{1.24}$$

This range $\{\tilde{\mathbf{y}}\}$ along with the original set of input SROM probabilities $\mathbf{p}$ define the output SROM $\tilde{\mathbf{Y}}$. The marginal distributions and moments of $\mathbf{Y}$ can then be estimated as

$$E[Y_i^q] \approx E[\tilde{Y}_i^q] = \sum_{k=1}^{m} p^{(k)} (\tilde{y}_i^{(k)})^q \tag{1.25}$$

$$P(Y_i \leq \xi) \approx P(\tilde{Y}_i \leq \xi) = \sum_{k=1}^{m} p^{(k)} \mathbf{1}\left(\tilde{y}_i^{(k)} \leq \xi\right) \tag{1.26}$$

From Equations (1.24) - (1.26) it can be seen that the SROM solution to a stochastic problem requires m forward solves corresponding to the samples of $\tilde{\mathbf{X}}$ which have unequal probability in general. Contrast this with traditional Monte

Percent error in Monte Carlo moment estimates					
Moment order	1	2	3	4	5
Min. % Error	4.17	8.82	2.01	1.63	7.14
Max. % Error	31.11	60.25	92.13	126.28	159.91

Table 1.2: Maximum and minimum percent error for five trials of Monte Carlo moment estimates ($n = 5$) for the beta random variable example.

Carlo solutions, which require n forward solves corresponding to independent, equally likely samples of $\mathbf{X}$. It was seen in the previous example that a 1D beta random variable could be accurately represented by a SROM with just $m = 5$ samples. For comparison, the first five moments of the beta random variable with $(\alpha, \beta) = (2, 5)$ are estimated using Monte Carlo with $n = 5$ samples. The maximum and minimum percent error are computed for five different Monte Carlo trials and displayed in Table 1.2. The moment estimates are both highly inaccurate and unstable as one may expect when using so few samples.

As we will see in later sections, satisfactory SROM-based solutions to random eigenvalue problems are obtained for $m \leq 20$. The advantage of SROM solutions over Monte Carlo for these problems and stochastic problems in general is that they are accurate and stable for $m \ll n$ samples. Thus, a SROM-based approach to Equation (1.1) requires far fewer evaluations of $\mathcal{M}$ but has added overhead for forming the input SROM $\tilde{\mathbf{X}}$. In this light, the benefits in efficiency become more pronounced for computationally intensive forward problems and problems with lower dimensional inputs. Thus, the same stored input SROM can be used to efficiently solve multiple stochastic problems for different combinations of any deterministic problem parameters.

1.3 Random eigenvalue problems by SROMs

In this study, the SROM solution framework is applied to stochastic eigenvalue problems defined by matrices with random entries. A particular application where this problem arises is the modal analysis of structural systems in which the elements of the system have uncertain stiffness given by the components of a random vector $\mathbf{X} \in \mathbb{R}^d$. Here, one is interested in determining the modal frequencies whose squares are the solution to the generalized eigenvalue problem

$$[K]\{\mathbf{V}\} = \Lambda[M]\{\mathbf{V}\} \tag{1.27}$$

where $M \in \mathbb{R}^{d' \times d'}$ and $K \in \mathbb{R}^{d' \times d'}$ are the system mass and stiffness matrix, respectively, and $\mathbf{V} \in \mathbb{R}^{d'}$ is an eigenvector and Λ is an eigenvalue. Since the entries of K are random, so are the modal frequencies of the system. We note that since our intended application is the analysis of discrete structural systems for which the mass matrix is diagonal, the generalized eigenvalue problem in Equation (1.27) reduces to a standard eigenvalue problem in practice. Hence, it will suffice to focus on the problem of estimating a set of eigenvalues $\mathbf{\Lambda} = (\Lambda_1, ..., \Lambda_{d'})$ corresponding to an arbitrary symmetric matrix K with random entries.

As described in Section 2.3, the statistics of the solution to this stochastic eigenvalue problem can be estimated by forming a reduced order model $\tilde{\mathbf{\Lambda}}$ for the eigenvalues $\mathbf{\Lambda}$. After a SROM $\tilde{\mathbf{X}}$ is formed for $\mathbf{X}$, the construction of $\tilde{\mathbf{\Lambda}}$ requires the solution of m deterministic eigenvalue problems defined by $\tilde{k}^{(k)} = K(\tilde{x}^{(k)}), k = 1, ...m$. The statistics of $\mathbf{\Lambda}$ are then approximated using Equations (1.25) and (1.26). In this section we study the accuracy of SROM approximations of random eigenvalues by developing analytical bounds on the discrepancy between SROM and exact eigenvalue solutions. In the subsequent

applications section, the accuracy of SROM-based eigenvalue solutions are verified numerically through the modal analysis of two different structural systems.

1.3.1 Accuracy of SROM-based solutions

The relative accuracy of the SROM $\tilde{\mathbf{X}}$ can be evaluated straightforwardly by using the objective function $\mathbf{e}(\{\tilde{\mathbf{x}}\}, \mathbf{p})$ as a metric. The performance of the SROM $\tilde{\mathbf{\Lambda}}$ for $\mathbf{\Lambda}$, however, depends on both the discrepancy between $\tilde{\mathbf{X}}$ and $\mathbf{X}$ and the mapping $\mathbf{X} \mapsto \mathbf{\Lambda}$. Hence, the SROM $\tilde{\mathbf{\Lambda}}$ corresponding to an accurate $\tilde{\mathbf{X}}$ can be unsatisfactory because of the complexity of this mapping. To gauge the performance of $\tilde{\mathbf{\Lambda}}$, we develop bounds on the discrepancy between $\tilde{\mathbf{\Lambda}}$ and $\mathbf{\Lambda}$ that depend on both the accuracy of $\tilde{\mathbf{X}}$ and the mapping $\mathbf{X} \mapsto \mathbf{\Lambda}$. To do so, we first obtain bounds on the discrepancy between eigenvalues of two distinct deterministic matrices. The bounds are then extended to the case of matrices with random entries in the following subsection.

Deterministic eigenvalue bounds

Consider the following deterministic eigenvalue problems

$$A\mathbf{v} = \lambda \mathbf{v} \tag{1.28}$$

$$\hat{A}\hat{\mathbf{v}} = \hat{\lambda}\hat{\mathbf{v}}, \tag{1.29}$$

where $A, \hat{A} \in \mathbb{R}^{d' \times d'}$ and we define the matrix $D \equiv \hat{A} - A$ as a finite perturbation to A. Our objective is to bound the discrepancy between the eigenvalues of A and $\hat{A}$ in terms of the size of the perturbation D. Given that the main application

considered involves finding natural frequencies and modes of stochastic linear dynamic systems that result from symmetric eigenvalue problems, it will suffice to focus on bounds case where A and D are symmetric. It is well known that these bounds are tighter and more informative than the general non-symmetric case. Two bounds are stated here: the first addresses the difference in the whole set of d' eigenvalues of $\hat{A}$, while the second addresses the difference in one particular eigenvalue.

First bound (*Wielandt-Hoffman Theorem*):

If $(\lambda_1, ..., \lambda_{d'})$ and $(\hat{\lambda}_1, ..., \hat{\lambda}_{d'})$ are the eigenvalues of the symmetric matrices A and $\hat{A} = A + D$, respectively, then

$$\sum_{i=1}^{d'} (\hat{\lambda}_i - \lambda_i)^2 \leq ||D||_F^2 \tag{1.30}$$

where $|| \cdot ||_F$ is the Frobenius norm. The proof can be found in Section 3 of [14].

Second bound (*Weyl's Theorem*):

If $(\lambda_1, ..., \lambda_{d'})$ and $(\hat{\lambda}_1, ..., \hat{\lambda}_{d'})$ are the eigenvalues of the symmetric matrices A and $\hat{A} = A + D$, respectively, then

$$|\hat{\lambda}_k - \lambda_k| \leq ||D||_2 \tag{1.31}$$

for $k = 1 : d'$. Or equivalently

$$\max_k |\hat{\lambda}_k - \lambda_k| \leq ||D||_2 \tag{1.32}$$

The proof can be found in Section 5.2 of [4].

Stochastic eigenvalue bounds

The deterministic eigenvalue bounds presented previously are now used to provide measures of accuracy on SROM-based solutions to stochastic eigenvalue problems. We begin with bounds on the discrepancy between the SROM eigenvalue estimate $\tilde{\mathbf{\Lambda}}$ and corresponding Monte Carlo approximation, denoted as $\widehat{\mathbf{\Lambda}}$. For the purpose of this exposition, let us suppose we have a collection of independent samples $\{\mathbf{x}^{(i)}\}_{i=1}^{n}$ of $\mathbf{X}$. Here, it is assumed n is large enough to characterize the probability law of $\mathbf{X}$ satisfactorily. Let $\tilde{\mathbf{X}}$ be an SROM of size $m \ll n$ defined by samples $\{\tilde{\mathbf{x}}^{(k)}\}_{k=1}^{m}$ and probabilities $(p^{(1)}, ..., p^{(m)})$. We make the simplifying assumption that $\{\tilde{\mathbf{x}}^{(k)}\}_{k=1}^{m}$ are a subset of the Monte Carlo samples $\{\mathbf{x}^{(i)}\}_{i=1}^{n}$.

First, we would like to bound the difference in eigenvalue solutions corresponding to a single Monte Carlo and SROM sample using the deterministic bounds in Section 3.1.1. We assume K is a symmetric matrix whose entries are a function of the components of $\mathbf{X}$. Let $\mathcal{K}^{(i)}$ and $\tilde{\mathcal{K}}^{(k)}$ denote two versions of this matrix formed corresponding to the Monte Carlo sample $\mathbf{x}^{(i)}$ and the SROM sample $\tilde{\mathbf{x}}^{(k)}$, respectively. If $\boldsymbol{\lambda}^{(i)}$ are the eigenvalues corresponding to $\mathcal{K}^{(i)}$ and $\tilde{\boldsymbol{\lambda}}^{(k)}$ are the eigenvalues corresponding to $\tilde{\mathcal{K}}^{(k)}$, we can use Equation (1.30) to bound the discrepancy in these sets of eigenvalues as

$$||\tilde{\boldsymbol{\lambda}}^{(k)} - \boldsymbol{\lambda}^{(i)}||_2 \leq ||\tilde{\mathcal{K}}^{(k)} - \mathcal{K}^{(i)}||_F, \tag{1.33}$$

where we have let $D = \tilde{\mathcal{K}}^{(k)} - \mathcal{K}^{(i)}$ be the perturbation matrix in this case. Similarly, if we are concerned with the discrepancy between one eigenvalue in particular, we can use Equation (1.31) to write

$$|\tilde{\lambda}_j^{(k)} - \lambda_j^{(i)}| \leq ||\tilde{\mathcal{K}}^{(k)} - \mathcal{K}^{(i)}||_2 \tag{1.34}$$

We now introduce a partition to the collection of samples $\{\mathbf{x}^{(i)}\}_{i=1}^n$ in order to use (1.33) and (1.34) to derive bounds on $E[||\tilde{\mathbf{\Lambda}} - \widehat{\mathbf{\Lambda}}||_2]$ and $E[|\tilde{\Lambda}_j - \widehat{\Lambda}_j|]$. Denote this partition as $\{\mathcal{I}_k, k = 1, ..., m\}$ where each set $\mathcal{I}_k$ contains n_k samples and has a nuclei at the SROM sample $\tilde{\mathbf{x}}^{(k)}$. Samples from $\{\mathbf{x}^{(i)}\}_{i=1}^n$ are placed in a given cluster $\mathcal{I}_k$ based on their proximity to $\tilde{\mathbf{x}}^{(k)}$ and are distributed in such a way that the relation $p^{(k)} = n_k/n$ is satisfied approximately for $k = 1, ..., m$. In this way, the probability that $\mathbf{X}$ is represented by a Monte Carlo sample that lies in cluster $\mathcal{I}_k$ is $n_k/n \approx p^{(k)}$ An algorithm to construct a partition with these properties was proposed in [8].

With such a partition in place, we can compute $E[||\tilde{\mathbf{\Lambda}} - \widehat{\mathbf{\Lambda}}||_2]$ as a weighted average of this discrepancy in each cluster of the partition

$$\begin{aligned} E\left[||\tilde{\mathbf{\Lambda}} - \widehat{\mathbf{\Lambda}}||_2\right] &= \sum_{k=1}^{m} p^{(k)} \left(\frac{1}{n_k} \sum_{\mathbf{x}^{(i)} \in \mathcal{I}_k} ||\tilde{\boldsymbol{\lambda}}^{(k)} - \boldsymbol{\lambda}^{(i)}||_2 \right) \\ &\approx \frac{1}{n} \sum_{k=1}^{m} \sum_{\mathbf{x}^{(i)} \in \mathcal{I}_k} ||\tilde{\boldsymbol{\lambda}}^{(k)} - \boldsymbol{\lambda}^{(i)}||_2 \\ &\leq \frac{1}{n} \sum_{k=1}^{m} \sum_{\mathbf{x}^{(i)} \in \mathcal{I}_k} ||\tilde{\mathcal{K}}^{(k)} - \mathcal{K}^{(i)}||_F, \end{aligned} \tag{1.35}$$

where we have used $p^{(k)} \approx n_k/n$ in the second equality and the bound in (1.33) for the final inequality. The same arguments can be made for $|\tilde{\Lambda}_j - \widehat{\Lambda}_j|$. Consequently, we have that the moments of order q of $||\tilde{\mathbf{\Lambda}} - \widehat{\mathbf{\Lambda}}||_2$ and $|\tilde{\Lambda}_j - \widehat{\Lambda}_j|$ satisfy the following inequalities

$$E\left[||\tilde{\mathbf{\Lambda}} - \widehat{\mathbf{\Lambda}}||_2^q\right] \leq \frac{1}{n}\sum_{k=1}^{m}\sum_{\mathbf{x}^{(i)}\in\mathcal{I}_k}\left(||\tilde{\mathcal{K}}^{(k)} - \mathcal{K}^{(i)}||_F\right)^q \tag{1.36}$$

$$E\left[|\tilde{\Lambda}_j - \widehat{\Lambda}_j|^q\right] \leq \frac{1}{n}\sum_{k=1}^{m}\sum_{\mathbf{x}^{(i)}\in\mathcal{I}_k}\left(||\tilde{\mathcal{K}}^{(k)} - \mathcal{K}^{(i)}||_2\right)^q \tag{1.37}$$

We note that as $m \to n$, the radius of each set $\mathcal{I}_k$ approaches zero. As a result, each $\mathcal{I}_k$ contains only its nucleus $\tilde{\mathbf{x}}^{(k)}$ and $n_k \to 1$. Hence, the SROM-based solution approaches the Monte Carlo solution in this limit case since both use the same samples of $\mathbf{X}$ and the probabilities $p^{(k)}$ converge to $1/n$.

With regard to an exact solution $\mathbf{\Lambda}$ to a stochastic eigenvalue problem, we can characterize the discrepancy of the SROM-based approximation $\tilde{\mathbf{\Lambda}}$ as

$$E\left[||\tilde{\mathbf{\Lambda}} - \mathbf{\Lambda}||_2^q\right] \leq E\left[||\tilde{\mathbf{\Lambda}} - \widehat{\mathbf{\Lambda}}||_2^q\right] + E\left[||\widehat{\mathbf{\Lambda}} - \mathbf{\Lambda}||_2^q\right] \tag{1.38}$$

Since $\tilde{\mathbf{\Lambda}}$ approaches $\widehat{\mathbf{\Lambda}}$ as $m \to n$ and Monte Carlo estimates $\widehat{\mathbf{\Lambda}}$ converge to $\mathbf{\Lambda}$ as $n \to \infty$, we can see that the expectation of the difference between $\mathbf{\Lambda}$ and $\tilde{\mathbf{\Lambda}}$ converges to 0 in this limit case. We note that while the relative performance of two distinct input SROMs $\tilde{\mathbf{X}}$ can be effectively gauged by comparing the optimum objective function values in Equation (1.15) corresponding to each model, the bounds in Equations (1.36) - (1.38) provide less explicit information on the quality of SROM solutions $\tilde{\mathbf{\Lambda}}$. These bounds are less sharp in the sense that they do not address convergence rate and because the asymptotic convergence argument above is not as useful in practice since $m \ll n$ in general. Development of analytical measures on the rates of convergence of $\tilde{\mathbf{\Lambda}}$ to $\mathbf{\Lambda}$ is beyond the scope of this study.

1.4 Applications

The SROM solution framework is now applied in several numerical examples. We demonstrate the performance of SROM-based solutions to stochastic eigenvalue problems through two examples involving the modal analysis of uncertain structural systems. The first analyzes a simple shear-frame idealization of a structure while the second considers a more general planar frame model. For the shear-frame model, we also consider the uncertain dynamics of the system and use SROMs to estimate the statistics of its evolution in time. We conclude the section with a numerical example illustrating one of the open research issues associated with the SROM-based approach to stochastic problems.

1.4.1 Shear-frame model

Consider a structure with N_s stories modeled by a planar frame of width $2L$ and height $N_s L$. In this section, we examine the highly idealized case where the beams of the structure are assumed to be rigid and we neglect both the joint rotations and the axial deformation of the beams and columns. These assumptions result in the shear-frame or shear-beam model commonly used in structural engineering [3]. The mass is idealized as concentrated at the floor levels and thus there are N_s degrees of freedom $(U_1, ..., U_{N_s})$ corresponding to the relative horizontal motion of each lumped mass `M`. Here, we assume the combined lateral stiffness of the columns connecting each story is uncertain and given by the components of the random vector $\mathbf{X} \in \mathbb{R}^d$ where $d = N_s$. The stiffness matrix for this simplified system is tridiagonal and has the general form

$$K = \begin{bmatrix} X_1 + X_2 & -X_2 & \cdots & 0 \\ -X_2 & X_2 + X_3 & \cdots & 0 \\ \vdots & \vdots & \ddots & -X_d \\ 0 & 0 & -X_d & X_d \end{bmatrix} \tag{1.39}$$

while the diagonal mass matrix is given by

$$M = \text{diag}(\mathtt{M}, \mathtt{M}, ..., \mathtt{M}/2) \in \mathbb{R}^{d \times d} \tag{1.40}$$

Let us suppose that $\mathbf{X}$ is a translation random vector with coordinates

$$X_i = F^{-1} \circ \Phi(G_i), \quad i = 1, ..., d, \tag{1.41}$$

where F is a shifted gamma distribution with shift, shape, and decay parameters $a = 1$, $k = 2$, and $\lambda = 3$, respectively. The vector $\mathbf{G} = (G_1, ..., G_d)$ is an $\mathbb{R}^d$-valued Gaussian variable with coordinates G_i of mean 0, variance 1, and correlations given by

$$E[G_i G_j] = \rho^{|i-j|}, \ \rho \in [0, 1] \tag{1.42}$$

Modal analysis

Our goal in this section is to estimate the statistics of the eigenvalues $\mathbf{\Lambda} = (\Lambda_1, ..., \Lambda_d)$ of the matrix $\hat{K} = M^{-1}K$ by forming the reduced model $\tilde{\mathbf{\Lambda}}$, as described in Section 3. We reiterate that these eigenvalues represent the square root of the system's modal frequencies. Using Equations (1.25) and (1.26) we compute the distribution and moment of order q of $\tilde{\Lambda}_i$ as $P(\tilde{\Lambda}_i \leq \xi) =$

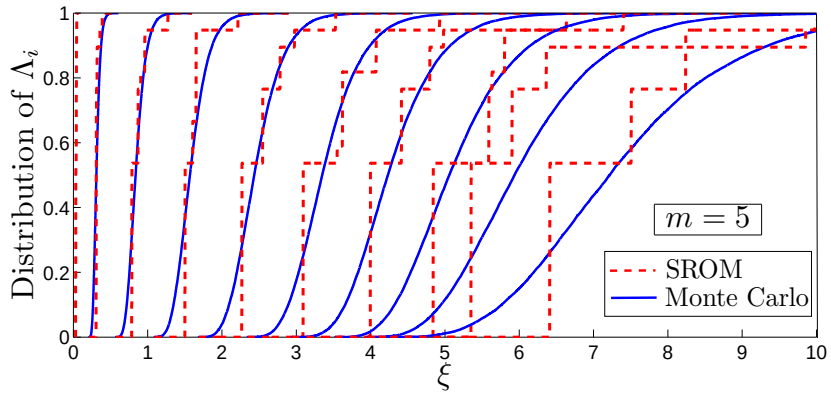

(a)

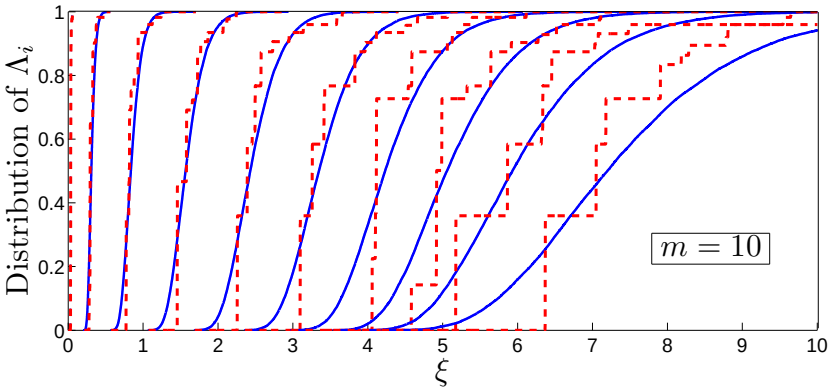

(b)

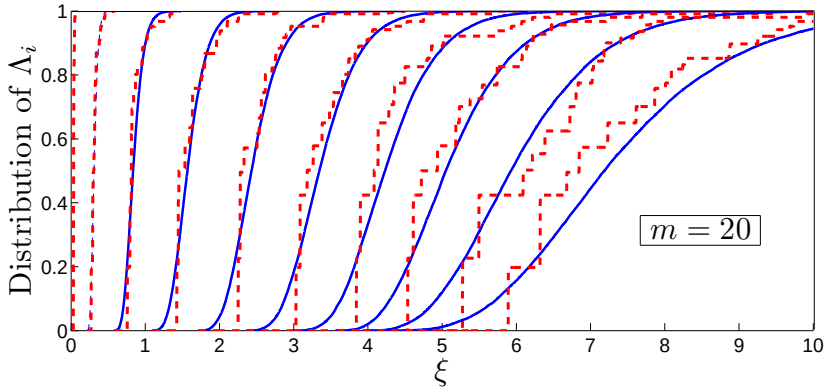

(c)

Figure 1.3: Estimates of the distributions of $\Lambda_i, i = 1, ..., 10$ in Example 4.1.1. The SROM approximations (dashed line) for (a)$m = 5$, (b)$m = 10$, and (c)$m = 20$ are compared with the Monte Carlo solution (solid line) using 10,000 samples.

SROM moment and CDF error in Example 4.1.1						
Model size (m)	ϵ_1	ϵ_2	ϵ_3	ϵ_4	$\bar{\epsilon}_M$	$\bar{\epsilon}_{CDF}$
5	2.81	5.17	9.36	14.44	4.02	2.60e-2
10	2.44	6.36	11.33	16.93	2.90	2.00e-2
20	3.18	6.40	10.09	13.99	2.71	1.25e-2

Table 1.3: SROM moment and CDF errors as defined in Equations (1.43)-(1.45) for Example 4.1.1.

$\sum_{k=1}^{m} p^{(k)} \mathbf{1}(\tilde{\lambda}_i^{(k)} \leq \xi)$ and $E[\tilde{\Lambda}_i^q] = \sum_{k=1}^{m} p^{(k)} (\tilde{\lambda}_i^{(k)})^q$, respectively. We also seek mean estimates of the eigenvectors of $\hat{K}$ representing the modes of the shear-frame model. To gauge the accuracy of the SROM-based solutions, we compare with Monte Carlo solutions computed from 10,000 independent realizations of $\hat{K}$. It is noted that a similar problem is solved in [7] for the case when $d = 3$. Here, we study the performance of the new optimization algorithm for larger scale problems by letting $d = 10$.

The error metrics we use to quantify accuracy of the SROM solutions will be the maximum percent error in moments for each order, the average percent error in all moments, and the average absolute error in CDFs:

$$\epsilon_q = 100 \times \max_i \left[\frac{|E[\tilde{\Lambda}_i^q] - E[\Lambda_i^q]|}{E[\Lambda_i^q]} \right], \; q = 1, ..., \bar{q} \tag{1.43}$$

$$\bar{\epsilon}_M = 100 \times \left(\frac{1}{d'\bar{q}} \right) \sum_{i=1}^{d'} \sum_{q=1}^{\bar{q}} \left[\frac{|E[\tilde{\Lambda}_i^q] - E[\Lambda_i^q]|}{E[\Lambda_i^q]} \right] \tag{1.44}$$

$$\bar{\epsilon}_{CDF} = \frac{1}{d'} \sum_{i=1}^{d'} \int_{I_i} \left(\tilde{F}_{\tilde{\Lambda}_i}(\xi_i) - F_{\Lambda_i}(\xi_i) \right)^2 d\xi_i \tag{1.45}$$

Results are generated for the case when $\rho = 0.5$ for three different SROM sizes $m = 5, 10, 20$. We consider moments up to order $\bar{q} = 4$ when forming the SROM

$\tilde{\mathbf{X}}$ and set the weighting factors in Equation (1.15) as $(\alpha_1, \alpha_2, \alpha_3) = (1e2, 1, 1)$. We choose a larger value for α_1 since we are evaluating the CDF error pointwise as in Equation (1.21) and hence a small error value can be achieved even if the SROM CDF is relatively inaccurate. The smoothing parameter of the SROM CDF in all results is set as $\sigma = 0.001$.

The distributions of $\tilde{\Lambda}_i$ and Λ_i as computed with Monte Carlo are compared in Figure 1.3 for $m = 5, 10, 20$. It is seen that we obtain accurate approximate distributions, even for a small model size of $m = 5$. The accuracy is especially prominent for the lower order eigenvalues with smaller variance, and it improves, generally, as m increases. The SROM moment and CDF errors, as computed in Equations (1.43) - (1.45), are displayed in Table 1.3 for the different model sizes tested. The maximum moment errors remain similar for the different model sizes while the average moment and CDF errors decrease as m increases. We note that the maximum moment errors occur for each case in estimates of the largest system eigenvalue. We can see by the values of $\bar{\epsilon}_M$, however, that the error in each moment is typically much smaller than the maximum values observed. Figure 1.4 shows the mean estimates of the eigenvectors of $\hat{K}$ using both Monte Carlo and SROMs for the case when $m = 20$, it is seen that the SROM estimates show excellent agreement.

Uncertain dynamics

In this section, we consider the dynamics of the shear-frame model with uncertain stiffness described above. We demonstrate the ability of SROMs to accurately estimate the statistics of the evolution of displacement in the structure in time under harmonic loading. The motion of the horizontal degrees of freedom

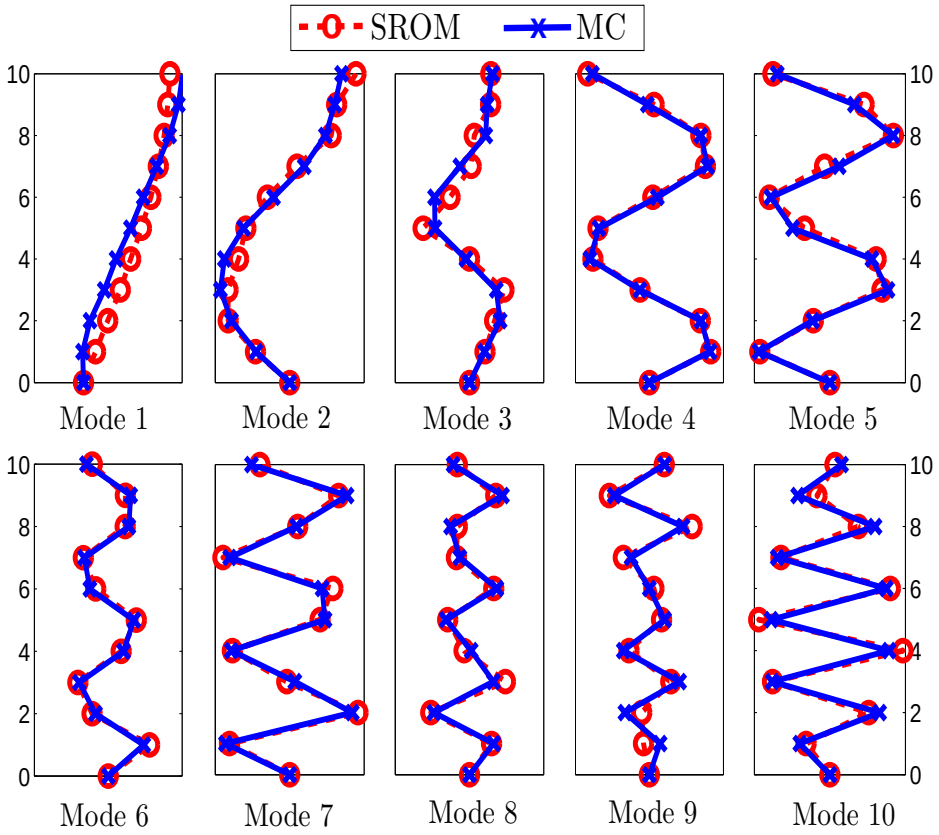

Figure 1.4: Mean estimates for the modes in Example 4.1.1 computed using SROMs ($m = 20$) and Monte Carlo (10,000 samples)

SROM moment errors in Example 4.1.2				
Order (q)	1	2	3	4
$i = 1$	0.30	0.54	1.47	3.03
$i = 2$	0.43	1.76	2.18	3.35
$i = 3$	0.30	1.35	2.15	3.62

Table 1.4: SROM moment errors as defined in (1.47)

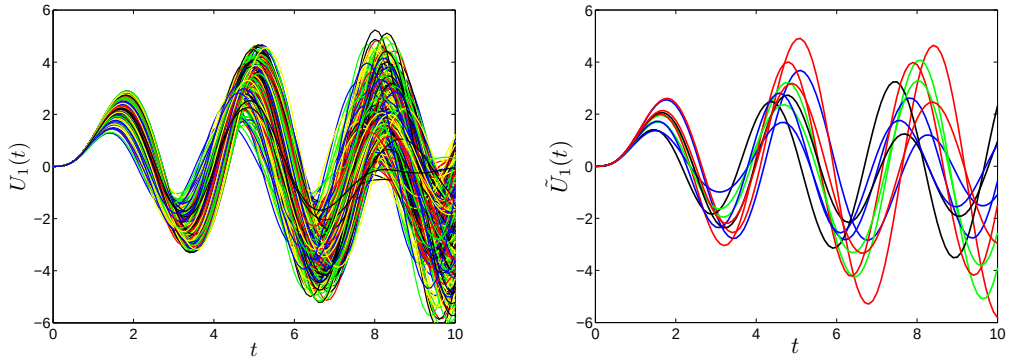

(a) (b)

Figure 1.5: Samples of $U_1(t)$ (left) and $\tilde{U}_1(t)$ (right).

$\mathbf{U} = (U_1, ..., U_{Ns})$ is governed by

$$M\ddot{\mathbf{U}} + C\dot{\mathbf{U}} + K\mathbf{U} = \mathbf{P} \tag{1.46}$$

where K and M for the shear frame are given in Equations (1.39) and (1.40), respectively. The damping matrix C is estimated using the Caughey damping model (Section 11.4.2 [3]) with a damping ratio of 5% prescribed for each of the system modes.

We examine the case where the structure has three stories ($N_s = 3$) and again the floor stiffnesses are described by the shifted gamma distribution in Equation (1.41) with the defining parameters unchanged from the previous section. We assume the frame is initially at rest when a force $P_1 = 5\sin(2t)$ is applied to the first story. Here, we seek the statistics of the motion of each degree of freedom from $t_0 = 0s$ to $t_f = 10s$. A SROM $\tilde{\mathbf{X}}$ of size $m = 10$ is formed for $\mathbf{X}$ and the corresponding SROM $\tilde{\mathbf{U}}(t)$ of $\mathbf{U}(t)$ is constructed by solving Equation (1.46) with $\mathbf{X} = \tilde{\mathbf{x}}^{(k)}, k = 1, ..., m$. We compare the SROM-based solution with the Monte Carlo solution using 1000 independent samples of $\mathbf{X}$.

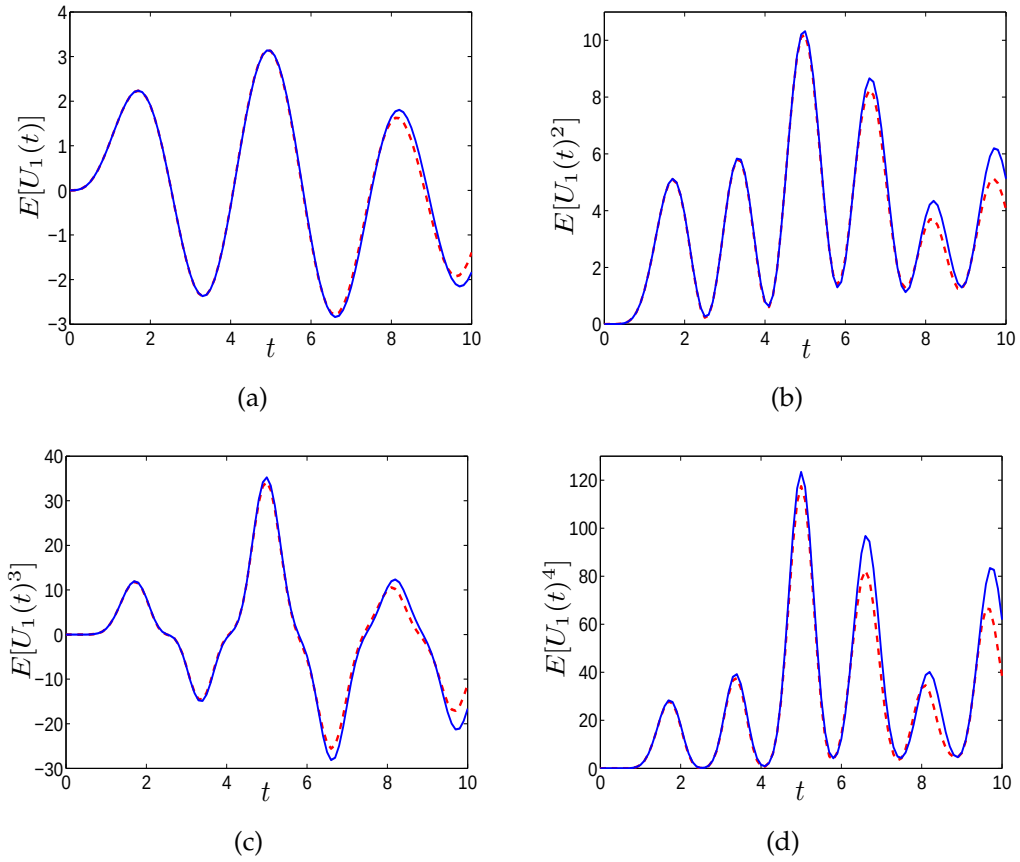

Figure 1.6: Estimates of the first four moments of $U_1(t)$ computed using the SROM (dashed) and Monte Carlo (solid) in Example 4.1.2.

Figure 1.5(a) shows 1,000 independent Monte Carlo samples of the solution $U_1(t)$ representing the motion of the first degree of freedom. Figure 1.5(a) shows the ten samples $(\tilde{u}_1^{(1)}(t), ..., \tilde{u}_1^{(m)}(t)))$ making up the range of $\tilde{U}_1(t)$ for comparison. The first four moments of $U_1(t)$ computed using the SROM $\tilde{U}_1(t)$ are plotted in Figure 1.6 against the Monte Carlo estimates. The SROM-based approximations for each moment show excellent agreement and are nearly identical for $t < 5s$. To demonstrate the accuracy of the SROM-based moments for the remaining degrees of freedom, the percent error in each moment is computed using

$$\varepsilon_i(q) = 100 \times \frac{\int_{t_o}^{t_f} \left(E[U_i(t)^q] - E[\tilde{U}_i(t)^q] \right)^2 dt}{\int_{t_o}^{t_f} \left(E[U_i(t)^q] \right)^2 dt} \tag{1.47}$$

and is displayed in Table 1.4. It is seen that the error for moments up to order four in each degree of freedom is less than 4% while the error in the mean estimates is well below 1%.

1.4.2 Modal analysis of a general planar frame

In this example, we relax some of the simplifying assumptions made for the shear-frame model and consider a more general planar frame model of a structure with N_s stories. Specifically, we no longer assume that the beams in the frame are rigid and hence allow for non-zero joint rotations $(\theta_{1,1}, \theta_{1,2}, ..., \theta_{N_s,2})$ in addition to the horizontal displacements $(U_1, ..., U_{N_s})$. In doing so, we now allow the stiffness in each member of the frame to vary randomly rather than assigning one value to characterize the lateral stiffness of each level. For this analysis, we assign a value for the Young's modulus of each member as

$$\mathcal{E}_i = a + bX_i, \quad i = 1, ..., d \tag{1.48}$$

with $(a, b) = (2, 3)$ and where X_i is given by Equation (1.41) with F as a beta distribution having shape parameters $(\alpha, \beta) = (2, 5)$. The components of $\mathbf{G}$ again have mean 0, variance 1, and correlations given by Equation (1.42). We assume unit values for the moment of inertia in each member as well as the story height L and mass `M`.

Again, we are interested in the natural frequencies and mode shapes of this system through the solution of the eigenvalue problem in Equation (1.27). For

the general planar frame considered here, the mass and stiffness matrices can be partitioned as

$$M = \begin{bmatrix} M_{11} & 0 \\ 0 & 0 \end{bmatrix}, \quad K = \begin{bmatrix} K_{11} & K_{12} \\ K_{21} & K_{22} \end{bmatrix} \tag{1.49}$$

where the 11 and 22 blocks of the matrices correspond to the translational and rotational degrees of freedom, respectively. Through a static condensation procedure, Equation (1.27) reduces to finding the eigenvalues $\mathbf{\Lambda} = (\Lambda_1, ..., \Lambda_{d'})$ of the matrix $\bar{K} = M_{11}^{-1}(K_{11} - K_{12}K_{22}^{-1}K_{21})$. We note that while M_{11} has the same form as Equation (1.40), the stiffness matrix K lacks special structure and does not possess a straightforward expression in terms of an arbitrary number of stories in this case.

We examine the case where the frame has four stories and so $d = 12$. Since we are neglecting rotational inertia, there are four frequencies and modes ($d' = 4$) corresponding to the structure's horizontal degrees of freedom. We generate results for SROM sizes $m = 10, 20$ and for correlation coefficients $\rho = 0.2, 0.9$ in Equation (1.42). The objective function weights and smoothing parameter are assigned as $(\alpha_1, \alpha_2, \alpha_3) = (1e2, 1, 1)$ and $\sigma = 0.001$, respectively. We once again employ the error metrics in Equations (1.43) - (1.45) to gauge SROM accuracy using Monte Carlo simulation with 10,000 samples as the reference solution.

The errors in the SROM approximations for the moments and distributions of Λ_i are displayed in Table 1.5 for each combination of model size and correlation coefficient. It can be seen that the SROM estimates are more accurate for a higher correlation coefficient value and the average moment and CDF errors decrease for a larger model size m as expected. The decrease in error is more

SROM moment and CDF error in Example 4.2							
	m	ϵ_1	ϵ_2	ϵ_3	ϵ_4	$\bar{\epsilon}_M$	$\bar{\epsilon}_{CDF}$
$\rho = 0.2$	10	15.00	14.49	13.17	5.38	4.10	3.35e-1
	20	15.26	3.77	17.30	11.87	3.46	1.09e-1
$\rho = 0.9$	10	10.74	13.27	9.74	5.50	3.60	4.30e-1
	20	0.79	6.25	13.03	17.12	2.78	1.97e-1

Table 1.5: SROM moment and CDF errors as defined in Equations (1.43)-(1.45) for Example 4.2.

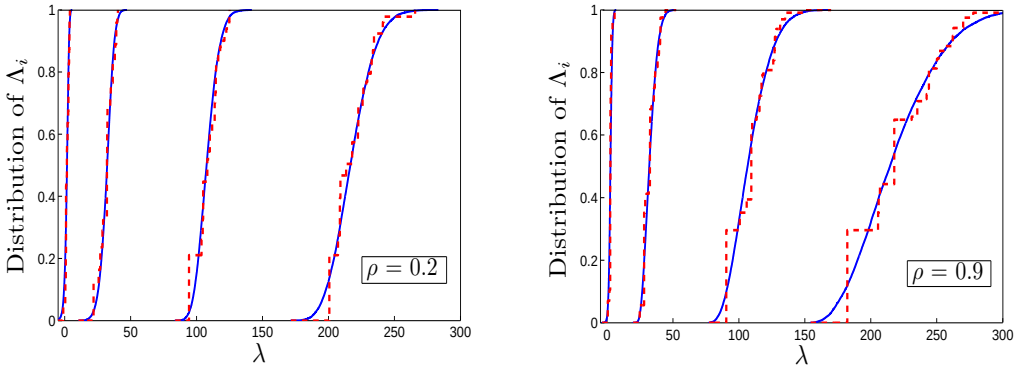

(a) (b)

Figure 1.7: Estimates of the distributions of $\Lambda_i, i = 1, ..., 4$ in Example 4.2. The SROM approximation (dashed line) with $m = 20$ is compared with the Monte Carlo solution (solid line) using 10,000 samples for $\rho = 0.2$ and $\rho = 0.9$.

pronounced in the distribution estimates as the SROM size is increased from $m = 10$ to $m = 20$. The SROM estimates for the distributions of Λ_i with $m = 20$ are compared with the Monte Carlo solution for the case of $\rho = 0.2$ and $\rho = 0.9$ in Figures 1.7(a) and 1.7(b), respectively. The approximate distributions for each eigenvalue show excellent agreement in both cases. Finally, the mean estimates for the modes of the structure using SROMs can be seen in Figure 1.8 for the case where $m = 10$ and $\rho = 0.9$. The approximate modes using SROMs are nearly identical to those computed using Monte Carlo with 10,000 samples.

For comparative purposes, the accuracy of eigenvalue moment estimates using Monte Carlo with 20 independent samples is examined. For $\rho = 0.9$, we compute the percent moment errors defined in Equations (1.43) and (1.44) for five Monte Carlo trials. These results are shown in Figure 1.9 in comparison to the SROM estimate with $m = 20$ presented above. In contrast to the SROM moment estimates, the Monte Carlo approximations can have very large errors and the magnitude of these errors varies greatly across the different trials. For example, the average moment error $\bar{\epsilon}_M$ for the five Monte Carlo trials are $13.15\%, 18.28\%, 6.26\%, 5.79\%$, and 12.95% compared with 2.78% for the SROM estimate.

1.4.3 Non-convexity of the SROM objective function

In this subsection, we demonstrate an open issue in the construction of SROMs for random vectors in that the objective function in Equation (1.15) has many local minima. A plot of the objective function versus two components of a SROM sample in Figure 1.10(a) shows its complexity. We illustrate the existence of distinct solutions resulting from local minima of the objective function by re-examining the example in Section 4.1.1 for three random starting points in the construction of $\tilde{\mathbf{X}}$. We let $d = 3$ and $m = 10$ and randomly draw the initial guess for the SROM samples according to Equation (1.41) for each of the three trials. All other problem parameters remain fixed at previously specified values. We compare the final objective function values e obtained for each $\tilde{\mathbf{X}}$ as well as the accuracy of the three corresponding eigenvalue SROMs $\tilde{\mathbf{\Lambda}}$.

In Table 1.6, we see that indeed the three optimization trials forming $\tilde{\mathbf{X}}$

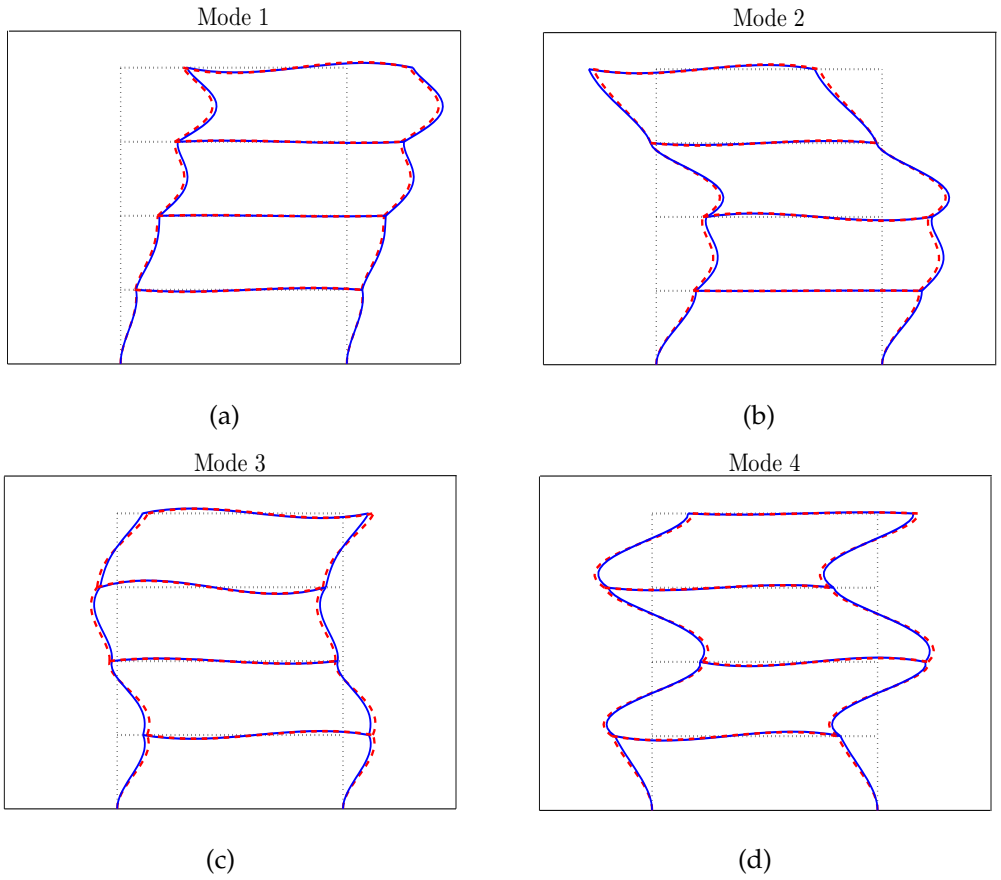

Figure 1.8: Mean estimates for the modes of the planar frame in Example 4.2 computed using SROMs with $m = 10$ (dashed line) and Monte Carlo with 10,000 samples (solid line) for the case when $\rho = 0.9$.

Errors for three distinct SROMs			
Trial	e	$\bar{\epsilon}_M$	$\bar{\epsilon}_{CDF}$
1	8.95e-5	1.48	2.03e-2
2	4.58e-5	2.30	1.59e-2
3	4.40e-4	3.08	2.34e-2

Table 1.6: Objective function values e for SROMs $\tilde{\mathbf{X}}$ formed from three random initial guesses and the moment and CDF errors of the corresponding eigenvalue estimates provided by the SROMs $\tilde{\mathbf{\Lambda}}$ in Example 4.1.1.

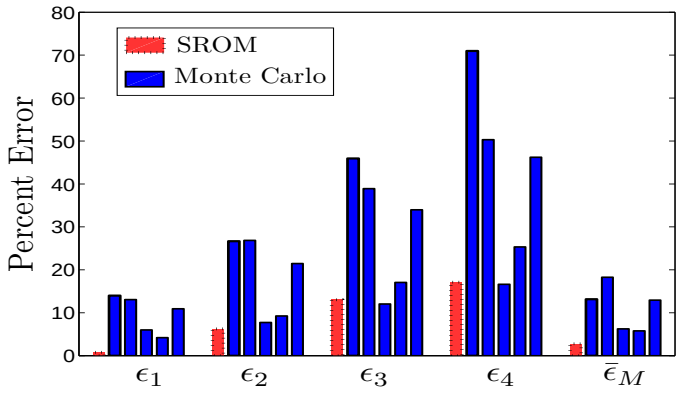

Figure 1.9: Comparison of the accuracy of eigenvalue moment estimates in Example 4.2 using SROMs and five trials of Monte Carlo with the same number of samples ($m = n = 20$). The maximum moment error ($\epsilon_i, i = 1, .., 4$) and average moment error($\bar{\epsilon}_M$) are defined in Equations (1.43) and (1.44), respectively.

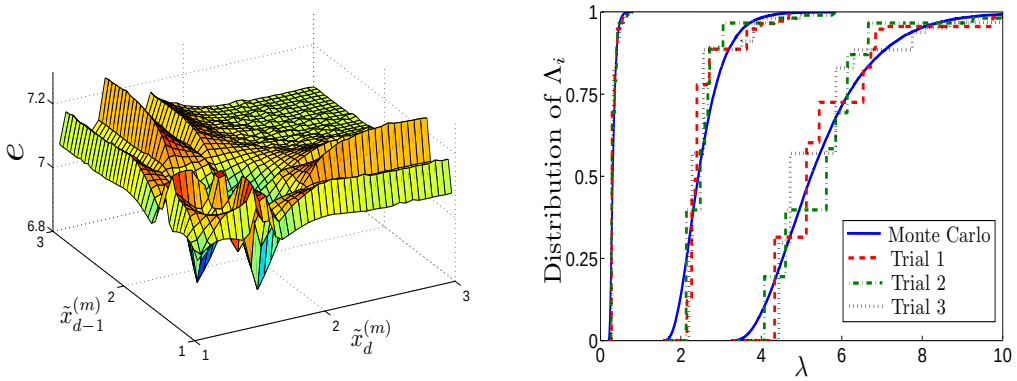

(a) (b)

Figure 1.10: (a) SROM objective function in Equation (1.15) versus two components of a SROM sample. (b) Distribution of eigenvalues from Example 4.1.1 ($d = 3$, $m = 10$) for SROMs $\tilde{\mathbf{\Lambda}}$ corresponding to SROMs $\tilde{\mathbf{X}}$ formed from three optimization trials with different initial guesses.

result in varying final objective function values. The average moment and CDF errors of the corresponding eigenvalue SROMs $\tilde{\mathbf{\Lambda}}$ are seen to vary as well. In the three trials shown, the average eigenvalue moment error increases as the objective function value increases but the same trend does not hold true with the CDF error. The distributions of $\tilde{\Lambda}_i$ and Λ_i for the three trials are compared in Figure 1.10(b), again showing the distinction between each solution formed from different SROMs $\tilde{\mathbf{X}}$.

While this example confirms that SROM construction and resulting SROM-based solutions are sensitive to the initial guess provided, we observe that SROM parameters corresponding to local minima of Equation (1.15) generally provide a satisfactory representation of $\mathbf{X}$. Indeed, the eigenvalue estimates provided by each of the three trials have an average error in moments of 3% or lower and the approximate distributions show excellent agreement with the Monte Carlo solution. Furthermore, we argue that the computational benefits of utilizing gradient-based optimization over global optimization techniques outweigh the potential trade-off in accuracy resulting from a local minimum solution. In practice, one can partially circumvent this issue by performing the optimization for several starting points and then using the most accurate SROM input to efficiently solve a particular forward problem. Depending on the application, this approach will still result in a significant computational speedup over traditional Monte Carlo simulation.

1.5 Conclusions

An improved approach has been proposed to construct stochastic reduced order models $\tilde{\mathbf{X}}$ for general random vectors $\mathbf{X}$. The defining SROM parameters are obtained through the solution of an optimization problem where the objective function quantifies the discrepancy between marginal distributions, marginal moments, and correlation matrices of $\tilde{\mathbf{X}}$ and $\mathbf{X}$ with constraints on admissible values of the probabilities $(p^{(1)}, ..., p^{(m)})$. The existing approach to SROM construction entails solving a series of reduced optimization problems for optimum probability values corresponding to different sets of independently drawn samples of $\mathbf{X}$, which are held fixed in each trial. By optimizing jointly over both $\{\tilde{\mathbf{x}}^{(1)}, ..., \tilde{\mathbf{x}}^{(m)}\}$ and $(p^{(1)}, ..., p^{(m)})$ in one procedure, the optimization algorithm presented here displays significant improvement in computational efficiency and accuracy, as demonstrated through numerical comparisons with the simplified approach used previously.

SROMs formed using the proposed algorithm have been applied to provide efficient solutions to random eigenvalue problems that arise in the modal analysis of structural systems with uncertain properties. SROMs were also shown to provide accurate estimates of the dynamics of such uncertain systems in time. Analytical bounds were established on the discrepancy between exact and SROM-based solutions to random eigenvalue problems. Numerical examples show that SROM-based estimates for the statistics of natural frequencies and modes of dynamic systems with random stiffness are accurate and stable for small SROM sizes $m \lesssim 20$. On the other hand, Monte Carlo estimates with the same number of samples are unstable and can be highly inaccurate.

1.6 Acknowledgments

Wilkins Aquino and James Warner acknowledge the kind support of the National Science Foundation through Award #CAREER-0643618. Mircea Grigoriu gratefully acknowledges the support of the National Science Foundation under Grants CMMI-0969150 and CMMI-0925714.

REFERENCES

[1] I. Babuska, F. Nobile, and R. Tempone. A stochastic collocation method for elliptic partial differential equations with random input data. *SIAM Journal of Numerical Analysis*, 45(3):1005–1034, 2007.

[2] I. Babuska, R. Tempone, and G. E. Zouraris. Galerkin finite element approximations of stochastic elliptic partial differential equations. *SIAM Journal of Numerical Analysis*, 42:800–825, 2004.

[3] A. K. Chopra. *Dynamics of Structures: Theory and Applications to Earthquake Engineering*. Prentice-Hall, Upper Saddle River, NJ, Second edition, 2001.

[4] J. W. Demmel. *Applied Numerical Linear Algebra*. SIAM, Philadelphia, PA, 1997.

[5] D. Gottlieb and D. Xiu. Galerkin method for wave equations with uncertain coefficients. *Communications in Computational Physics*, 3(2):505–518, 2008.

[6] M. Grigoriu. *Stochastic Calculus. Applications in Science and Engineering*. Birkhäuser, Boston, 2002.

[7] M. Grigoriu. Reduced order models for random functions. application to stochastic problems. *Applied Mathematical Modelling*, 33:161–175, 2009.

[8] M. Grigoriu. Effective conductivity by stochastic reduced order models (sroms). *Computational Materials Science*, 50:138–146, 2010.

[9] M. Grigoriu. Linear random vibration by stochastic reduced-order models. *International Journal for Numerical Methods in Engineering*, 82:1537–1559, 2010.

[10] 0. Le Maitre, O. Knio, H. Najm, and R. Ghanem. A stochastic projection method for fluid flow: Basic formulation. *Journal of Computational Physics*, 173:481–511, 2001.

[11] G. Lin, X. Wan, C.-H. Su, and G. E. Karniadakis. Stochastic computational fluid mechanics. *IEEE Computing in Science and Engineering*, 9(2):21–29, 2007.

[12] Y. Marzouk and D. Xiu. A stochastic collocation approach to bayesian inference in inverse problems. *Communications in Computational Physics*, 6(4):826–847, 2009.

[13] MATLAB version 7.10.0 (R2010a). The MathWorks Inc., Natick, Massachusetts, 2010.

[14] J. H. Wilkinson. Elementary proof of the wielandt-hoffman theorem and of its generalization. Technical report, Stanford University, Stanford, California, 1970.

[15] D. Xiu. *Numerical Methods for Stochastic Computations. A Spectral Method Approach*. Princeton University Press, Princeton, NJ, 2010.

[16] D. Xiu and G. E. Karniadakis. The weiner-askey polynomial chaos for stochastic differential equations. *SIAM Journal of Scientific Computing*, 24(2):619–644, 2002.

CHAPTER 2

INVERSE MATERIAL IDENTIFICATION IN COUPLED ACOUSTIC-STRUCTURE INTERACTION USING A MODIFIED ERROR IN CONSTITUTIVE EQUATION FUNCTIONAL

Co-authors: Manuel I. Diaz, Wilkins Aquino, and Marc Bonnet

Paper under review in *Computational Mechanics*, submitted November 2013.

Abstract

This work focuses on the identification of heterogeneous linear elastic moduli in the context of frequency-domain, coupled acoustic-structure interaction (ASI), using either solid displacement or fluid pressure measurement data. The approach postulates the inverse problem as an optimization problem where the solution is obtained by minimizing a modified error in constitutive equation (MECE) functional. The latter measures the discrepancy in the constitutive equations that connect kinematically admissible strains and dynamically admissible stresses, while incorporating the measurement data as additional quadratic error terms.

We demonstrate two strategies for selecting the MECE weighting coefficient to produce regularized solutions to the ill-posed identification problem: 1) the discrepancy principle of Morozov, and 2) an error-balance approach that selects the weight parameter as the minimizer of another functional involving the ECE and the data misfit. Numerical results demonstrate that the proposed methodology can successfully recover elastic parameters in 2D and 3D ASI systems

from response measurements taken in either the solid or fluid subdomains. Furthermore, both regularization strategies are shown to produce accurate reconstructions when the measurement data is polluted with noise. The discrepancy principle is shown to produce nearly optimal solutions, while the error-balance approach, although not optimal, remains effective and does not need a priori information on the noise level.

2.1 Introduction

The noninvasive characterization of material properties in a physical system is of great importance in a variety of science and engineering fields. Along these lines, considerable research efforts have been made to formulate and solve inverse problems in which experimental measurements of the mechanical response of a system are used to infer its defining material parameters. Such parameter estimation problems are prevalent in areas like damage detection in structures, geotechnical exploration, biomechanical imaging, etc. [26, 24, 32, 4]. In this work, we narrow our focus on the problem of elasticity imaging in systems that involve coupled acoustic-structure interaction (ASI).

While an inverse problem of this nature could arise in many scenarios, from oceanic oil discovery to the nondestructive evaluation of marine structures, we are motivated mainly by applications in medical imaging. Here, the modeling of interaction between an acoustic fluid and biomechanical structure is necessary for imaging areas like the heart wall, arteries, and bladder that have direct contact with blood and other bodily fluid. Since elastic properties are known to be an indicator for distinguishing diseased from healthy human tis-

sue [17, 8, 27, 21], elasticity imaging has become an essential tool in detecting the onset and monitoring of the progression of a number of diseases. Depending on the imaging modality used, either the response of the tissue itself [29, 25] or the acoustic emission in the surrounding fluid [14, 15] under a prescribed excitation can be used as data for the inverse identification of the tissue's elastic parameters.

Despite its importance in medical imaging and other applications, there exist relatively few computational approaches for parameter estimation in systems with ASI. In [10], an approach was developed to inversely estimate the viscoelastic properties of a submerged solid using pressure data from the steady-state dynamic response of the system. Since solving the inverse problem requires many costly evaluations of a forward ASI finite element solver, this work was extended in [9] to use reduced-order modeling with proper orthogonal decomposition for the forward problem to reduce computation time. The estimation of material parameters in submerged, orthotropic elastic cylinders was performed in [28], where it was shown that a surface velocity measurement was sufficient to recover the orthotropic parameters, while an acoustic pressure measurement contained only enough information to recover two of the three unknown parameters. While the previously mentioned works operated under the assumption of homogeneous materials with geometries that were known *a priori*, the work in [1] sought pointwise reconstructions by representing the spatial variation of the unknown elastic modulus using Gaussian radial basis functions. Inclusions were properly identified within a submerged solid using both fluid pressure measurements and surface velocity measurements on the solid.

A common theme in the above studies was the minimization of a norm (generally L^2) of the error between computed and measured system responses using non-gradient based optimization techniques to obtain parameter estimates. In this work, as the main point of departure, we postulate the inverse problem as the minimization of a modified error in constitutive equation (MECE) functional, which is then solved with a gradient-based approach. The MECE functional is a combination of the error in constitutive equation (ECE), introduced in [22] as a measure of the discrepancy in the constitutive equations that connect kinematically admissible strains and dynamically admissible stresses, and quadratic error terms that incorporate the measurement data. MECE-based approaches for identification initially appeared in the context of model updating from vibrational data [23, 5]. The underlying principle was to split the equations into a reliable set (containing, for example, the equilibrium equations, initial conditions, and boundary conditions), to be enforced strictly as constraints, and an unreliable set (that included measured data and the unknown constitutive properties), contributing terms in the MECE functional to be minimized. More recent extensions of the MECE approach to time-domain formulations [2, 16] were shown to be very robust in the presence of high levels of noise, while also providing an inherent error estimate through the ECE. The MECE method was extended to large scale identification problems in [3], where the authors also showed that this approach displayed fast convergence and accuracy as compared to conventional least-squares minimization approaches.

In this work, we extend the MECE approach for the inverse estimation of elastic material parameters to the context of frequency-domain, coupled ASI systems. The MECE functional is modified to include an additional error term for fluid pressure data, allowing for a general formulation where measurements

of either the displacement response in the solid or the acoustic emission in the surrounding fluid can be used as data for the inverse problem. In doing so, the governing equations of the solid system, the acoustic fluid system, and the coupling conditions between them are enforced as constraints, while the MECE functional is minimized to obtain an estimate for the unknown material parameters. The weight parameter that multiplies the misfit data term in the MECE functional in essence behaves as a regularization parameter. Two different strategies for selecting this weight parameter are demonstrated and compared in numerical examples: 1) the discrepancy principle of Morozov [20, 12], and 2) an error-balance approach where the sum of the squares of the ECE and data mismatch terms that enter the definition of the MECE functional is minimized.

The article is organized as follows. The following section formulates both the forward and inverse problems for a coupled ASI system and then details the MECE approach for solving the inverse problem. Section 2.3 then comments on some of the practical aspects of the MECE algorithm, including the two regularization methods that are demonstrated in this work. The performance of the numerical method is then demonstrated in Section 2.4 through results for the recovery of elastic parameters given noisy measurements taken in either the solid or the fluid, on 2D and 3D examples. Concluding remarks are given in Section 2.5.

2.2 Formulation

2.2.1 Forward problem

In this section, we present the governing equations for the steady-state acoustic-structure interaction problem. We consider a linear elastic body Ω_s immersed in a semi-infinite fluid domain Ω_f with a separating fluid-structure interface denoted as Γ_fs. In this work, we assume both small strains and deformations in the solid domain as well as negligible flow and small pressure amplitudes in the fluid domain. Furthermore, body forces throughout each subdomain are taken to be negligible. We consider a constant mass density within the solid domain and a constant mass density and bulk modulus in the fluid domain. The remaining quantities can have spatial and/or frequency dependence, which is suppressed in our notation for simplicity.

The linear elastic solid domain Ω_s undergoing time-harmonic motion is governed by (a) the balance equations

$$\nabla\cdot\boldsymbol{\sigma} = -\rho_\mathrm{s}\omega^2\boldsymbol{u} \qquad \text{in } \Omega_\mathrm{s}, \tag{2.1a}$$

$$\boldsymbol{\sigma}\cdot\boldsymbol{n}_\mathrm{s} = \boldsymbol{t} \qquad \text{on } \Gamma_t, \tag{2.1b}$$

$$\boldsymbol{\sigma}\cdot\boldsymbol{n}_\mathrm{s} = -p\boldsymbol{n}_\mathrm{s} + \boldsymbol{g} \qquad \text{on } \Gamma_\mathrm{fs}, \tag{2.1c}$$

where $\boldsymbol{\sigma}$ is the stress tensor, ρ_s is the solid mass density, ω is the angular frequency, $\boldsymbol{u}$ is the displacement field, $\boldsymbol{n}_\mathrm{s}$ is the unit normal vector pointing outward from Ω_s, $\boldsymbol{t}$ and $\Gamma_t \subset \partial\Omega_\mathrm{s}$ are the specified traction and its support, p is the

acoustic pressure; (b) the kinematic compatibility equations

$$\boldsymbol{\varepsilon}[\boldsymbol{u}] = \tfrac{1}{2}\left(\nabla \boldsymbol{u} + \nabla \boldsymbol{u}^T\right) \qquad \text{in } \Omega_{\mathrm{s}}, \tag{2.2a}$$

$$\boldsymbol{u} = \boldsymbol{0} \qquad \text{on } \Gamma_u, \tag{2.2b}$$

where $\boldsymbol{\varepsilon}$ is the linearized strain tensor and $\Gamma_u = \partial\Omega_{\mathrm{s}} \setminus \Gamma_t$ is the constrained part of the boundary; (c) the constitutive (linear elastic) equation

$$\boldsymbol{\sigma} = \mathbb{C} : \boldsymbol{\varepsilon} \qquad \text{in } \Omega_{\mathrm{s}}, \tag{2.3}$$

where $\mathbb{C}$ is the heterogeneous fourth-order elasticity tensor. The boundary condition in Equation (2.1c) prescribes balance between forces arising from the solid and fluid domains along the wet interface Γ_{fs}, with $\boldsymbol{g}$ denoting a specified traction that may be present over Γ_{fs}.

The governing equations for the acoustic fluid system can be written in the frequency domain as

$$\nabla^2 p + k^2 p = 0 \qquad \text{in } \Omega_{\mathrm{f}}, \tag{2.4a}$$

$$p = 0 \qquad \text{on } \Gamma_p, \tag{2.4b}$$

$$\partial_{\boldsymbol{n}_{\mathrm{f}}} p = -f\,(ik + \beta)\,p \qquad \text{on } \Psi_R, \tag{2.4c}$$

$$\partial_{\boldsymbol{n}_{\mathrm{f}}} p = \rho_{\mathrm{f}} \omega^2 \boldsymbol{u} \cdot \boldsymbol{n}_{\mathrm{f}} \qquad \text{on } \Gamma_{\mathrm{fs}} \tag{2.4d}$$

where $k = \omega\sqrt{\rho_{\mathrm{f}}/K}$ is the wave number with ρ_{f} and K denoting the fluid mass density and bulk modulus, respectively. The vector $\boldsymbol{n}_{\mathrm{f}}$ is the unit normal pointing outward from Ω_{f}. Here, we introduce the artificial boundary Ψ_R in order to truncate the semi-infinite fluid domain for computational purposes. Equation (2.4c) is the non-reflecting radiation condition applied to this boundary as a first order approximation to the Sommerfield radiation condition, where f and β are geometry-specific constants. While this simple treatment suffices in this work,

we note that more sophisticated techniques like higher order absorbing conditions or perfectly matched layers [7] could be substituted here. Equation (2.4d) arises from the continuity in displacements of fluid and solid particles normal to Γ_{fs}. This interface condition along with Equation (2.1c) provide the coupling between the two sets of governing equations for the solid and fluid systems.

Since the constitutive tensor $\mathbb{C}$ is the main unknown of the inverse problem, the constitutive equation (2.3) will (in remaining consistent with earlier works based on MECE formulations) be included in the MECE functional to be minimized, while equations (2.1), (2.2) and (2.4) will be enforced exactly, in weak form. For the latter purpose, let the spaces of trial and test solutions for displacements and acoustic pressures, respectively, be defined as

$$\mathcal{U} = \left\{ \boldsymbol{u} |\ \boldsymbol{u} \in [H^1(\Omega_{\text{s}})]^d, \quad \boldsymbol{u} = \boldsymbol{0} \quad \text{on } \Gamma_u \right\} \tag{2.5a}$$

$$\mathcal{P} = \left\{ p |\ p \in H^1(\Omega_{\text{f}}), \quad p = 0 \quad \text{on } \Gamma_p \right\} \tag{2.5b}$$

where d is the spatial dimension. Furthermore, the space of dynamically-admissible stresses in the solid is defined by

$$\mathcal{S}(\boldsymbol{u}) := \left\{ \boldsymbol{\sigma} |\ \boldsymbol{\sigma} \in H_{\text{div}}(\Omega_{\text{s}}),\ \nabla \cdot \boldsymbol{\sigma} = -\rho_{\text{s}} \omega^2 \boldsymbol{u} \ \text{ in } \Omega_{\text{s}},\ \ \boldsymbol{\sigma} \cdot \boldsymbol{n}_{\text{s}} = \boldsymbol{t} \ \text{ on } \Gamma_t \right\} \tag{2.6}$$

With these definitions, the weak formulation for equations (2.1) and (2.2a) is

$$\mathcal{B}(\boldsymbol{\sigma}, \boldsymbol{u}, \boldsymbol{w}) = \mathcal{F}_{\text{s}}(p, \boldsymbol{w}) + \mathcal{F}(\boldsymbol{w}) \quad \forall \boldsymbol{w} \in \mathcal{U} \tag{2.7}$$

having set

$$\mathcal{B}(\boldsymbol{\sigma}, \boldsymbol{u}, \boldsymbol{w}) := (\boldsymbol{\sigma}, \boldsymbol{\varepsilon}[\boldsymbol{w}])_{\Omega_{\text{s}}} - \rho_{\text{s}} \omega^2 (\boldsymbol{u}, \boldsymbol{w})_{\Omega_{\text{s}}}, \tag{2.8a}$$

$$\mathcal{F}_{\text{s}}(p, \boldsymbol{w}) := (p \boldsymbol{n}_{\text{s}}, \boldsymbol{w})_{\Gamma_{\text{fs}}}, \tag{2.8b}$$

$$\mathcal{F}(\boldsymbol{w}) := (\boldsymbol{t}, \boldsymbol{w})_{\Gamma_t} + (\boldsymbol{g}, \boldsymbol{w})_{\Gamma_{\text{fs}}} \tag{2.8c}$$

and where $(\cdot,\cdot)_\Phi$ denotes the $L^2(\Phi)$ inner product. Specifically, for two second-order tensor fields $\boldsymbol{x},\ \boldsymbol{y}$, one has

$$(\boldsymbol{x},\boldsymbol{y})_\Phi = \int_\Phi \boldsymbol{x} : \bar{\boldsymbol{y}}\, d\Phi = \int_\Phi x_{ij}\bar{y}_{ij}\, d\Phi \tag{2.9}$$

where the over-bar $\bar{\boldsymbol{y}}$ denotes complex conjugation and the repeated indices indicate summation over the components of $\boldsymbol{x}$ and $\boldsymbol{y}$.

For the set of equations (2.4) governing the fluid system, the corresponding weak formulation is given as

$$\mathcal{A}_\mathrm{f}(p,v) = \mathcal{F}_\mathrm{f}(\boldsymbol{u},v) \quad \forall v \in \mathcal{P} \tag{2.10}$$

where

$$\mathcal{A}_\mathrm{f}(p,v) := (\nabla p,\nabla v)_{\Omega_\mathrm{f}} - k^2\,(p,v)_{\Omega_\mathrm{f}} + f(ik+\beta)\,(p,v)_{\Psi_R} \tag{2.11a}$$

$$\mathcal{F}_\mathrm{f}(\boldsymbol{u},v) := \rho_\mathrm{f}\omega^2(\boldsymbol{u}\cdot\boldsymbol{n}_\mathrm{f},v)_{\Gamma_\mathrm{fs}} \tag{2.11b}$$

2.2.2 Inverse Problem

The inverse problem associated with the coupled ASI forward problem consists of estimating the spatial distribution of elastic moduli in Ω_s that define the constitutive tensor $\mathbb{C}$, given measured acoustic pressures $p^m(\hat{\boldsymbol{x}}_\mathrm{f}), \hat{\boldsymbol{x}}_\mathrm{f} \in \Omega_\mathrm{f}^m \subseteq \overline{\Omega}_\mathrm{f}$ and/or measured solid displacements $\boldsymbol{u}^m(\hat{\boldsymbol{x}}_\mathrm{s}),\ \hat{\boldsymbol{x}}_\mathrm{s} \in \Omega_\mathrm{s}^m \subseteq \overline{\Omega}_\mathrm{s}$, obtained at one or more frequencies. Additionally, we assume that the properties of the fluid are known.

Modified error in constitutive equation approach

In this work, the inverse problem is cast as an optimization problem in which the unknown constitutive tensor is estimated by minimizing a MECE func-

tional. The MECE functional combines two types of error terms: 1) an error in constitutive equation (ECE) functional [22] that measures the discrepancy in the constitutive equations that connect kinematically admissible strains and dynamically admissible stresses, and 2) quadratic error terms quantifying the mismatch between measurement data and computed fields for given material parameter values. The MECE functional in the present ASI context is expressed as

$$\Lambda(\boldsymbol{u},\boldsymbol{\sigma},p;\mathbb{C}) = U(\boldsymbol{u},\boldsymbol{\sigma};\mathbb{C}) + \frac{\kappa_{\mathrm{s}}}{2}\left\|\boldsymbol{u}-\boldsymbol{u}^{m}\right\|^{2}_{L^{2}(\Omega_{\mathrm{s}}^{m})} + \frac{\kappa_{\mathrm{f}}}{2}\left\|p-p^{m}\right\|^{2}_{L^{2}(\Omega_{\mathrm{f}}^{m})} \tag{2.12}$$

where

$$U(\boldsymbol{u},\boldsymbol{\sigma};\mathbb{C}) := \frac{1}{2}\int_{\Omega_{\mathrm{s}}} (\boldsymbol{\sigma}-\mathbb{C}:\boldsymbol{\varepsilon}[\boldsymbol{u}]):\mathbb{C}^{-1}:(\overline{\boldsymbol{\sigma}-\mathbb{C}:\boldsymbol{\varepsilon}[\boldsymbol{u}]})\,d\Omega_{\mathrm{s}} \tag{2.13}$$

is the ECE functional for linear elastic materials and κ_{s} and κ_{f} are weighting parameters for the solid displacement and acoustic pressure data, respectively, that control the relative importance of these terms in the inverse problem. The ECE term (2.13) quantifies the discrepancy between kinematically admissible displacements and dynamically admissible stresses for a given $\mathbb{C}$ that bears the important properties

$$U(\boldsymbol{u},\boldsymbol{\sigma};\mathbb{C}) \geq 0 \quad \forall\mathbb{C} \tag{2.14}$$

$$U(\boldsymbol{u},\boldsymbol{\sigma};\mathbb{C}) = 0 \iff \boldsymbol{\sigma} = \mathbb{C}:\boldsymbol{\varepsilon}[\boldsymbol{u}] \tag{2.15}$$

Now, the solution of an inverse problem cast using a MECE framework for an ASI system is given by

$$(\boldsymbol{u}^{\star},\boldsymbol{\sigma}^{\star},p^{\star},\mathbb{C}^{\star}) = \underset{\boldsymbol{u}\in\mathcal{U},\,\boldsymbol{\sigma}\in\mathcal{S}(\boldsymbol{u}),\,p\in\mathcal{P},\,\mathbb{C}\in\mathcal{C}}{\arg\min}\ \Lambda(\boldsymbol{u},\boldsymbol{\sigma},p;\mathbb{C}), \tag{2.16}$$

where $\mathcal{C}$ is the search space for the unknown constitutive tensor comprised of all fourth-order tensor fields that are symmetric, positive definite, and bounded,

while the remaining spaces $\mathcal{U}, \mathcal{S}, \mathcal{P}$ are defined by (2.5a), (2.5b) and (2.6). On noting that (2.16) defines a PDE-constrained optimization problem, we define a Lagrangian functional $\mathcal{L} : \mathcal{U} \times \mathcal{S} \times \mathcal{P} \times \mathcal{U} \times \mathcal{P} \times \mathcal{C} \to \mathbb{R}$ as

$$\mathcal{L}(\boldsymbol{u}, \boldsymbol{\sigma}, p, \boldsymbol{w}, v; \mathbb{C}) := \Lambda(\boldsymbol{u}, \boldsymbol{\sigma}, p; \mathbb{C}) - \mathrm{Re}\left[\mathcal{B}(\boldsymbol{\sigma}, \boldsymbol{u}, \boldsymbol{w}) - \mathcal{F}_{\mathrm{s}}(p, \boldsymbol{w}) - \mathcal{F}(\boldsymbol{w})\right] - \mathrm{Re}\left[\mathcal{A}_{\mathrm{f}}(p, v) - \mathcal{F}_{\mathrm{f}}(\boldsymbol{u}, v)\right] \tag{2.17}$$

where $\mathcal{B}$, $\mathcal{A}_{\mathrm{f}}$, $\mathcal{F}_{\mathrm{s}}$, $\mathcal{F}_{\mathrm{f}}$ and $\mathcal{F}$ were defined in Section 2.2.1 and $\mathrm{Re}[\cdot]$ denotes the real part of a complex number. Note that the test functions $\boldsymbol{w} \in \mathcal{U}$ and $v \in \mathcal{P}$ used in the variational forms of the elastic and acoustic systems, respectively, act as Lagrange multipliers in (3.26) [18]. The remainder of this section is devoted to the derivation (and solution strategy) of the first-order optimality conditions for the minimization problem (2.16).

Derivation of the first-order optimality conditions

We now derive the first-order optimality conditions for the MECE inverse problem (2.16) by taking directional derivatives of the Lagrangian (3.26) with respect to $\boldsymbol{u}, \boldsymbol{\sigma}, p, \boldsymbol{w}, v, \mathbb{C}$ and setting each to zero. The unknown fields $\boldsymbol{u}, \boldsymbol{\sigma}, p, \mathbb{C}$ that satisfy these conditions will be those that minimize the MECE functional (2.12) while also satisfying the forward ASI problem. We denote, for example, the directional derivative of the Lagrangian functional $\mathcal{L}$ with respect to the stress field $\boldsymbol{\sigma}$ as $\mathcal{L}'_{\boldsymbol{\sigma}}$, which is given as

$$\langle \mathcal{L}'_{\boldsymbol{\sigma}}, \hat{\boldsymbol{\sigma}} \rangle = \frac{d}{d\theta}[\mathcal{L}(\boldsymbol{u}, \boldsymbol{\sigma} + \theta\hat{\boldsymbol{\sigma}}, p, \boldsymbol{w}, v; \mathbb{C})]\Big|_{\theta=0} \tag{2.18}$$

for all variations $\hat{\boldsymbol{\sigma}} \in H_{\mathrm{div}}(\Omega_{\mathrm{s}})$. By carrying out the calculation in (2.18) and setting the result equal to zero, we obtain the following expression for the stress

field

$$\langle \mathcal{L}'_{\boldsymbol{\sigma}}, \hat{\boldsymbol{\sigma}} \rangle = \mathrm{Re}\left((\hat{\boldsymbol{\sigma}}, \mathbb{C}^{-1} : \boldsymbol{\sigma})_{\Omega_\mathrm{s}} - (\hat{\boldsymbol{\sigma}}, \boldsymbol{\varepsilon}[\boldsymbol{u}])_{\Omega_\mathrm{s}} - (\hat{\boldsymbol{\sigma}}, \boldsymbol{\varepsilon}[\boldsymbol{w}])_{\Omega_\mathrm{s}} \right)$$

$$= \mathrm{Re}\left((\hat{\boldsymbol{\sigma}}, \mathbb{C}^{-1} : \boldsymbol{\sigma} - \boldsymbol{\varepsilon}[\boldsymbol{u}] - \boldsymbol{\varepsilon}[\boldsymbol{w}])_{\Omega_\mathrm{s}} \right) \qquad \forall \hat{\boldsymbol{\sigma}} \in \mathcal{S} \qquad (2.19)$$

$$\boldsymbol{\sigma} = \mathbb{C} : \boldsymbol{\varepsilon}[\boldsymbol{u} + \boldsymbol{w}] \qquad (2.20)$$

Proceeding in the same fashion, the partial derivatives of the Lagrangian functional with respect to the remaining mechanical fields, the Lagrange multipliers, and the constitutive tensor are given by

$$\langle \mathcal{L}'_{\boldsymbol{w}}, \hat{\boldsymbol{w}} \rangle = \mathrm{Re}\left((\boldsymbol{\sigma}, \boldsymbol{\varepsilon}[\hat{\boldsymbol{w}}])_{\Omega_\mathrm{s}} - \omega^2 (\rho_\mathrm{s} \boldsymbol{u}, \hat{\boldsymbol{w}})_{\Omega_\mathrm{s}} - (\boldsymbol{t}, \hat{\boldsymbol{w}})_{\Gamma_t} - (\boldsymbol{g}, \hat{\boldsymbol{w}})_{\Gamma_\mathrm{fs}} - (p \boldsymbol{n}_\mathrm{s}, \hat{\boldsymbol{w}})_{\Gamma_\mathrm{fs}} \right) \qquad (\hat{\boldsymbol{w}} \in \mathcal{U})$$

$$\langle \mathcal{L}'_{v}, \hat{v} \rangle = \mathrm{Re}\left(- (\nabla p, \nabla \hat{v})_{\Omega_\mathrm{f}} + k^2 (p, \hat{v})_{\Omega_\mathrm{f}} - f(ik + \beta)(p, \hat{v})_{\Psi_R} + \rho_\mathrm{f} \omega^2 (\boldsymbol{u} \cdot \boldsymbol{n}_\mathrm{f}, \hat{v})_{\Gamma_\mathrm{fs}} \right) \quad (\hat{v} \in \mathcal{P})$$

$$\langle \mathcal{L}'_{\boldsymbol{u}}, \hat{\boldsymbol{u}} \rangle = \mathrm{Re}\Big((\mathbb{C} : \boldsymbol{\varepsilon}[\boldsymbol{u}] - \boldsymbol{\sigma}, \boldsymbol{\varepsilon}[\hat{\boldsymbol{u}}])_{\Omega_\mathrm{s}} + \kappa_\mathrm{s} (\boldsymbol{u} - \boldsymbol{u}^m, \hat{\boldsymbol{u}})_{\Omega_m} +$$

$$+ \rho_\mathrm{s} \omega^2 (\boldsymbol{w}, \hat{\boldsymbol{u}})_{\Omega_\mathrm{s}} + \rho_\mathrm{f} \omega^2 (\hat{\boldsymbol{u}} \cdot \boldsymbol{n}_\mathrm{f}, v)_{\Gamma_\mathrm{fs}} \Big) \qquad (\hat{\boldsymbol{u}} \in \mathcal{U})$$

$$\langle \mathcal{L}'_{p}, \hat{p} \rangle = \mathrm{Re}\Big(- (\nabla \hat{p}, \nabla v)_{\Omega_\mathrm{f}} + k^2 (\hat{p}, v)_{\Omega_\mathrm{f}} - f(ik + \beta)(\hat{p}, v)_{\Psi_R} +$$

$$- (\hat{p} \boldsymbol{n}_\mathrm{s}, \boldsymbol{w})_{\Gamma_\mathrm{fs}} + \kappa_\mathrm{f} (p - p^m, \hat{p})_{\Omega_\mathrm{f}^m} \Big) \qquad (\hat{p} \in \mathcal{P})$$

$$\langle \mathcal{L}'_{\mathbb{C}}, \hat{\mathbb{C}} \rangle = \left(\hat{\mathbb{C}} \,,\, \boldsymbol{\varepsilon}[\boldsymbol{u}] \otimes \boldsymbol{\varepsilon}[\bar{\boldsymbol{u}}] - (\mathbb{C}^{-1} : \boldsymbol{\sigma}) \otimes (\mathbb{C}^{-1} : \bar{\boldsymbol{\sigma}}) \right)_{\Omega_\mathrm{s}} \qquad (\hat{\mathbb{C}} \in \mathcal{C})$$

By setting these partial derivatives equal to zero and substituting the definition for $\boldsymbol{\sigma}$ in Equation (2.20), we obtain the following set of coupled variational equations

$$\mathcal{A}_\mathrm{s}(\boldsymbol{u}, \hat{\boldsymbol{w}}) + (\mathbb{C} : \boldsymbol{\varepsilon}[\boldsymbol{w}], \boldsymbol{\varepsilon}[\hat{\boldsymbol{w}}])_{\Omega_\mathrm{s}} - \mathcal{F}_\mathrm{s}(p, \hat{\boldsymbol{w}}) - \mathcal{F}(\hat{\boldsymbol{w}}) = 0 \qquad \forall \hat{\boldsymbol{w}} \in \mathcal{U} \qquad (2.21a)$$

$$\mathcal{A}_\mathrm{f}(p, \hat{v}) - \mathcal{F}_\mathrm{f}(\boldsymbol{u}, \hat{v}) = 0 \qquad \forall \hat{v} \in \mathcal{P} \qquad (2.21b)$$

$$\mathcal{A}_\mathrm{s}(\boldsymbol{w}, \hat{\boldsymbol{u}}) - \rho_\mathrm{f} \omega^2 (v, \hat{\boldsymbol{u}} \cdot \boldsymbol{n}_\mathrm{f})_{\Gamma_\mathrm{fs}} + \kappa_\mathrm{s} (\boldsymbol{u} - \boldsymbol{u}^m, \hat{\boldsymbol{u}})_{\Omega_\mathrm{s}^m} = 0 \qquad \forall \hat{\boldsymbol{u}} \in \mathcal{U} \qquad (2.21c)$$

$$(\boldsymbol{w}, \hat{p} \boldsymbol{n}_\mathrm{s})_{\Gamma_\mathrm{fs}} + \mathcal{A}_\mathrm{f}(v, \hat{p}) + \kappa_\mathrm{f} (p^m - p, \hat{p})_{\Omega_\mathrm{f}^m} = 0 \qquad \forall \hat{p} \in \mathcal{P} \qquad (2.21d)$$

$$\left(\hat{\mathbb{C}} \,,\, \boldsymbol{\varepsilon}[\boldsymbol{u}] \otimes \boldsymbol{\varepsilon}[\bar{\boldsymbol{u}}] - \boldsymbol{\varepsilon}[\boldsymbol{u} + \boldsymbol{w}] \otimes \boldsymbol{\varepsilon}[\bar{\boldsymbol{u}} + \bar{\boldsymbol{w}}] \right)_{\Omega_\mathrm{s}} = 0 \qquad \forall \hat{\mathbb{C}} \in \mathcal{C} \qquad (2.21e)$$

where expressions have been simplified by introducing the bilinear forms $\mathcal{A}_{\mathrm{f}}$, given by (2.11a), and $\mathcal{A}_{\mathrm{s}}$, defined by

$$\mathcal{A}_{\mathrm{s}}(\boldsymbol{u},\boldsymbol{w}) := \mathcal{B}_{\mathrm{s}}(\mathbb{C}:\boldsymbol{\varepsilon}\left[\boldsymbol{u}\right],\boldsymbol{u},\boldsymbol{w}) = \left(\mathbb{C}:\boldsymbol{\varepsilon}\left[\boldsymbol{u}\right],\boldsymbol{\varepsilon}\left[\boldsymbol{w}\right]\right)_{\Omega_{\mathrm{s}}} - \rho_{\mathrm{s}}\omega^2(\boldsymbol{u},\boldsymbol{w})_{\Omega_{\mathrm{s}}}. \tag{2.22}$$

The set of variational equations (2.21), along with (2.20), represent the first-order optimality conditions for the MECE minimization problem (2.16).

Solution of the first-order optimality conditions

The system of equations (2.21) can be subdivided into (a) a set of four linear equations (2.21a)-(2.21d), and (b) the non-linear equation (2.21e). Like in earlier applications of MECE to parameter identification, e.g. [5, 3], this subdivision makes it natural to adopt an iterative alternating strategy of block Gauss-Seidel type whereby each solution iteration for (2.21) consists in (i) solving the set of linear equations (2.21a)-(2.21d) for the mechanical fields and Lagrange multipliers, with $\mathbb{C}$ kept fixed, and (ii) updating $\mathbb{C}$ via equation (2.21e). Here, this method will be seen to entail solving a 4×4 complex symmetric block linear system followed (when considering isotropic materials) by simple and explicit update formulas for the elastic moduli, similar to those used in [3].

Step (i): field and multiplier update The finite element method [6] is used to discretize and transform the coupled weak formulation (2.21a)-(2.21d) into a linear system of equations. Using standard Voigt notation, the displacement fields, pressure field, and corresponding test functions are replaced with the

following discrete approximations

$$
\begin{aligned}
\boldsymbol{u}^h &= [N_{\mathrm{s}}]\{u\}, & \hat{\boldsymbol{u}}^h &= [N_{\mathrm{s}}]\{\hat{u}\}, & \boldsymbol{\varepsilon}[\boldsymbol{u}^h] &= [B_{\mathrm{s}}]\{u\}, \\
\boldsymbol{w}^h &= [N_{\mathrm{s}}]\{w\}, & \hat{\boldsymbol{w}}^h &= [N_{\mathrm{s}}]\{\hat{w}\}, & \boldsymbol{\varepsilon}[\boldsymbol{w}^h] &= [B_{\mathrm{s}}]\{w\}, \\
p^h &= [N_{\mathrm{f}}]\{p\}, & \hat{p}^h &= [N_{\mathrm{f}}]\{\hat{p}\}, & \nabla p^h &= [B_{\mathrm{f}}]\{p\}, \\
v^h &= [N_{\mathrm{f}}]\{v\}, & \hat{v}^h &= [N_{\mathrm{f}}]\{\hat{v}\}, & \nabla v^h &= [B_{\mathrm{f}}]\{v\},
\end{aligned}
$$

where $[N_{s(f)}]$ and $[B_{s(f)}]$ represent matrices of finite element shape functions and their derivatives with respect to spatial coordinates, respectively, for the solid (fluid) system. The terms, $\{\cdot\}$, represent vectors of nodal quantities in the finite element mesh. Inserting these approximations into the variational problem (2.21a)-(2.21d) and simplifying, we arrive at the following 4×4 block system of equations:

$$
\begin{bmatrix}
[H_{\mathrm{s}}] & -[S]^T & [K_{\mathrm{s}}] & [0] \\
-\rho_{\mathrm{f}}\omega^2[S] & [H_{\mathrm{f}}] & [0] & [0] \\
-\kappa_{\mathrm{s}}[Q_{\mathrm{s}}] & [0] & [H_{\mathrm{s}}] & -\rho_{\mathrm{f}}\omega^2[S]^T \\
[0] & -\kappa_{\mathrm{f}}[Q_{\mathrm{f}}] & -[S] & [H_{\mathrm{f}}]]
\end{bmatrix}
\begin{Bmatrix} \{u\} \\ \{p\} \\ \{w\} \\ \{v\} \end{Bmatrix}
=
\begin{Bmatrix} \{P_{\mathrm{s}}\} \\ \{0\} \\ -\kappa_{\mathrm{s}}\{R_{\mathrm{s}}\} \\ -\kappa_{\mathrm{f}}\{R_{\mathrm{f}}\} \end{Bmatrix}
\tag{2.23}
$$

where the sub-matrices and vectors in the system are defined as

$$[H_{\mathrm{s}}] = [K_{\mathrm{s}}] - \omega^2 [M_{\mathrm{s}}], \qquad [H_{\mathrm{f}}] = [K_{\mathrm{f}}] + i\omega [C_{\mathrm{f}}] - \omega^2 [M_{\mathrm{f}}]$$

$$[K_{\mathrm{s}}] = \sum_{\text{elements}} \int_{\Omega_{\mathrm{s}}^e} [B_{\mathrm{s}}]^T [C] [B_{\mathrm{s}}] \, d\Omega, \qquad [K_{\mathrm{f}}] = \sum_{\text{elements}} \int_{\Omega_{\mathrm{f}}^e} [B_{\mathrm{f}}]^T [B_{\mathrm{f}}] \, d\Omega$$

$$[M_{\mathrm{s}}] = \sum_{\text{elements}} \int_{\Omega_{\mathrm{s}}^e} \rho_{\mathrm{s}} [N_{\mathrm{s}}]^T [N_{\mathrm{s}}] \, d\Omega, \qquad [M_{\mathrm{f}}] = \sum_{\text{elements}} \int_{\Omega_{\mathrm{f}}^e} \frac{\rho_{\mathrm{f}}}{K} [N_{\mathrm{f}}]^T [N_{\mathrm{f}}] \, d\Omega$$

$$[Q_{\mathrm{s}}] = \sum_{\text{elements}} \int_{\Omega_{\mathrm{s}}^e} [N_{\mathrm{s}}]^T [N_{\mathrm{s}}] \, d\Omega, \qquad [Q_{\mathrm{f}}] = \sum_{\text{elements}} \int_{\Omega_{\mathrm{f}}^e} [N_{\mathrm{f}}]^T [N_{\mathrm{f}}] \, d\Omega$$

$$[S] = \sum_{\text{elements}} \int_{\Gamma_{\mathrm{fs}}^e} [N_{\mathrm{f}}]^T \boldsymbol{n}_{\mathrm{f}}^T [N_{\mathrm{s}}] \, dS, \qquad [C_{\mathrm{f}}] = (i\omega)^{-1} \sum_{\text{elements}} \int_{\partial\Psi_R^e} f \, (ik + \beta) \, [N_{\mathrm{f}}]^T [N_{\mathrm{f}}] dS$$

$$\{R_{\mathrm{s}}\} = \sum_{\text{elements}} \int_{\Omega_{\mathrm{s}}^e} [N_{\mathrm{s}}]^T \boldsymbol{u}^m d\Omega_{\mathrm{s}}, \qquad \{R_{\mathrm{f}}\} = \sum_{\text{elements}} \int_{\Omega_{\mathrm{f}}^e} [N_{\mathrm{f}}]^T p^m d\Omega_{\mathrm{s}}$$

$$\{P_{\mathrm{s}}\} = \sum_{\text{elements}} \int_{\Gamma_t^e} [N_{\mathrm{s}}]^T \boldsymbol{t} \, dS + \sum_{\text{elements}} \int_{\Gamma_{fs}^e} [N_{\mathrm{s}}]^T \boldsymbol{g} \, dS$$

where $[C]$ is the linear elastic constitutive matrix in Voigt notation. Here, the expressions for $[Q_{\mathrm{s}}], [Q_{\mathrm{f}}], \{R_{\mathrm{s}}\}$, and $\{R_{\mathrm{s}}\}$ assume that the full fields are available for the measurement data $\boldsymbol{u}^m$ and p^m. In the case where only sparse data is available, the matrices $[Q_{\mathrm{s}}]$ and $[Q_{\mathrm{f}}]$ are replaced with diagonal Boolean matrices whose non-zero entries correspond to degrees of freedom that have been measured. Likewise, the vectors $\{R_{\mathrm{s}}\}$ and $\{R_{\mathrm{s}}\}$ are modified to contain the measurement values at those degrees of freedom and zeros elsewhere. It is noted that the equations in (2.23) can easily be rearranged to yield a complex symmetric matrix, but the system remains indefinite. In this study, we employ the parallel, direct linear solver PARDISO [30, 31] which provides efficient solutions to such systems.

Step (ii): constitutive update This step consists in solving equation (2.21e) for $\mathbb{C}$, with $\boldsymbol{u}, \boldsymbol{w}, p, v$ set to the solution of step (i). As shown in [3], this reduces to explicit update formulas when considering isotropic linear elastic materials, for

which the elasticity tensor can be expressed in terms of the bulk modulus B and the shear modulus G as

$$\mathbb{C} = \left(B - \frac{2}{3}\right)(\boldsymbol{I} \otimes \boldsymbol{I}) + 2G\mathbb{I} \tag{2.24}$$

(with $\boldsymbol{I}$ and $\mathbb{I}$ denoting the second and fourth order identity tensor, respectively).

The update formulae for B and G are obtained by first decoupling the stress and strain tensors into deviatoric and volumetric components

$$\boldsymbol{\sigma} = \boldsymbol{\sigma}_d + \hat{p}\boldsymbol{I}, \qquad \boldsymbol{\varepsilon}[\boldsymbol{u}] = \boldsymbol{\varepsilon}_d[\boldsymbol{u}] + \frac{1}{3}\hat{e}_u\boldsymbol{I}$$

where $\boldsymbol{\sigma}_d$ and $\boldsymbol{\varepsilon}_d$ are the deviatoric stress and strain tensors, respectively, $\hat{p} = \frac{1}{3}\operatorname{tr}(\boldsymbol{\sigma})$ is the mean stress and $\hat{e}_u = \operatorname{tr}(\boldsymbol{\varepsilon}[\boldsymbol{u}])$ is the volumetric strain. Then, we can enforce the optimality condition (2.21e) directly in terms of the bulk and shear modulus: $\langle \mathcal{L}'_B, \hat{B}\rangle = 0$ and $\langle \mathcal{L}'_G, \hat{G}\rangle = 0$, obtaining at iteration $n+1$

$$B^{n+1} = \frac{(\hat{p},\hat{p})^{1/2}}{(\hat{e}_u,\hat{e}_u)^{1/2}} = B^n \frac{(\hat{e}_u+\hat{e}_w,\hat{e}_u+\hat{e}_w)^{1/2}}{(\hat{e}_u,\hat{e}_u)^{1/2}} \tag{2.25a}$$

$$G^{n+1} = \frac{(\boldsymbol{\sigma}_d,\boldsymbol{\sigma}_d)^{1/2}}{(\boldsymbol{\varepsilon}_d[\boldsymbol{u}],\boldsymbol{\varepsilon}_d[\boldsymbol{u}])^{1/2}} = G^n \frac{(\boldsymbol{\varepsilon}_d[\boldsymbol{u}+\boldsymbol{w}],\boldsymbol{\varepsilon}_d[\boldsymbol{u}+\boldsymbol{w}])^{1/2}}{(\boldsymbol{\varepsilon}_d[\boldsymbol{u}],\boldsymbol{\varepsilon}_d[\boldsymbol{u}])^{1/2}} \tag{2.25b}$$

where the second equality results from the dependence of $\boldsymbol{\sigma}$ on both $\boldsymbol{u}$ and $\boldsymbol{w}$ as in Equation (2.20). We note that these pointwise material update formulas can be easily extended to update portions of the domain by using inner products in (2.25) defined over the desired regions. This is useful, for example, in inverse problems involving homogeneous materials with known geometries where one seeks only the elastic parameters defining each region rather than the spatial variation of these parameters.

In summary, the MECE inverse problem for ASI in Eq. (2.16) is solved by first forming the Lagrangian functional in (3.26). Then, by taking directional

derivatives of the Lagrangian with respect to the unknown mechanical fields, the Lagrange multipliers, and the constitutive tensor, we arrive at the coupled set of equations in (2.20) and (2.21), representing the first-order optimality conditions. A block Gauss-Seidel solution strategy is adopted to solve this set of equations by alternating between the solution of Equations (2.21a) - (2.21d) with the current value of $\mathbb{C}$ and then Equation (2.21e) with the updated values of $\boldsymbol{u}$, p, $\boldsymbol{w}$, v, and $\boldsymbol{\sigma}$. We reiterate that in practice, one iteration of this Gauss-Seidel algorithm amounts to solving the block system in (2.23), evaluating the stress field using (2.20), and then updating the elastic moduli using (2.25).

Remark 1 *The MECE minimization strategy is easily adaptable to situations where measurement data is acquired at multiple frequencies by defining the MECE functional as*

$$\bar{\Lambda}(\boldsymbol{u}_1, \ldots, \boldsymbol{u}_N, \boldsymbol{\sigma}_1, \ldots, \boldsymbol{\sigma}_N, p_1, \ldots, p_N, \mathbb{C}) = \sum_{i=1}^{N} \Lambda_i(\boldsymbol{u}_i, \boldsymbol{\sigma}_i, p_i; \mathbb{C}) \tag{2.26}$$

where data is obtained at the frequencies $\{\omega_i\}_{i=1}^N$ *and* Λ_i *depends on* ω_i *through the data at that frequency. A MECE iteration hence consists of solving equations* (2.21a)–(2.21d) *for each frequency (with* $\Lambda = \Lambda_i$*, yielding fields* $\boldsymbol{u}_i, \boldsymbol{w}_i, p_i, v_i$*), followed by a constitutive update where (for the isotropic case) the right-hand sides in* (2.25) *are summed over the relevant frequencies.*

Remark 2 *The block Gauss-Seidel strategy described above can be instead interpreted as an alternating minimization method [3], since steps (i) and (ii) are the stationarity equations for the partial minimization of the MECE functional with moduli* $\mathbb{C}$ *fixed (to the previous iterate) and with fields* $\boldsymbol{u}, \boldsymbol{w}, p, v$ *fixed (to their latest value), respectively.*

Remark 3 *Methods based on Newton or quasi-newton approaches [13] may also be used to solve the MECE optimization problem* (2.16)*. These approaches have received*

little or no attention in the current literature related to ECE-type methods and present an interesting future direction to investigate.

2.3 Weighting parameter selection and regularization in MECE

In this section, we discuss the role and adjustment of the weighting parameters, κ_{s} and κ_{f}, in the MECE functional (2.12). These parameters, which define the balance between minimizing the ECE (2.13) and matching the experimental data, are of great importance in the quality of the reconstruction of $\mathbb{C}$. In that respect, the MECE functional (2.12) is analogous to a regularized cost functional [11, 20], with regularization provided by the ECE term. In this analogy, κ_{s} and κ_{f} act as reciprocals of regularization parameters in the usual sense.

We now introduce some additional notation to facilitate the discussion to follow. First, to ensure consistent units (i.e. energy) and proper scaling among the components of the MECE functional (2.12), the coefficients κ_{s} and κ_{f} are recast in the following form, as proposed in [3]:

$$\kappa_{\mathrm{s}} = \alpha_{\mathrm{s}} A_{\mathrm{s}}, \quad \kappa_{\mathrm{f}} = \alpha_{\mathrm{f}} A_{\mathrm{f}}, \qquad \text{with} \quad A_{\mathrm{s}} := \frac{U(\mathbb{C}_0)}{\|\boldsymbol{u}^m\|^2_{L^2(\Omega_{\mathrm{s}}^m)}}, \quad A_{\mathrm{f}} := \frac{U(\mathbb{C}_0)}{\|p^m\|^2_{L^2(\Omega_{\mathrm{f}}^m)}} \tag{2.27}$$

where $U(\mathbb{C}_0)$ is the strain energy in the solid system of the solution of the forward problem (2.1)–(2.4) with the initial guess $\mathbb{C} = \mathbb{C}_0$ and $\alpha_{\mathrm{s}}, \alpha_{\mathrm{f}}$ are non-dimensional weighting parameters. Moreover, let $\boldsymbol{u}_\alpha, \boldsymbol{\sigma}_\alpha, p_\alpha$ and $\mathbb{C}_\alpha$ denote the fields and elastic moduli obtained upon convergence of the minimization problem (2.16) for given $\alpha := (\alpha_{\mathrm{s}}, \alpha_{\mathrm{f}})$. The converged values of the ECE, displace-

ment misfit and pressure misfit components of the MECE functional (2.12) are

$$U(\alpha) := U(\boldsymbol{u}_\alpha, \boldsymbol{\sigma}_\alpha, \mathbb{C}_\alpha), \qquad D_{\mathrm{s}}(\alpha) := \tfrac{1}{2} A_{\mathrm{s}} \|\boldsymbol{u}_\alpha - \boldsymbol{u}^m\|^2_{L^2(\Omega_{\mathrm{s}}^m)}, \qquad D_{\mathrm{f}}(\alpha) := \tfrac{1}{2} A_{\mathrm{f}} \|p_\alpha - p^m\|^2_{L^2(\Omega_{\mathrm{f}}^m)}, \tag{2.28}$$

(with $A_{\mathrm{s}}, A_{\mathrm{f}}$ as defined in (2.27)) so that the converged MECE value $\Lambda(\alpha)$ is given by

$$\Lambda(\alpha) = U(\alpha) + \alpha_{\mathrm{s}} D_{\mathrm{s}}(\alpha) + \alpha_{\mathrm{f}} D_{\mathrm{f}}(\alpha) \tag{2.29}$$

Adjusting the MECE weighting coefficients is now a matter of finding an effective strategy for setting $\alpha_{\mathrm{s}}, \alpha_{\mathrm{f}}$. As α_{s}, α_{f} are increased, $D_{\mathrm{s}}(\alpha)$ and $D_{\mathrm{f}}(\alpha)$ decrease: greater emphasis is put on reducing the L^2 data discrepancies and the measured data is approximated more closely (but so is the measurement noise). Alternatively, decreasing α_{s}, α_{f} yields reconstructions that better reduce the ECE, i.e. emphasize the satisfaction of the constitutive relation (2.3), while eventually losing important information contained in the measured data. Since α_{s} and α_{f} ultimately decide the tradeoff between over-smoothing a solution and over-fitting noisy input data, selecting appropriate values is akin to regularization with the MECE algorithm. We present two strategies for the selection of $\alpha_{\mathrm{s}}, \alpha_{\mathrm{f}}$. The first is based on the discrepancy principle of Morozov [20, 12], a well-established approach which assumes the level of noise in the data to be known *a priori*. In the second approach, applicable to cases with unknown noise, $\alpha_{\mathrm{s}}, \alpha_{\mathrm{f}}$ are selected by minimizing an error-balance function that we propose on the basis of heuristic considerations.

Adjustment method 1: Morozov discrepancy principle. This approach, which assumes that the level of noise δ in the measurement data is known, exploits the discrepancy principle of Morozov [20, 12]. Here, the parameter α is

chosen to be the smallest positive number such that the final discrepancy between the computed and measured system response is at the level of the noise. This amounts (considering displacement data for definiteness) to choosing α such that

$$\frac{\|\boldsymbol{u}_\alpha - \boldsymbol{u}^m\|_{L^2(\Omega_{\mathrm{s}}^m)}}{\|\boldsymbol{u}^m\|_{L^2(\Omega_{\mathrm{s}}^m)}} = c\delta, \tag{2.30}$$

where c is a constant (taken as $c = 1$ in this work). This strategy is implemented by solving the inverse problem for increasing values of α (starting from a very low value) until condition (2.30) is met within a chosen tolerance.

Adjustment method 2: error balance. For the situation when the noise level δ on the data is unknown, we now propose an approach for weighting parameter selection that is based on an error-balance between the terms in the converged MECE functional (2.29). The underlying, heuristic, idea is to adjust α so as to strike a balance between the minimization of the different components of the MECE functional, hoping to achieve a satisfactory tradeoff between over-smoothing the solution (over-emphasis on ECE minimization) and over-fitting the data (over-emphasis on data discrepancy minimization). In practice, we propose to choose α so as to minimize the following error-balance function $\mathcal{J}(\alpha)$:

$$\mathcal{J}(\alpha) := U^2(\alpha) + D_{\mathrm{s}}^2(\alpha) + D_{\mathrm{f}}^2(\alpha) \tag{2.31}$$

In this work, we adopt a simple approach to approximate that value of α. The optimization problem (2.16) is solved for multiple values of α in a predetermined range, yielding corresponding values for $U(\alpha)$, $D_{\mathrm{s}}(\alpha)$, $D_{\mathrm{f}}(\alpha)$. The optimal value of $\mathcal{J}(\alpha)$ is then obtained by solving a one-dimensional minimization problem. Although this approach seems very computationally expensive, in practice solutions for different values of α are independent and can be obtained

simultaneously through parallel solutions of optimization problems (2.16). An adaptive approach for determining more efficiently an optimal value of α is highly desirable and will be pursued in future work.

2.4 Numerical results

In this section, we apply the MECE algorithm to estimate unknown material properties in ASI systems for three different examples. We consider nearly-incompressible materials assuming a known bulk modulus equal to that of the surrounding fluid medium and seek to recover an unknown shear modulus field throughout the solid domain. The mean-dilatation approach [19] is used to handle near-incompressibility. We examine the case where the full displacement field is measured as well as the case where displacement data is only available in one direction. We also test the performance of the algorithm in recovering elastic parameters given pressure measurements in the fluid domain. In all examples, we add random noise to the inverse problem data to simulate the measurement errors that are inherent in practice. Denoting the synthetic (computed and interpolated) displacement at a node i as $\hat{u}_i$, the corresponding noisy measurement u_i^m is given as

$$u_i^m = \hat{u}_i(1 + \delta r_i), \tag{2.32}$$

where r_i is a normal random variable with zero mean and unit variance and the parameter δ is a prescribed relative noise level. In our examples, we use $\delta = 0.01, 0.03$, and 0.05.

In Example 1, we consider a two-dimensional problem where the shear modulus field is estimated using incomplete and noisy displacement data in the

solid domain. Example 2 is another two-dimensional problem in which the shear modulus of three different materials with geometries that are known *a priori* are recovered using sparse pressure measurements from sensors within the fluid domain. In Example 3, we image a shear modulus field in a three-dimensional acoustic-structure system using a full displacement field.

Remark 4 *The frequencies in the examples presented herein were chosen so as to maintain a low shear wavenumber in the solid. This choice was made without loss of generality and in the interest of avoiding excessively fine meshes. Notice that because of the large differences in the bulk and shear moduli, the wavelengths in the fluid are very large as compared to the solid domain. This fact is not a problem when pressure is used to identify shear moduli as long as the pressure field remains sensitive to changes in the material.*

2.4.1 Example 1: 2D imaging with displacement data

We consider a two-dimensional acoustic-structure system in which a square solid domain under plane strain conditions is submerged in an infinite fluid medium. We seek to use the noisy and incomplete (i.e. one-directional) displacement response of the solid under an applied traction to recover the unknown shear modulus field. We study the quality of the reconstruction for varying levels of data noise and illustrate the performance of both the discrepancy principle and the error-balance technique for choosing the weight α_{s}.

A sketch of the problem domain for this example can be seen in Figure 2.1(a). The fluid medium has been truncated using a circle of radius $R = 0.1\,\mathrm{m}$ on which the non-reflecting radiation condition (2.4c) has been specified. The solid

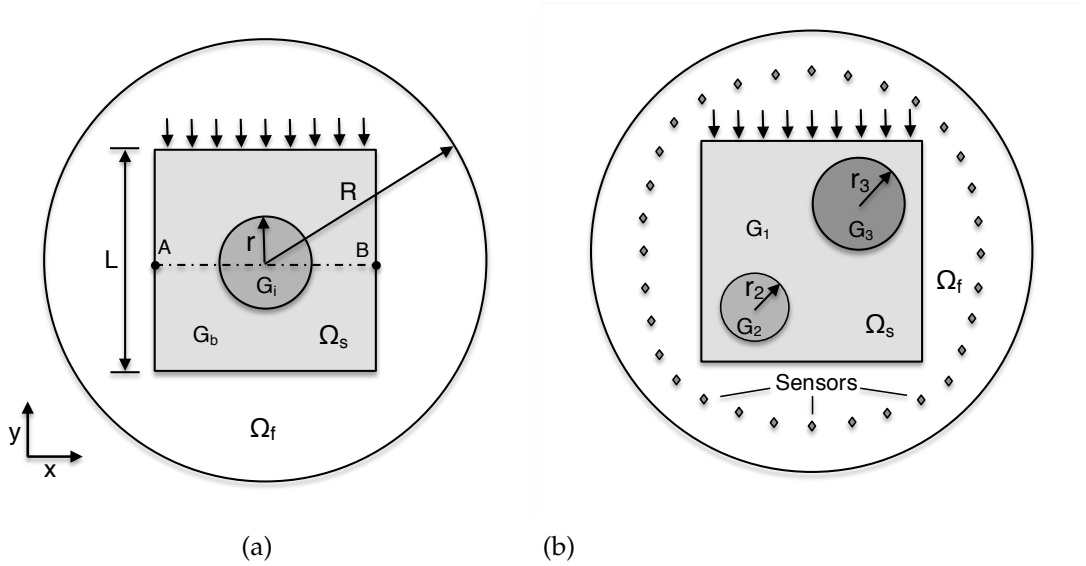

(a) (b)

Figure 2.1: Diagrams of the problem domains in (a) Example 1 and (b) Example 2.

domain is a square with sides of length $L = 0.1\,\text{m}$ containing a centered, circular inclusion with radius $r = 0.02\,\text{m}$. A uniform traction $\boldsymbol{g} = -g\boldsymbol{e}_y$, with $g = 10^3\,\text{N/m}$, is applied in the y-direction along the top surface of the solid. The coupling conditions (2.1c) and (2.4d) are present along the solid-fluid interface. The mass density and bulk modulus are assumed to be constant and the same for both the fluid and solid domains: $\rho_\text{f} = \rho_\text{s} = 1000\,\text{kg/m}^3$ and $K = B = 2.2 \times 10^9\,\text{Pa}$. We consider an inclusion shear modulus (G_i) that is four times stiffer than that of the background material (G_b): $G_i = 4G_b = 6.0 \times 10^4\,\text{Pa}$.

The displacement data used for the inverse problem is generated artificially by solving the coupled ASI problem (Equations (2.1) to (2.4)) with the true shear moduli on an unstructured finite element mesh with $70,000$ nodes. For the solution of the inverse problem with MECE, however, a coarser mesh with $12,000$ nodes is used, where the solid domain is a uniform 58×58 grid (i.e. the geometry of the inclusion is not explicity meshed). Both meshes are made of four-node,

bilinear elements. The displacement within the solid domain is interpolated from the finer mesh to the coarser mesh, which avoids committing the "inverse crime" and deliberately introduces a modeling error. Only those displacements in the y-direction are then kept as data to recover the shear modulus. The data is collected for two frequencies ($f = 40.0, 50.0\,\text{Hz}$), and thus the whole input data for the problem consists of $6,738$ displacement measurements.

Shear reconstructions using the discrepancy principle

The inverse problem (2.16) is first solved using the discrepancy principle of Morozov, i.e. selecting α_s such that equation (2.30) is approximately satisfied for $c = 1$ when the MECE algorithm has converged (note that for this example $\alpha_\text{f} = 0$). We note that in this study, the algorithm is deemed to have converged when the relative change in the functional (2.12) between two successive iterations is below 1%. For the following results, an initial guess of $G^0 = G_b = 1.5 \times 10^4\,\text{Pa}$ is used for the shear modulus throughout the entire solid domain. The effect of measurement error on the recovered shear modulus is studied by considering solutions to the inverse problem in the presence of three different levels of noise (1%, 3%, and 5%).

Noise	α_s	Relative discrepancy	Iterations
1%	8000	$1.00e$-2	5
3%	40	$3.04e$-2	21
5%	1.5	$5.06e$-2	21

Table 2.1: The value of MECE weight α_s selected for each noise level using the discrepancy principle (2.30) along with the final value of the relative discrepancy (l.h.s. of (2.30)) and the number of iterations it took for the MECE algorithm to converge

The selected value of α_s for each noise level considered is given in Table 2.1, together with the final value of the relative discrepancy between the measured and computed displacements (left hand side of (2.30)) when the algorithm converged and the number of MECE iterations until convergence. As expected, the selected value of α_s increases as the noise level δ decreases. This is due to the fact that higher weight (larger α_s) is needed on the discrepancy term of the MECE functional (2.12) for the minimization to reach lower thresholds in the discrepancy equation (2.30). Note also that the higher value of α_s for the case of 1% caused faster convergence (5 iterations versus 21 for 3% and 5% noise), an observation that is consistent with earlier work [3].

The shear modulus field estimates for each noise level, with α_s obtained using the discrepancy principle, are displayed in Figure 2.2. Figure 2.2(a) shows the solutions for each noise level plotted across line AB of Figure 2.1(a) compared with the reference solution. Figures 2.2(b,c,d) show the two-dimensional recovered shear modulus field for 1%, 3%, and 5% noise levels, respectively. It can be seen that the level of accuracy for the case of 3% and 5% noise is comparable, while the solution for 1% noise is more accurate, as expected. Indeed, Figure 2.2(a) shows that the true magnitude of the inclusion shear modulus is slightly overestimated for the higher noise levels. Additionally, the two-dimensional plots show that the boundary of the inclusion is more distinctly identified for 1% noise than for the higher noise levels. Generally speaking, however, the solutions for each case provide satisfactory estimates of the background and inclusion shear modulus and accurately resolve the boundary between the materials.

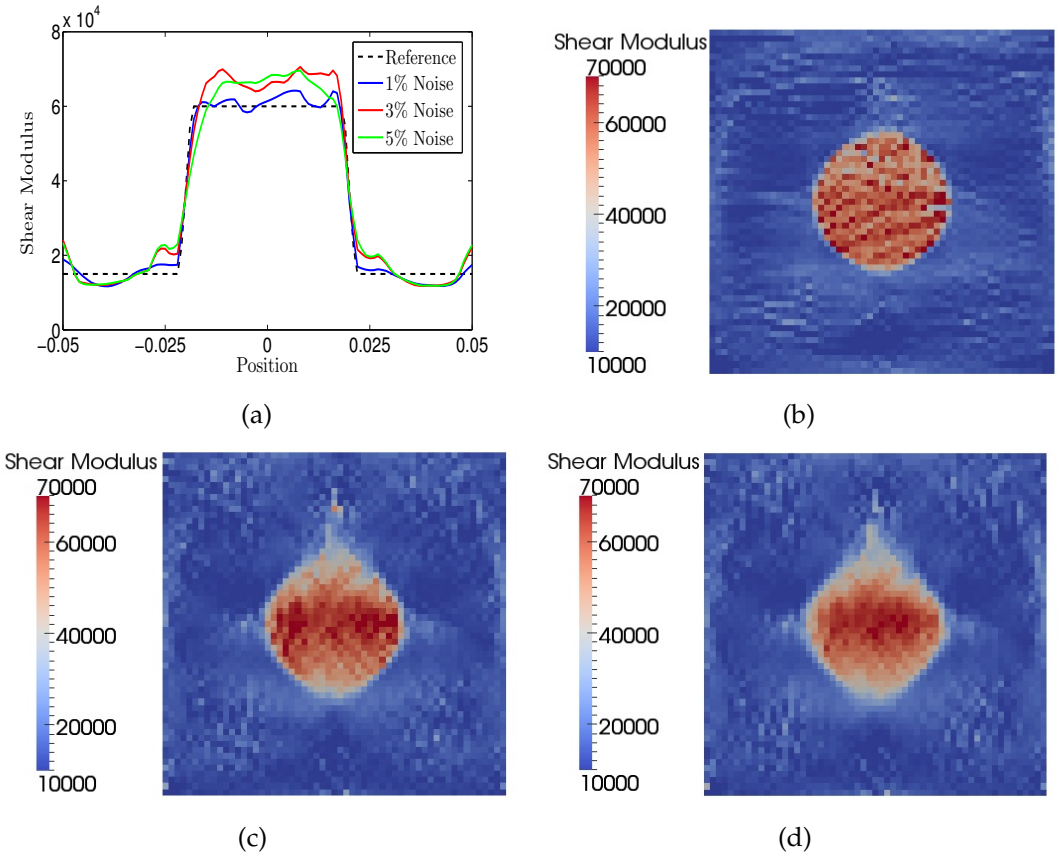

Figure 2.2: Shear reconstruction, MECE weight α_s selected using the discrepancy principle. (a) The solution for each noise level, plotted along line segment AB of Fig. 2.1(a). (b) Recovered shear field for 1% noise. (c) 3% noise. (d) 5% noise. Units: Pa, m

Shear reconstructions using error balance

We now demonstrate the use of the error balance approach for selecting α_s. For comparison purposes, the problem setup described in Section 2.4.1 remains unchanged. To carry out the approach, the inverse problem (2.16) is solved for weighting coefficients sampling the range $0.1 \leq \alpha_s \leq 100$, and postprocessing is done to find the value of α_s that minimizes the error balance function $\mathcal{J}(\alpha_s)$ defined by (2.31). The resulting plot of $\mathcal{J}$ versus α_s, displayed in Figure 2.3 for the different noise levels, shows that the method selects α_s to be 5, 10, and 10 for

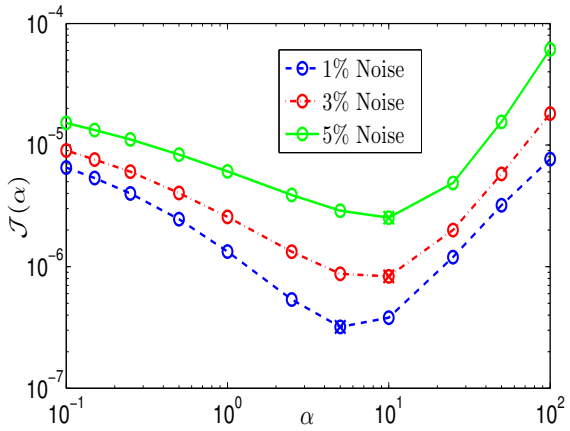

Figure 2.3: The error-balance function $\mathcal{J}$ (Eq. (2.31)) versus α_s, with minimum values denoted with an "$\times$".

1%, 3%, and 5% noise, respectively.

The corresponding shear field reconstructions for each noise level using the error balance approach are shown in Figure 2.4. As in the previous section, the solutions are compared with the reference along line AB in Figure 2.4(a), while Figures 2.4(b,c,d) show the two-dimensional estimated shear modulus fields for 1%, 3%, and 5% noise levels, respectively. Again, the relative accuracy of the recovered fields are satisfactory for each noise level in terms of the estimated magnitudes for each material as well as the resolution of the boundary between them. The line plots in Figure 2.4(a) show that the higher noise levels tend to overestimate the inclusion shear modulus more so than the case of 1% noise. However, it can be seen in this plot, as well as in Figures 2.4(b,c,d), that the inclusion geometry is more accurately identified for 3% and 5% noise than for 1% noise. The latter observation seems to be a reflection of the error-balance approach producing a weight parameter value that is too small for the lowest noise level case, further emphasizing the non-optimal nature of the approach.

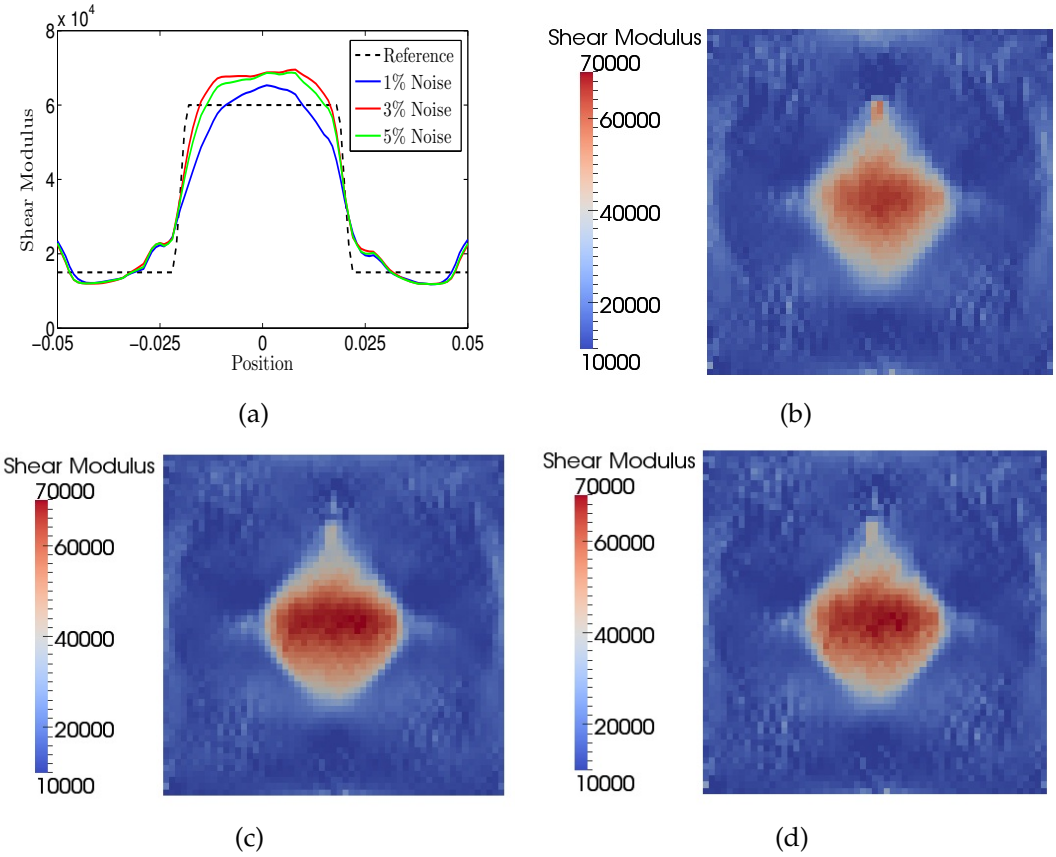

Figure 2.4: Shear reconstruction, MECE weight α_s selected using error balance. (a) The solution for each noise level, plotted along line segment AB of Fig. 2.1(a). (b) Recovered shear field for 1% noise. (c) 3% noise. (d) 5% noise. Units: Pa, m

Comparison of discrepancy principle and error balance solutions

The relative performance of using the discrepancy principle versus the error balance approach for selecting the weighting coefficient is now discussed. To facilitate a comparison of the accuracy between the two methods, the solution error is computed for a wide range of α_s values for each noise level. The error metric used is a relative ℓ^2 norm over the elements in the solid domain, given as

$$\hat{E}_G(\alpha_s) = \frac{\sum_{i=1}^{\text{NE}} \left| G_{\text{true}}^{(i)} - G_{\text{est}}^{(i)}(\alpha_s) \right|^2}{\sum_{i=1}^{\text{NE}} \left| G_{\text{true}}^{(i)} \right|^2} \tag{2.33}$$

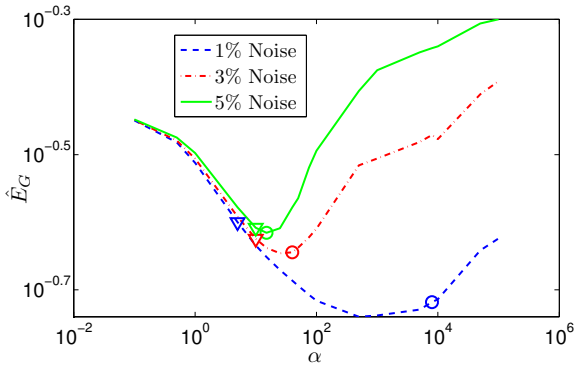

Figure 2.5: The shear reconstruction error (2.33) versus α_s for different noise levels in Example 1. The circle and triangle markers denote the values of α_s selected using the discrepancy principle and the error balance technique, respectively

where NE is the number of elements in the solid domain and $G_{\text{true}}^{(i)}$ is simply 1.5×10^4 Pa or 6.0×10^4 Pa depending on whether the centroid of element i falls within the background or inclusion material, respectively.

Figure 2.5 shows $\hat{E}_G(\alpha_s)$ plotted against α_s for each noise level. In addition, the values for α_s selected using the discrepancy principle are indicated by circle markers, while those selected using the error balance approach are marked by triangles. For each noise level, it can be seen that the discrepancy principle produces a value of α_s that is closer to the optimal value $\alpha_s^\star$ (such that $\hat{E}_G(\alpha_s^\star)$ is the lowest possible solution error for a given data set) than the error balance approach . Indeed, using the discrepancy principle leads to values of α_s that are very close to optimal for 3% and 5% noise, and although it is farther off for 1% noise, the resulting error $\hat{E}_G$ is still close to its optimal value $\hat{E}_G(\alpha_s^\star)$. On the other hand, the error balance method yields choices of α_s that are also near optimal for 3% and 5% noise but significantly far from the optimal value for 1% noise. Furthermore, the error balance selection of α_s appears to be relatively insensitive to the noise level, which is a drawback of the approach.

The results from this example suggest that using the discrepancy principle to select the MECE weighting coefficient outperforms the error balance approach. The solutions for all noise levels using each method appear to be satisfactory in Figures 2.2 and 2.4, but the rigorous error comparison in Figure 2.5 shows that, in terms of accuracy, the discrepancy principle outperforms the error-balance approach. Perhaps more significant than the difference in accuracy is the trending behavior of each method for varying noise levels. The discrepancy principle yields values of α_{s} that increase consistently with decreasing noise, following the same expected trend as the optimal value $\alpha_{\mathrm{s}}^{\star}$. The error balance approach shows little variance for different noise levels and follows the opposite trend, selecting a slightly smaller weighting coefficient for 1% noise. Of course, employing the discrepancy principle in practice requires *a priori* knowledge of the noise level, while the error balance approach does not. Hence, we reiterate that the main appeal of the latter method is its generality and argue that in the absence of information about noise level, it represents a viable approach for selecting the weighting parameter.

2.4.2 Example 2: 2D modulus estimation with pressure data

We again consider a two-dimensional acoustic-structure system that consists of a square solid domain under the plane strain assumption submerged in an infinite fluid medium, see Figure 2.4.1. In this case, however, we use sparse and noisy measurements of the acoustic pressure in the fluid to estimate the elastic properties of the solid. The latter is made of two inclusions of different size and material embedded in the background matrix and thus involves three homogeneous materials whose spatial distribution is assumed to be known. Taking the

center of the square as the origin, material two is centered at (-0.025 m,-0.025 m) with radius $r_2 = 0.015$ m and material three is centered at (0.02 m,0.02 m) with radius $r_3 = 0.02$ m (Fig. 2.4.1).

The boundary conditions and dimensions of the solid and fluid domains, as well as the material properties of the fluid and the bulk modulus of the solid, are as in Example 1, while the shear modulus values are: $G_1 = 1.5 \times 10^4$ Pa, $G_2 = 3.0 \times 10^4$ Pa, and $G_3 = 6.0 \times 10^4$ Pa. The acoustic pressure is measured at thirty-two sensors spaced evenly on a ring in the fluid domain. The system is excited at a frequency of 40.0 Hz.

The inverse problem reduces to estimating the values G_1, G_2, G_3 of the shear moduli in the background and inclusions. The relevant MECE weight α_{f} is selected using both the discrepancy principle and the error balance approach. The pressure data for the inverse problem is generated by solving the forward problem with true moduli values, storing the pressure values at sensor locations, and adding artificial noise according to (2.32) with $\boldsymbol{u}^m$ replaced by p^m. The forward problem is solved on a finite element mesh with $54,000$ nodes while a coarser mesh with $17,000$ nodes is used for the inverse problem. In this case, the inclusions are meshed in the grid used for the inversion since a known spatial distribution of moduli is assumed.

The unknown moduli $\vec{G} = [G_1\ G_2\ G_3]^T$ are estimated using a uniform initial guess $G^0 = 1.5 \times 10^4$ Pa with pressure data polluted with 1%, 3%, and 5% noise. The relative solution accuracy is defined as

$$\bar{E}_G(\alpha_{\mathrm{f}}) = \frac{\|\vec{G}_{\text{true}} - \vec{G}_{\text{est}}(\alpha_{\mathrm{f}})\|}{\|\vec{G}_{\text{true}}\|}, \tag{2.34}$$

The value of $\bar{E}_G(\alpha_{\mathrm{f}})$ is plotted versus α_{f} for each noise level in Figure 2.6, with the values of α_{f} selected using the discrepancy principle (1.5, 0.2, and 0.1 for

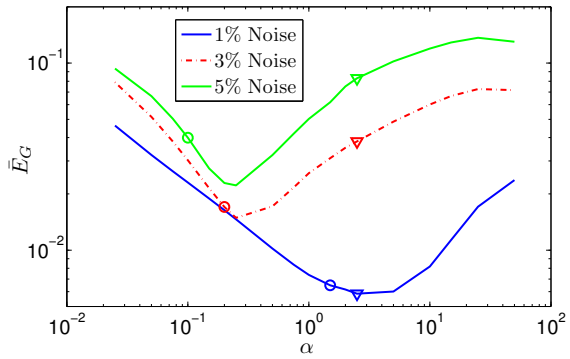

Figure 2.6: The relative error (2.34) in the estimated shear moduli versus α_{f} for different noise levels in Example 2. The circle and triangle markers denote the values of α_{f} selected using the discrepancy principle and the error balance technique, respectively.

1%, 3%, and 5% noise, respectively) and the error balance approach (2.5 for each noise level), respectively, indicated by circles and triangles.

Selecting α_{f} using the discrepancy principle produces significantly more accurate solutions for 3% and 5% noise levels while the error balance solution is slightly more accurate for 1% noise. As in Example 1, α_{f} increases as the noise level δ decreases when selected using the discrepancy principle, but is insensitive to δ when selected using error balance. Reconstruction errors $\bar{E}_G(\alpha_{\mathrm{f}})$ increase with δ for both weight adjustment methods, as expected. The overall identification accuracy is nevertheless satisfactory for all considered cases, with all relative errors on individual moduli found to be below 10% and most of them well below 5%.

We mention in passing that we also studied the effect of different initial guesses of shear moduli on the accuracy of the resulting reconstructions for the current example. We found that the behavior of the proposed algorithm was insensitive to the initial guess (at least for the current example). Furthermore, the results reported above for the error balance and discrepancy principle ap-

proaches remained the same.

We note that the pointwise reconstruction of the shear modulus field without assuming known geometry *a priori* may not be feasible with the current problem setup. This is because having pressure data is akin to having only surface displacement measurements, and therefore less information is available about the unknown shear moduli than when interior solid data is available. A pointwise reconstruction of the shear field might be feasible using pressure data collected for a range of frequencies and different loading configurations; e.g. when using approaches similar to those found in seismic imaging. However, this is beyond the scope of this work.

2.4.3 Example 3: 3D imaging with displacement data

The MECE algorithm is now applied to a larger scale, three-dimensional, inverse problem. Data consisting of the full displacement field in all directions is used to recover an unknown shear modulus in a solid cube with sides of length $L = 0.1\,\mathrm{m}$ and a centered spherical inclusion of radius $r = 0.02\,\mathrm{m}$. The infinite fluid domain is truncated by a sphere with radius $R = 0.1\,\mathrm{m}$ where the non-reflecting boundary condition (2.4c) is applied. The solid is excited with a uniform traction $\boldsymbol{g} = -g\boldsymbol{e}_y$, with $g = 10^4\,\mathrm{N/m^2}$ on the top surface at a frequency $f = 50.0\,\mathrm{Hz}$. The material properties in the fluid and solid are as in Example 1.

The displacement data used for the inverse problem is generated artificially by solving the coupled ASI problem (2.1)–(2.4) with the true shear moduli on a mesh with $43,000$. A coarser mesh with $27,000$ nodes ($13,000$ nodes in the solid) is then used for the inverse problem. Quadratic (10-node) tetahedral elements

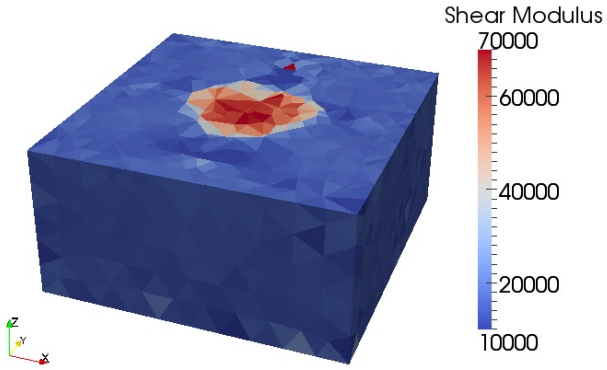

Figure 2.7: A clip plane contour plot of the recovered shear modulus in Example 3 for 3% noisy data. Units: Pa

were used in both meshes. The inverse problem was solved for noise levels of 1%, 3%, and 5% with an initial guess equal to the background shear modulus. In this example, only the discrepancy principle was used to select α_s, which yielded values of 50.0, 3.0, and 1.25 for 1%, 3%, and 5% noise, respectively.

Figure 2.7 shows the reconstructed shear modulus on its horizontal plane of symmetry, for the case of 3% noise. The inclusion is easily distinguished from the background matrix, with the estimated values of the shear modulus in each region in good agreement with their true couinterparts ($G_i = 6.0 \times 10^4$ Pa, $G_b = 1.5 \times 10^4$ Pa). A threshold plot shown in Figure. 2.8, in which all elements whose shear modulus is outside of the range 4.5×10^4 Pa $\leq G \leq 7.0 \times 10^4$ Pa are removed from view, gives a better sense of the reconstruction quality. The region occupied by the remaining thresholded elements is seen to coincide well with the true inclusion, whose meshed shape is shown for comparison.

Finally, a comparison of the estimated shear modulus distribution for different noise levels is shown in Figure 2.9. The solutions are plotted across the x-axis through the center of the solid domain and compared with the reference solu-

tion. As expected, the reconstruction accuracy somewhat declines, and the discontinuity between the two materials becomes in particular less well resolved, as the noise level is increased. The solution for each noise level nevertheless clearly identifies the embedded inclusion and provides satisfactory estimates of the shear moduli. Moreover, a low number of iterations of the MECE algorithm was found sufficient to achieve convergence to the solution of the optimality system for all values of α_s. For instance, the solutions for 1%, 3%, and 5% noise were obtained in 11, 19, and 17 iterations, respectively.

2.5 Conclusions

In this study, we proposed a framework for the inverse identification of material properties in frequency-domain, coupled acoustic-structure interaction (ASI) systems using a modified error in constitutive equations (MECE) approach. Our formulation allows for both measurements of displacements in the solid and the acoustic pressure in the neighboring fluid to estimate the linear elastic parameters that define the solid. Furthermore, we demonstrated two different methods to select the MECE weighting coefficient: (i) the discrepancy principle of Morozov and (ii) an error-balance approach. The latter, which did not produce optimal results and was outperformed by the former from an accuracy standpoint, has the advantage of remaining effective (for practical purposes) even when the level of noise on the input data is unknown *a priori*. Overall, the numerical results in this paper showed the effectiveness of each approach in generating satisfactory reconstructions in the presence of noisy and incomplete data.

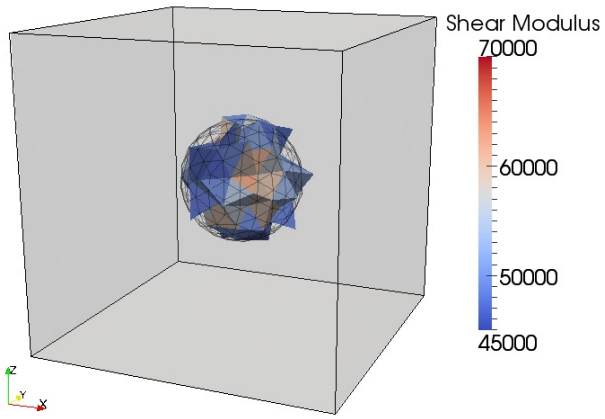

Figure 2.8: A threshold plot of the recovered shear modulus in Example 3 for 3% noisy data. The mesh outline of the true inclusion is shown for comparison. Units: Pa.

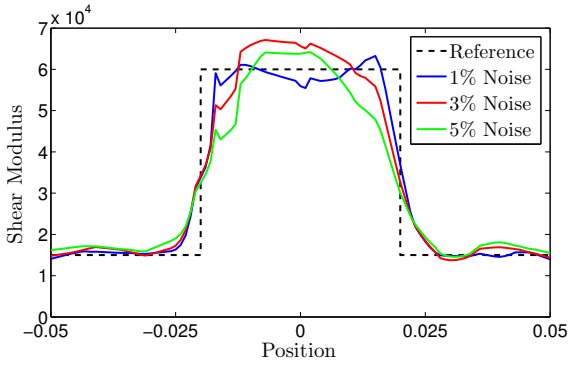

Figure 2.9: Comparison of the reconstructed shear moduli for different noise levels in Example 3 against the true shear modulus. Units: Pa, m

2.6 Acknowledgments

This work was partially supported by NIH Grants #EB002640 and #EB002167.

REFERENCES

[1] M. Aguilo, W. Aquino, J. C. Brigham, and M. Fatemi. An inverse problem approach for elasticity imaging through vibroacoustics. *IEEE Transactions on Medical Imaging*, 29(4):1012–1021, 2010.

[2] O. Allix, P. Feissel, and H. M. Nguyen. Identification strategy in the presence of corrupted measurements. *Engineering Computations*, 22:487–504, 2005.

[3] B. Banerjee, T. F. Walsh, W. Aquino, and M. Bonnet. Large scale parameter estimation problems in frequency-domain elastodynamics using an error in constitutive equation functional. *Comp. Meth. Appl. Mech. Eng.*, 253:60–72, 2013.

[4] H. T. Banks, M. L. Joyner, B. Wincheski, and W. P. Winfree. Real time computational algorithms for eddy-current-based damage detection. *Inverse Problems*, 18:795–823, 2002.

[5] D. Barthe, A. Deraemaeker, P. Ladevèze, and S. Le Loch. Validation and updating of industrial models based on the constitutive relation error. *American Institute of Aeronautics and Astronautics*, 42:1427–1434, 2004.

[6] K. J. Bathe. *Finite Element Procedures*. Prentice Hall, Pearson Education, Inc., USA, 2006.

[7] J. P. Berenger. A perfectly matched layer for the absorption of electromagnetic waves. *J. Comput. Phys.*, 114:185–200, 1994.

[8] M. Bernal, I. Nenadic, M. W. Urban, and J. F. Greenleaf. Material property estimation for tubes and arteries using ultrasound radiation force and analysis of propagating modes. *J. Acoust. Soc. Am.*, 129(3):1344–1354, 2011.

[9] J. C. Brigham and W. Aquino. Inverse viscoelastic material characterization using pod reduced-order modeling in acoustic-structure interaction. *Comp. Meth. Appl. Mech. Eng.*, 198:893–903, 2009.

[10] J. C. Brigham, W. Aquino, F. G. Mitri, Greenleaf J. F., and M. Fatemi. Inverse estimation of viscoelastic material properties for solids immersed in fluids using vibroacoustic techniques. *J. Appl. Phys.*, 101(23509):1–14, 2007.

[11] D. Calvetti, S. Morigi, L. Reichel, and F. Sgallari. Tikhonov regularization and the l-curve for large discrete ill-posed problems. *J. Comput. Appl. Math.*, 123:423–446, 2000.

[12] D. Colton and R. Kress. *Inverse Acoustic and Electromagnetic Scattering Theory*. Springer, Berlin, 1998.

[13] I. Epanomeritakis, V. Akcelik, O. Ghattas, and J. Bielak. A newton-cg method for large-scale three-dimensional elastic full-waveform seismic inversion. *Inverse Problems*, 24:034015 (26p), 2008.

[14] M. Fatemi and J. F. Greenleaf. Ultrasound-stimulated vibro-acoustic spectrography. *Science*, 280:82–85, 1998.

[15] M. Fatemi and J. F. Greenleaf. Vibro-acoustography: An imaging modality based on ultrasound-stimulated acoustic emission. *Proceedings of the National Academy of Sciences*, 96:6603–6608, 1999.

[16] P. Feissel and O. Allix. Modified constitutive relation error identification strategy for transient dynamics with corrupted data. *Comp. Meth. Appl. Mech. Eng.*, 196:1968–1983, 2007.

[17] J. F. Greenleaf, M. Fatemi, and M. Insana. Selected methods for imaging elastic properties in biological tissues. *Annual Review of Biomedical Engineering*, 5:57–78, 2003.

[18] M. Hinze, R. Pinnau, M. Ulbrich, and S. Ulbrich. *Optimization with PDE Constraints*. Springer, New York, 2009.

[19] T. J. R. Hughes. *The finite element method: linear static and dynamic finite element anaysis*. Dover Publications, Inc., Mineola, New York, USA, 2000.

[20] V. Isakov. *Inverse Problems for Partial Differential Equations*. Springer, New York, 1998.

[21] B. A. Kingwell and C. D. Gatzka. Arterial stiffness and prediction of cardiovascular risk. *Journal of Hypertension*, 20:2337–2340, 2002.

[22] P. Ladeveze and D. Leguillon. Error estimate procedure in the finite element method and applications. *SIAM J. Numer. Anal.*, 20:485–509, 1983.

[23] P. Ladevèze, D. Nedjar, and M. Reynier. Updating of finite element models using vibration tests. *AIAA Journal*, 32:1485–1491, 1994.

[24] S. Levasseur, Y. Malécot, M. Boulon, and E. Flavigny. Soil parameter identification using a genetic algorithm. *Int. J. Numer. Anal. Metho. Geomech.*, 32:189–213, 2007.

[25] R. Muthupillai, D. J. Lomas, P. J. Rossman, J. F. Greenleaf, A. Manduca, and R. L. Ehman. Magnetic resonance elastography by direct visualization of propogating acoustic strain waves. *Science*, 269(5232):1854–1857, 1995.

[26] A. A. Oberai, N. H. Gokhale, M. M. Doyley, and J. C. Bamber. Evaluation of the adjoint equation based algorithm for elasticity imaging. *Phys. Med. Biol.*, 49:2955–2974, 2004.

[27] D. B. Plewes, J. Bishop, A. Samani, and J. Sciarretta. Visualization and quantification of breast cancer biomechanical properties with magnetic resonance elastography. *Phys. Med. Biol.*, 45:1591–1610, 2000.

[28] E. Rosario, J. C. Brigham, and W. Aquino. Identification of material properties of orthotropic elastic cylinders immersed in fluid using vibroacoustic techniques. *Ultrasonics*, 48:547–552, 2008.

[29] Chen S., M. Fatemi, and J. F. Greenleaf. Quantifying elasticity and viscosity from measurement of shear wave speed dispersion. *J. Acoust. Soc. Am.*, 115(6):2781–2785, 2004.

[30] O. Schenk and K. Gärtner. Solving unsymmetric sparse systems of linear equations with pardiso. *Journal of Future Generation Computer Systems*, 20(3):475–487, 2004.

[31] O. Schenk and K. Gärtner. On fast factorization pivoting methods for symmetric indefinite systems. *Elec. Trans. Numer. Anal.*, 23:158–179, 2006.

[32] C. J. Stull, C. J. Earls, and P.S. Koutsourelakis. Model-based structural health monitoring of naval ship hulls. *Comp. Meth. Appl. Mech. Eng.*, 200:1137–1149, 2011.

CHAPTER 3

STOCHASTIC REDUCED ORDER MODELS FOR INVERSE PROBLEMS UNDER UNCERTAINTY

Co-authors: Wilkins Aquino and Mircea Grigoriu

Paper in preparation for submission to *Journal of Computational Physics*

Abstract

This work presents a novel approach for inverse problems under uncertainty using stochastic reduced order models (SROMs). Given statistical information about an observed state variable in a system, unknown parameters are estimated probabilistically through the solution of a model-constrained, stochastic optimization problem. The point of departure and crux of the proposed framework is the representation of a random quantity using a SROM - a low dimensional, discrete approximation to a continuous random element that permits efficient and non-intrusive stochastic computations. Characterizing the uncertainties with SROMs transforms the stochastic optimization problem into a deterministic one in a larger dimensional space. The non-intrusive nature of SROMs facilitates efficient gradient computation for random vector unknowns using an adjoint method approach and relies entirely on calls to existing deterministic simulators. Furthermore, the method is naturally extended to handle multiple sources of uncertainty in cases where state variable data, system parameters, and boundary conditions are all considered random.

The new and widely-applicable SROM framework is formulated for a gen-

eral stochastic optimization problem in terms of an abstract objective function and constraining model. For demonstration purposes, however, we study its performance in the specific case of inverse identification of random material parameters in elastodynamics. We demonstrate the ability to efficiently recover random shear moduli given material displacement statistics as input data. We also show that the approach remains effective for the case where the loading in the problem is random as well.

3.1 Introduction

Inverse problems arise in a range of important engineering applications including elasticity imaging, source identification, and damage detection. Generally speaking, one is provided data regarding the observed or measured state of a system and then uses this information to estimate some unknown parameters of interest. The standard approach is to then pose the inverse problem as an optimization problem where the solution is obtained by minimizing a relevant objective function involving the state data. Since the state and parameters of the system are connected through a governing boundary value problem, it appears as a constraint on the optimization problem.

Inherent in any system under consideration is uncertainty in the model definition (boundary conditions, geometry, material properties, etc.) that govern it. Additionally, in the common situation where the inverse problem depends on experimentally measured quantities, instrument errors and noise further impact the variance in potential solutions. While explicitly incorporating these uncertainties in the solution framework provides robustness to fluctuations in input

data and rigorous quantification of solution uncertainty, it generally comes at the expense of complex implementations and substantial computational cost. This work focusses on a practical and efficient approach to solving inverse problems under uncertainty.

Existing methods to treat inverse problems with uncertainty can be broadly classified into two categories: the Bayesian inference approach and the newer stochastic optimization approach. In the former, the posterior probability distribution of the unknown/design parameters given a realization of the state variable is first formulated using Bayes' theorem. This conditional distribution combines the information from the input data through the likelihood function with any *a priori* knowledge of the unknowns using a user-specified prior distribution. The posterior distribution is then sampled using Markov Chain Monte Carlo (MCMC) algorithms in order to estimate the statistics of the unknown parameters. While this approach has achieved success in a number of applications [15, 22, 17, 16] , common criticisms of the approach include its computational cost (since every MCMC sample generally requires a deterministic simulation) and the sensitivity of the resulting solutions to the prior distribution model chosen.

This paper considers the latter approach of stochastic optimization. Here, the point of departure from Bayesian inference is immediate - the input data for the inverse problem is the statistics of the system state rather than a single deterministic realization. An objective function is formulated in terms of the given state variable statistics and then the unknown parameters are estimated probabilistically as the random variables that minimize this objective function. The random state and parameters of the system in consideration are related

through a governing stochastic model, which therefore constrains the optimization problem. For tractability, this stochastic optimization problem is generally translated into a deterministic one through a suitable parameterization of the random quantities. From here, conventional deterministic optimization algorithms can be applied to estimate the unknown parameters of the probabilistic models used.

The stochastic optimization approach was first proposed in [19], where the framework was applied to solve the stochastic inverse heat conduction problem. Here, an unknown, random heat flux was estimated given the probability distribution function (PDF) of the temperature at discrete points in a conducting solid. The system uncertainties were represented using generalized polynomial chaos expansions (GPCE) [24, 26] and a conjugate gradient approach was used to solve the optimization problem constrained by the forward stochastic heat conduction problem. The spectral stochastic finite element method (SSFEM) [4] was employed to solve all subproblems during the optimization algorithm (evaluating the forward problem, calculating gradients), requiring extensive modification of the existing deterministic solver and limiting the overall scalability of the approach.

To overcome these shortcomings associated with reliance on the SSFEM, the work was later extended in [3] by representing uncertainty with a sparse grid collocation approach for the stochastic inverse heat conduction problem. The non-intrusive nature of stochastic collocation [1, 25] yielded a decoupled framework for stochastic optimization that can be readily parallelized (and is hence scalable) and relies solely on calls to deterministic simulators and optimization software. Furthermore, the approach was able to incorporate the effects of mul-

tiple sources of uncertainty where the temperature data, material conductivity, and unknown heat flux were all considered random. The framework was shown to effectively recover an unknown boundary heat flux in an inverse or design problem given either the moments or PDF of the temperature at points in the domain. While scalable, the approach still suffered from the curse of dimensionality and thus required a very large number of deterministic simulations. An adaptive sparse-grid approach was later proposed in [14] in an effort to use as few collocation points and hence model evaluations as possible for stochastic optimization problems. The approach was combined with a trust-region algorithm to efficiently solve PDE-constrained optimization under uncertainty. However, only the data in the PDEs was considered random in this case while the optimization variables were assumed to be deterministic.

The point of departure from existing work and the crux of the method proposed here is the representation of a random quantity using a stochastic reduced order model (SROM). A SROM is a low-dimensional, discrete approximation to a continuous random element comprised of a finite and generally small number of samples with varying probability. Such a representation allows for non-intrusive and efficient stochastic computations in terms of only this small set of defining samples and probabilities. The SROM concept was originally proposed in [6] and then further refined in [23]. The application of SROMs has thus far exclusively focussed on propagating uncertainty in forward models, including the determination of effective conductivities for random microstructures [7], the estimation of linear dynamic system states [8, 9], and the quantification of uncertainty in intergranular corrosion rates [21]. The primary strengths of SROMs, as shown in these papers, are their ability to represent an underlying random quantity with low-dimensionality and to subsequently solve uncertainty prop-

agation problems in a fraction of the computational time required by traditional Monte Carlo simulation.

This work represents the first application of SROMs for uncertainty quantification in inverse problems by introducing a novel approach for stochastic optimization with model constraints based on this concept. The framework represents a practical alternative to Bayesian inference and previous stochastic optimization approaches with the following strengths: 1) it relies entirely on calls to existing deterministic solvers and standard optimization software, 2) it is easily parallelized and scalable, and 3) it is readily extended to handle multiple sources of uncertainty. Additionally, in contrast with existing stochastic collocation-based methods that discretize the entire probability space equally, SROMs naturally give higher weight to important areas of the probability space. This property yields low-dimensional approximations and thus relatively few calls to the deterministic model to solve the stochastic optimization problem.

The SROM-based inverse problem approach presented here is formulated for a general stochastic optimization problem in terms an abstract objective function and model constraint. The transformation of the constrained optimization problem from stochastic to deterministic using SROMs is developed in these abstract terms and followed by a general derivation of gradients using an adjoint approach. In order to study the performance of the method, we then show the adaptation of the formulation to the specific case of inverse identification of random material parameters in elastodynamics. We demonstrate the ability to efficiently recover random shear moduli given material displacement statistics as input data. We also show that the approach remains effective for the case where the loading in the problem can only be characterized probabilis-

tically.

The article is organized as follows: Next, in Section 2, we provide the necessary background for this study, introducing SROMs and describing their traditional use for propagating uncertainty in deterministic models. Then, Section 3 describes the proposed SROM-based inverse problem approach, providing both the formulation for general stochastic optimization problems and the subsequent application of the method for inverse material identification in elastodynamics. Section 4 presents three numerical examples, demonstrating the effectiveness of the proposed method for cases of multiple sources of uncertainty, limited/sparse input data, and problems with multiple unknown, random parameters. We finally conclude in Section 5 with a summary of this work.

3.2 Background

3.2.1 Stochastic reduced order models (SROMs) for uncertainty propagation in forward problems

Stochastic reduced order models (SROMs) provide a low-dimensional, discrete approximation of a given random quantity and have been used in several past works [7, 8, 21] to facilitate efficient stochastic computations. Namely, traditional SROM applications have involved estimating the state $\mathbf{S} \in \mathcal{S} \subset \mathbb{R}^n$ of a system, provided the probabilistic description of some random parameters $\mathbf{X} \in \mathcal{X} \subset \mathbb{R}^d$ and a system model $\mathcal{M}$ that connects the two

$$\mathcal{M}(\mathbf{S}, \mathbf{X}) = 0 \tag{3.1}$$

We note that models depending on random fields can be described by this model after an appropriate parameterization or discretization. One of the strengths of using SROMs is the ability to propagate uncertainty in these types of problems in a non-intrusive fashion, meaning the mathematical model $\mathcal{M}$ need only be accessed as a "black-box". Therefore, the developments in this section and the optimization framework detailed subsequently are not limited to any particular system and we can proceed in terms of an arbitrary model $\mathcal{M}$ with parameters (inputs) $\mathbf{X}$ and state (output) $\mathbf{S}$.

Performing stochastic computations of the general form (3.1) using SROMs requires the construction of an accurate probability model of $\mathbf{X}$ and then a method to propagate uncertainty to estimate the statistics $\mathbf{S}$. This section briefly describes these procedures after first introducing and defining the SROM.

SROM definition

For the following discussion, let $(\Omega, \mathcal{F}, P)$ and $(\Psi, \mathcal{G})$ denote a probability space and a measurable space, respectively. Here, Ω is the sample space, $\mathcal{F} \subseteq 2^{\Omega}$ is the $\sigma-$algebra (event space), and $P : \mathcal{F} \to [0, 1]$ is the probability measure. A function $X : \Omega \mapsto \Psi$ is a random element if it is measurable from $(\Omega, \mathcal{F})$ to $(\Psi, \mathcal{G})$, that is, if $X^{-1}(G) = \{\omega : X(\omega) \in \mathcal{G}\} \in \mathcal{F}, \quad \forall G \in \mathcal{G}$ [5]. In our discussion, we assume $\Psi = \mathbb{R}^d$ and $\mathcal{G} = \mathcal{B}(\mathbb{R}^d)$ is the Borel σ-algebra on $\mathbb{R}^d$, and so $\mathbf{X} : \Omega \mapsto \mathbb{R}^d$ is a d-dimensional random vector.

A stochastic reduced order model (SROM) $\tilde{\mathbf{X}}$ is a simple random element with a finite set of samples $\{\tilde{\mathbf{x}}^{(1)}, ..., \tilde{\mathbf{x}}^{(m)}\}$ and corresponding probabilities $(p^{(1)}, ..., p^{(m)})$ such that $p^{(k)} \geq 0 \ \forall k$ and $\sum_{k=1}^{m} p^{(k)} = 1$ [7], that is close to $\mathbf{X}$ in

some sense. Hence, the SROM $\tilde{\mathbf{X}}$ is completely defined by the model size m and sample-probability pairs $\{\tilde{\mathbf{x}}^{(k)}, p^{(k)}\}_{k=1}^{m}$ and effectively provides a discrete-valued approximation to a given continuous random quantity $\mathbf{X}$.

When SROMs are used for uncertainty propagation in forward models, it is assumed that the statistics of $\mathbf{X}$ are known a priori. For example, one is provided with the following expressions for its marginal distributions, moments of order q, and correlation matrix

$$F_i(x_i) = P(X_i \leq x_i) \tag{3.2}$$

$$\mu_i(q) = E[X_i^q] \tag{3.3}$$

$$\mathbf{r} = E[\mathbf{X}\mathbf{X}^T], \tag{3.4}$$

Then, once the SROM parameters ($\{\tilde{\mathbf{x}}\}$ and $\mathbf{p}$) are specified, the corresponding expressions for its statistics are given by

$$\tilde{F}_i(x_i) = \sum_{k=1}^{m} p^{(k)} \mathbf{1}\left(\tilde{x}_i^{(k)} \leq x_i\right) \tag{3.5}$$

$$\tilde{\mu}_i(q) = \sum_{k=1}^{m} p^{(k)} (\tilde{x}_i^{(k)})^q, \tag{3.6}$$

$$\tilde{r}(i,j) = \sum_{k=1}^{m} p^{(k)} \tilde{x}_i^{(k)} \tilde{x}_j^{(k)} \tag{3.7}$$

where $\mathbf{1}(\cdot)$ is the indicator function. Note that by design, the SROM is constructed such that $\tilde{\mathbf{X}}$ provides a satisfactory discrete approximation to $\mathbf{X}$, and so Equations (3.5)-(3.7) provide estimates of the true statistics in (3.2)-(3.4). The details of this construction is provided in the following section.

SROM construction for forward problems

In order to solve stochastic problems of the general form (3.1), which we will refer to as the "forward problem", we first describe how to construct a SROM

of $\mathbf{X}$ given knowledge of its statistics. An optimal reduced order representation of a random input can be obtained by selecting the SROM parameters such that the statistics of $\tilde{\mathbf{X}}$ ((3.5)-(3.7)) best approximate those of $\mathbf{X}$ ((3.2)-(3.4)). In practice, this is done by solving an optimization problem with objective function measuring the discrepancies between SROM and target marginal distributions, marginal moments up to order $\bar{q} \geq 1$, and correlation matrices as

$$e_1(\{\tilde{\mathbf{x}}\}, \mathbf{p}) = \frac{1}{2} \sum_{i=1}^{d} \int_{I_i} \left(\tilde{F}_i(x_i) - F_i(x_i) \right)^2 dx_i \tag{3.8}$$

$$e_2(\{\tilde{\mathbf{x}}\}, \mathbf{p}) = \frac{1}{2} \sum_{i=1}^{d} \sum_{q=1}^{\bar{q}} \left(\frac{\tilde{\mu}_i(q) - \mu_i(q)}{\mu_i(q)} \right)^2 \tag{3.9}$$

$$e_3(\{\tilde{\mathbf{x}}\}, \mathbf{p}) = \frac{1}{2} \sum_{i,j=1; j>i}^{d} \left(\frac{\tilde{r}(i,j) - r(i,j)}{r(i,j)} \right)^2, \tag{3.10}$$

respectively, where I_i denotes the support of F_i. The optimization problem for selecting the defining SROM parameters is then formally stated as

$$\begin{aligned} \tilde{\mathbf{X}} \equiv & \underset{\{\tilde{\mathbf{x}}\}, \mathbf{p}}{\operatorname{argmin}} \left(\sum_{i=1}^{3} \alpha_i e_i(\{\tilde{\mathbf{x}}\}, \mathbf{p}) \right) \\ \text{s.t. } & \sum_{k=1}^{m} p^{(k)} = 1 \text{ and } p^{(k)} \geq 0, \ k = 1, ..., m, \end{aligned} \tag{3.11}$$

where $\{\alpha_i \geq 0\}_{i=1}^{3}$ are weighting factors controlling the relative contribution of each error term to the cost functional. Note that the model size m is not included in the optimization and is selected beforehand based on computational considerations. Furthermore, it was shown in [6] that the statistics of the SROM $\tilde{\mathbf{X}}$ converge to those of the target random variable $\mathbf{X}$ with increasing model size, i.e. $e_i \to 0 \ \forall i$ as $m \to \infty$. Details on the solution of (3.23) can be found in [23] and are omitted here for brevity.

Propagating uncertainty with SROMs

After a SROM is generated for the random parameters $\mathbf{X}$ of a system, the uncertainty in the state $\mathbf{S}$ can be estimated non-intrusively in a manner analogous to Monte Carlo methods. This is done by simply evaluating the model $\mathcal{M}$ with $\mathbf{X} = \tilde{\mathbf{x}}^{(k)}$ as

$$\mathcal{M}(\tilde{\mathbf{s}}^{(k)}, \tilde{\mathbf{x}}^{(k)}) = 0, \ k = 1, ..., m \tag{3.12}$$

The resulting state samples $\{\tilde{\mathbf{s}}\}$ along with the original input SROM probabilities $\mathbf{p}$ define a new SROM $\tilde{\mathbf{S}}$ of $\mathbf{S}$. Now, we can use $\tilde{\mathbf{S}}$ to estimate the statistics of the state using expressions analagous to (3.5)-(3.7). For example, the marginal distributions and moments of $\mathbf{S}$ can be approximated as

$$P(S_i \leq s_i) \approx P(\tilde{S}_i \leq s_i) = \sum_{k=1}^{m} p^{(k)} \mathbf{1}\left(\tilde{s}_i^{(k)} \leq s_i\right) \tag{3.13}$$

$$E[S_i^q] \approx E[\tilde{S}_i^q] = \sum_{k=1}^{m} p^{(k)} (\tilde{s}_i^{(k)})^q \tag{3.14}$$

Viewing the above procedure for propagating uncertainty with SROMs, it is evident that the method shares the same benefits of Monte Carlo simulation in its generality and non-intrusiveness. However, the SROMs are designed to better represent the underlying random quantity through the optimization problem in Equation (3.23) and therefore generally require far fewer samples and model evaluations to obtain a solution. Indeed, SROMs have been shown in numerous previous studies to significantly reduce computational cost over Monte Carlo simulation while maintaining a similar degree of accuracy for applications from corrosion modeling [21] to structural dynamics [23].

Multiple sources of uncertainty with SROMs

An additional strength of the SROM approach to stochastic computations detailed in this section is that it can be naturally extended to handle problems with multiple sources of uncertainty. Consider the case where, in addition to the parameters $\mathbf{X}$, the state of a system $\mathbf{S}$ also depends on a separate and independent source of randomness in some variable $\mathbf{\Theta}$. This could occur, for example, when the variability in the state of a system is influenced by both internal randomness (material properties, geometry, etc) as well as uncertainty from external sources (boundary conditions, loads, fluxes, etc.). In this case, the abstract system model in Equation (3.1) takes the form

$$\mathcal{M}(\mathbf{S}, \mathbf{X}; \mathbf{\Theta}) \tag{3.15}$$

Note here that we could very well encapsulate all random parameters as $\mathbf{Y} = [\mathbf{X}\ \mathbf{\Theta}]^T$. However, this explicit separation will be helpful in the inverse problem setting where $\mathbf{X}$ is considered unknown while $\mathbf{\Theta}$ is given.

The procedure for solving Equation (3.15) using SROMs is consistent with the approach described previously with the caveat of treating the additional random parameters $\mathbf{\Theta}$. The SROMs $\tilde{\mathbf{X}} = \{\tilde{\mathbf{x}}^{(i)}, p_x^{(i)}\}_{i=1}^{m_x}$ and $\tilde{\mathbf{\Theta}} = \{\tilde{\theta}^{(j)}, p_\theta^{(j)}\}_{j=1}^{m_\theta}$ must be formed in this case for both $\mathbf{X}$ and $\mathbf{\Theta}$ by solving the optimization problem in Equation (3.23) given the probabilistic description of each variable. In this case, the SROM approximation $\tilde{\mathbf{S}}$ to the system state $\mathbf{S}$ is generated by evaluating the model $m_x \times m_\theta$ times as

$$\mathcal{M}(\tilde{\mathbf{s}}^{(k)}, \tilde{\mathbf{x}}^{(i)}; \tilde{\boldsymbol{\theta}}^{(j)}) = 0, \text{ for } i = 1, ..., m_x,\ j = 1, ..., m_\theta \tag{3.16}$$

$$k = (j-1) \times m_x + i \tag{3.17}$$

Here, the probabilities associated with the SROM $\tilde{\mathbf{S}}$ are given by

$$p_s^{(k)} = p_x^{(i)} \times p_\theta^{(j)} \tag{3.18}$$

Using the SROM defined by these samples and probabilities, the statistics of $\mathbf{S}$ can again be approximated using the expressions in (3.13) and (3.14). This concept generalizes in the same manner to more than two random inputs, with the computational cost increasing with the size of each additional SROM.

3.3 Stochastic inverse problem approach

In this section, we introduce a novel framework for solving inverse problems under uncertainty using SROMs. The non-intrusive nature of SROMs allows us to formulate the approach in terms of a general stochastic optimization problem governed by an abstract model of the form in Equation (3.1). This constrained optimization problem is first defined and then transformed into its deterministic counterpart by choosing an SROM approximation to the uncertainties. We then provide details on the solution of the SROM-based optimization problem, supplying the necessary ingredients to facilitate the use of standard gradient-based optimization software. Finally, we comment on the extension of the method to the case of optimization and inverse problems in the presence of multiple uncertainties.

3.3.1 The general stochastic optimization problem

In this work, our strategy for solving inverse problems under uncertainty is to first pose them as model-constrained stochastic optimization problems. Here,

we seek to determine the parameters $\mathbf{X}$ in a system governed by the model $\mathcal{M}$ such that $\mathbf{X}$ and the resulting state $\mathbf{S}$ minimize some function of these variables. Contrast this with the problem of uncertainty propagation in forward models, as described in the previous section using SROMs, where the situation is reversed (we are given $\mathbf{X}$ and use $\mathcal{M}$ to compute $\mathbf{S}$ directly). We will denote the general objective function to be minimized as $\mathcal{J}(\mathbf{S}, \mathbf{X})$ where $\mathcal{J} : \mathbb{R}^n \times \mathbb{R}^d \to \mathbb{R}$. We choose a "Discretize-Optimize" approach [10, 11], where we will work with a discretized version of the model equations (3.1) and hence Euclidean spaces in the derivations to follow. In this manner, let $\mathbf{M}(\mathbf{S}, \mathbf{X}) = \mathbf{0} \in \mathbb{R}^n$ denote the resulting stochastic algebraic system of equations.

With this notation adopted, we can pose the general form of the constrained stochastic optimization problem as follows

$$\begin{aligned} &\underset{\mathbf{S},\mathbf{X}}{\operatorname{argmin}} \;\; \mathcal{J}(\mathbf{S}, \mathbf{X}) \\ &\text{such that: } \; \mathbf{M}(\mathbf{S}, \mathbf{X}) = \mathbf{0} \end{aligned} \tag{3.19}$$

In the study of inverse problems, the objective function $\mathcal{J}$ generally represents an error metric measuring how close a particular value of $\mathbf{X}$ is to producing a state $\mathbf{S}$ whose statistics matches those of given measurement data. Note, however, that the general form in (3.19) could also represent an optimal control or design problem depending on the nature of $\mathcal{J}$. Likewise, the context of any of these problems can span a wide range of systems as no specific form has been assumed for the model $\mathbf{M}$.

3.3.2 The SROM approach to stochastic optimization

At this point, we depart from existing approaches that have adopted spectral representations of $\mathbf{X}$ and $\mathbf{S}$ and proceed in terms of the SROM approximations, $\tilde{\mathbf{X}}$ and $\tilde{\mathbf{S}}$, of these quantities instead. In accordance with the previous section, all uncertainty in problem (3.19) can now be expressed in terms of m parameter samples $\{\tilde{\mathbf{x}}\}$, the resulting state samples $\{\tilde{\mathbf{s}}\}$, and the vector of probabilities $\mathbf{p} \in \mathbb{R}^m$ corresponding to each sample pair. For notational convenience, we will interpret the SROM samples as the concatenated vectors

$$\{\tilde{\mathbf{x}}\} \equiv \begin{Bmatrix} \tilde{\mathbf{x}}^{(1)} \\ \vdots \\ \tilde{\mathbf{x}}^{(m)} \end{Bmatrix} \in \mathbb{R}^D; \quad \{\tilde{\mathbf{s}}\} \equiv \begin{Bmatrix} \tilde{\mathbf{s}}^{(1)} \\ \vdots \\ \tilde{\mathbf{s}}^{(m)} \end{Bmatrix} \in \mathbb{R}^N, \tag{3.20}$$

where $D = d \times m$ and $N = n \times m$.

By introducing the SROM approximations of the random state and parameter vectors, we can now effectively transform the constrained stochastic optimization problem in (3.19) into a deterministic one. First, the objective function can be expressed in terms of the SROMs as

$$\mathcal{J}(\mathbf{S}, \mathbf{X}) \approx \mathcal{J}(\tilde{\mathbf{S}}, \tilde{\mathbf{X}}) = \mathcal{J}\left(\{\tilde{\mathbf{s}}\}, \{\tilde{\mathbf{x}}\}, \mathbf{p}\right) \tag{3.21}$$

where the optimization problem is now over a finite number of deterministic unknown parameters. Likewise, the model constraints using the SROM approximation are given by

$$\tilde{\mathbf{M}} \equiv \mathbf{M}(\tilde{\mathbf{S}}, \tilde{\mathbf{X}}) = \begin{Bmatrix} \mathbf{M}(\tilde{\mathbf{s}}^{(1)}, \tilde{\mathbf{x}}^{(1)}) \\ \vdots \\ \mathbf{M}(\tilde{\mathbf{s}}^{(m)}, \tilde{\mathbf{x}}^{(m)}) \end{Bmatrix} = \mathbf{0} \ \in \mathbb{R}^N \tag{3.22}$$

where we have converted the governing stochastic constraint into m sets of decoupled, deterministic constraint equations. We note that it was proved in [7] that the SROM solution to stochastic algebraic equations (3.22) converges to the true solution with increasing SROM size.

Finally, we can pose the optimization problem in the space of the defining parameters of the unknown SROM $\tilde{\mathbf{X}}$ only by working with a reduced formulation where $\tilde{\mathbf{S}}$ is viewed as an implicit function of $\tilde{\mathbf{X}}$ through Equation (3.1). In this case, we assume that the state and parameter samples belong to appropriate admissible sets, $\{\tilde{\mathbf{s}}\} \in \mathcal{S}$ and $\{\tilde{\mathbf{x}}\} \in \mathcal{X}$, and that $\mathbf{M}$ is continuously differentiable over these sets. Then, through the implicit function theorem, we adopt the objective function $\hat{\mathcal{J}}(\tilde{\mathbf{X}}) = \mathcal{J}(\tilde{\mathbf{S}}(\tilde{\mathbf{X}}), \tilde{\mathbf{X}})$ and formally define the SROM solution to the stochastic optimization problem (3.19) as

$$\tilde{\mathbf{X}}^* \equiv \underset{\{\tilde{\mathbf{x}}\}\in\mathcal{X},\, \mathbf{p}\in\mathcal{P}}{\operatorname{argmin}} \quad \hat{\mathcal{J}}(\{\tilde{\mathbf{x}}\}, \mathbf{p}) \tag{3.23}$$

where $\mathcal{P}$ is the feasible set of SROM probabilities

$$\mathcal{P} = \left\{ \mathbf{p} |\ \mathbf{p} \in \mathbb{R}^m,\ \ \sum_{i=1}^{m} p^{(i)} = 1 \text{ and } p^{(i)} \geq 0,\ \forall i \right\} \tag{3.24}$$

and the set $\mathcal{X}$ could, for example, reflect specified inequality constraints on $\{\tilde{\mathbf{x}}\}$

$$\mathcal{X} = \left\{ \{\tilde{\mathbf{x}}\} |\ \{\tilde{\mathbf{x}}\} \in \mathbb{R}^D,\ \ \{\tilde{\mathbf{x}}\}_{\text{min}} \leq \{\tilde{\mathbf{x}}\} \leq \{\tilde{\mathbf{x}}\}_{\text{max}} \right\} \tag{3.25}$$

In the remaining formulation, however, we shall focus on the non-trivial model constraints (3.22) and forego the treatment of the more straightforward equality and inequality constraints on $p^{(i)}$ and $\{\tilde{\mathbf{x}}\}$ for the sake of simplicity.

3.3.3 Solution strategy for the SROM-based optimization problem

We now focus on the details of the solution to the deterministic SROM-based optimization problem defined in (3.23). We will assume that we are employing an external gradient-based optimization package that requires only the computation of the objective function $\hat{\mathcal{J}}$ and its gradient $\nabla\hat{\mathcal{J}}$ (e.g. quasi-Newton methods). Along these lines, we now provide an efficient approach for computing the gradient using an adjoint approach and then summarize the full procedure for implementing the SROM optimization framework.

Gradient derivations

Here, we illustrate a Lagrangian-based approach [12] to deriving gradients of the objective function $\hat{\mathcal{J}}$ with respect to the unknown SROM parameters $\{\tilde{\mathbf{x}}\}$ and $\mathbf{p}$. For this purpose, we assume $\hat{\mathcal{J}}$ to be differentiable with respect to both $\{\tilde{\mathbf{x}}\}$ and $\mathbf{p}$. We focus primarily on obtaining an expression for $\frac{\partial\hat{\mathcal{J}}}{\partial\{\tilde{\mathbf{x}}\}}$, which is significantly more involved due to the dependence of the model $\mathbf{M}$ on $\{\tilde{\mathbf{x}}\}$ (Eq. (3.22)). We begin by first introducing the Lagrangian function

$$\mathcal{L}(\{\tilde{\mathbf{x}}\},\mathbf{p},\{\tilde{\mathbf{w}}\}) = \hat{\mathcal{J}}(\{\tilde{\mathbf{x}}\},\mathbf{p}) + \{\tilde{\mathbf{w}}\}^T\tilde{\mathbf{M}} \tag{3.26}$$

where $\{\tilde{\mathbf{w}}\} \in \mathbb{R}^N$ is the set of adjoint variables. Note that if we consider state samples $\{\tilde{\mathbf{s}}\}$ that are generated via Equation (3.22), we have $\mathcal{L}(\{\tilde{\mathbf{x}}\},\mathbf{p},\{\tilde{\mathbf{w}}\}) = \hat{\mathcal{J}}(\{\tilde{\mathbf{x}}\},\mathbf{p})$ since $\tilde{\mathbf{M}} = \mathbf{0}$ is satisfied. Therefore, for the gradients of the objective function with respect to the unknown SROM parameter samples, we have

$$\hat{\mathcal{J}}_{\{\tilde{\mathbf{x}}\}} = \mathcal{L}_{\{\tilde{\mathbf{x}}\}} \tag{3.27}$$

where we have adopted the shorthand notation $\hat{\mathcal{J}}_{\{\tilde{\mathbf{x}}\}} \equiv \frac{\partial \hat{\mathcal{J}}}{\partial \{\tilde{\mathbf{x}}\}}$ for derivatives.

Using Equation (3.26) and the fact that the samples $\{\tilde{\mathbf{s}}\}$ are viewed as implicit functions of $\{\tilde{\mathbf{x}}\}$, we have

$$\begin{aligned}\mathcal{L}_{\{\tilde{\mathbf{x}}\}} &= [\{\tilde{\mathbf{s}}\}_{\{\tilde{\mathbf{x}}\}}]^T \mathcal{J}_{\{\tilde{\mathbf{s}}\}} + \mathcal{J}_{\{\tilde{\mathbf{x}}\}} + [\{\tilde{\mathbf{s}}\}_{\{\tilde{\mathbf{x}}\}}]^T [\tilde{\mathbf{M}}_{\{\tilde{\mathbf{s}}\}}]^T \{\tilde{\mathbf{w}}\} + [\tilde{\mathbf{M}}_{\{\tilde{\mathbf{x}}\}}]^T \{\tilde{\mathbf{w}}\} \\ &= \mathcal{J}_{\{\tilde{\mathbf{x}}\}} + [\tilde{\mathbf{M}}_{\{\tilde{\mathbf{x}}\}}]^T \{\tilde{\mathbf{w}}\} + [\{\tilde{\mathbf{s}}\}_{\{\tilde{\mathbf{x}}\}}]^T \left([\tilde{\mathbf{M}}_{\{\tilde{\mathbf{s}}\}}]^T \{\tilde{\mathbf{w}}\} + \mathcal{J}_{\{\tilde{\mathbf{s}}\}} \right) \end{aligned} \tag{3.28}$$

We can then eliminate the third term by choosing the adjoint variables such that they satisfy

$$[\tilde{\mathbf{M}}_{\{\tilde{\mathbf{s}}\}}]^T \{\tilde{\mathbf{w}}\} = -\mathcal{J}_{\{\tilde{\mathbf{s}}\}} \tag{3.29}$$

where $[\tilde{\mathbf{M}}_{\{\tilde{\mathbf{s}}\}}]$ is the Jacobian of the discretized state equations. Here, we can leverage the non-intrusive nature of the SROM approximation to greatly simplify the solution of (3.29). Adopting the shorthand notation $\tilde{\mathbf{M}}^{(i)} \equiv \mathbf{M}(\tilde{\mathbf{s}}^{(i)}, \tilde{\mathbf{x}}^{(i)})$, we note that

$$[\tilde{\mathbf{M}}^{(i)}_{\tilde{\mathbf{s}}^{(j)}}] = [\mathbf{0}], \text{ for } i \neq j, \tag{3.30}$$

and so the problem decouples into m independent systems of equations as

$$[\tilde{\mathbf{M}}^{(k)}_{\tilde{\mathbf{s}}^{(k)}}]^T \tilde{\mathbf{w}}^{(k)} = -\mathcal{J}_{\tilde{\mathbf{s}}^{(k)}}, \text{ for } k = 1, ...m \tag{3.31}$$

Finally, using this set of adjoint variables, we can express the gradient in (3.27) as

$$\hat{\mathcal{J}}_{\{\tilde{\mathbf{x}}\}} = \begin{Bmatrix} \hat{\mathcal{J}}_{\tilde{\mathbf{x}}^{(1)}} \\ \vdots \\ \hat{\mathcal{J}}_{\tilde{\mathbf{x}}^{(m)}} \end{Bmatrix} = \begin{Bmatrix} \mathcal{J}_{\tilde{\mathbf{x}}^{(1)}} + [\tilde{\mathbf{M}}^{(1)}_{\tilde{\mathbf{x}}^{(1)}}]^T \tilde{\mathbf{w}}^{(1)} \\ \vdots \\ \mathcal{J}_{\tilde{\mathbf{x}}^{(m)}} + [\tilde{\mathbf{M}}^{(m)}_{\tilde{\mathbf{x}}^{(m)}}]^T \tilde{\mathbf{w}}^{(m)} \end{Bmatrix} \tag{3.32}$$

where we have again decoupled the expression using the fact that

$$[\tilde{\mathbf{M}}^{(i)}_{\tilde{\mathbf{x}}^{(j)}}] = [\mathbf{0}], \text{ for } i \neq j \tag{3.33}$$

With regard to the gradient with respect to the SROM probabilities $\hat{\mathcal{J}}_{\mathbf{p}}$, since these parameters do not appear in the model constraints explicitly, we have

$$\hat{\mathcal{J}}_{\mathbf{p}} = \mathcal{L}_{\mathbf{p}} = \mathcal{J}_{\mathbf{p}} \tag{3.34}$$

Note that in general this expression will be easily obtained due to the simple linear relations of the SROM statistics (3.5) - (3.7) with respect to $\mathbf{p}$.

Implementation summary

Here, we briefly summarize the procedure for computing the objective function and gradient for the optimization problem defined in Equation (3.23), so that it can be readily solved using gradient-based optimization software. Given a set of SROM parameters $\{\tilde{\mathbf{x}}\}$ and $\mathbf{p}$, the following steps are to be carried out to supply $\hat{\mathcal{J}}$ and $\nabla\hat{\mathcal{J}}$ to the optimization algorithm used:

1. Solve m decoupled, forward problems (Equation (3.22)) for the state samples $\{\tilde{\mathbf{s}}\}$.
2. Solve m decoupled, adjoint problems (Equation (3.31)) for the adjoint variables $\{\tilde{\mathbf{w}}\}$.
3. Evaluate the objective function $\hat{\mathcal{J}}(\{\tilde{\mathbf{x}}\}, \mathbf{p})$.
4. Evaluate the gradients $\hat{\mathcal{J}}_{\{\tilde{\mathbf{x}}\}}$ and $\hat{\mathcal{J}}_{\mathbf{p}}$ using Equations (3.32) and (3.34), respectively.

It is clear from this procedure that computing the objective function and gradient at each iteration requires $2m$ deterministic model solves. However, it should be emphasized that since the solves are decoupled, they can be easily

parallelized to improve scalability. Furthermore, this number of deterministic solves remains constant regardless of the dimension d of the random unknown parameters $\mathbf{X}$. A detailed discussion of optimization algorithms can be found in [20] and is outside the scope of this study. We also note that the Hessian (or the operation of a Hessian on a vector) could be derived along similar lines to the above approach in order to utilize second order optimization algorithms

3.3.4 Optimization under multiple uncertainties

In this section, we briefly describe the generalization of the proposed SROM framework for stochastic optimization problems with multiple sources of uncertainty. Similar to Section 3.2.1, we consider an additional and independent (known) source of uncertainty in the parameters $\mathbf{\Theta}$, so that the governing model takes the form (3.15). We assume that the SROM $\tilde{\mathbf{\Theta}} = \{\tilde{\theta}^{(j)}, p_\theta^{(j)}\}_{j=1}^{m_\theta}$ has been formed offline to represent $\mathbf{\Theta}$ prior to the solution of the stochastic optimization problem.

As was the case for propagating uncertainty in forward models with multiple sources of randomness, the SROM approach to stochastic optimization is similarly straightforward. The introduction of the random parameters $\mathbf{\Theta}$ does not directly affect the objective function (3.21), but it does result in the following modified form of the discretized constraint equations

$$\mathbf{M}(\mathbf{S}, \mathbf{X}; \mathbf{\Theta}) = \mathbf{0} \tag{3.35}$$

Using the SROM approximations $\tilde{\mathbf{X}}$ and $\tilde{\mathbf{\Theta}}$ and the approach to propagating uncertainties given in Equation (3.16), the associated set of deterministic constraint

equations is now given by

$$\mathbf{M}(\tilde{\mathbf{S}}, \tilde{\mathbf{X}}; \tilde{\mathbf{\Theta}}) = \mathbf{M}(\{\tilde{\mathbf{s}}\}, \{\tilde{\mathbf{x}}\}; \{\tilde{\boldsymbol{\theta}}\}) = \left\{ \begin{array}{c} \mathbf{M}(\tilde{\mathbf{s}}^{(1)}, \tilde{\mathbf{x}}^{(1)}; \tilde{\boldsymbol{\theta}}^{(1)}) \\ \vdots \\ \mathbf{M}(\tilde{\mathbf{s}}^{(k)}, \tilde{\mathbf{x}}^{(i)}; \tilde{\boldsymbol{\theta}}^{(j)}) \\ \vdots \\ \mathbf{M}(\tilde{\mathbf{s}}^{(m_s)}, \tilde{\mathbf{x}}^{(m_x)}; \tilde{\boldsymbol{\theta}}^{(m_\theta)}) \end{array} \right\} = \mathbf{0} \ \in \mathbb{R}^{\hat{N}} \quad (3.36)$$

Here, $\hat{N} = n \times m_x \times m_\theta$ and we have assumed the indexing scheme from Equation (3.17). It follows that one of the main changes to the optimization formulation is the need to solve the $m_x \times m_\theta$ forward problems in (3.36) to obtain the state samples $\{\tilde{\mathbf{s}}\} \in \mathbb{R}^{\hat{N}}$, as opposed to the m_x problems in (3.22).

Computing the gradient with respect to the SROM samples in Equation (3.27) for the case of multiple uncertainties still benefits from the decoupled nature of the SROM approach. To illustrate this, we adopt the shorthand notation for a given forward problem instance

$$\tilde{\mathbf{M}}^{(i,j)} = \mathbf{M}(\tilde{\mathbf{s}}^{(k)}, \tilde{\mathbf{x}}^{(i)}; \tilde{\boldsymbol{\theta}}^{(j)}) \quad (3.37)$$

where Equation (3.17) is again implied for the index k. Then, it is clear that the following simplifications (analogous to (3.30) and (3.33)) apply when taking derivatives with respect to the model equations

$$\tilde{\mathbf{M}}^{(i,j)}_{s^{(k)}} = [\mathbf{0}], \text{ for } k \neq (i-1) \times m_x + j \quad (3.38)$$

$$\tilde{\mathbf{M}}^{(i,j)}_{x^{(k)}} = [\mathbf{0}], \text{ for } k \neq j \quad (3.39)$$

The first expression implies a similar decoupling of the full adjoint problem in Equation (3.29) to a series of independent solutions of Equation (3.31). Note that in this case one must perform $m_x \times m_\theta$ solves for the adjoint variables $\{\tilde{\mathbf{w}}\} \in$

$\mathbb{R}^{\hat{N}}$. Finally, we must update each component of the gradient vector in (3.32) as follows

$$\hat{\mathcal{J}}_{\tilde{\mathbf{x}}^{(i)}} = \mathcal{J}_{\tilde{\mathbf{x}}^{(i)}} + \sum_{j=1}^{m_\theta} [\tilde{\mathbf{M}}_{\tilde{\mathbf{x}}^{(i)}}^{(i,j)}]^T \tilde{\mathbf{w}}^{(j)} \tag{3.40}$$

where (3.39) has been enforced to simplify the expression.

In summary, the SROM-based optimization framework can be straightforwardly extended to handle multiple sources of uncertainty. One must simply update the gradient expression according to (3.40) and cope with an increased computational cost in proportion to the size of the SROM used to model Θ. While in this case it requires $2(m_x \times m_\theta)$ model evaluations to compute the gradient at each optimization iteration, the solves remain decoupled from one another and hence easily parallelized.

3.4 Application

In this section, we introduce the problem of random material identification in elastodynamics and demonstrate the use of the SROM optimization approach in this setting. We begin by formulating the elastodynamics forward problem in both continuous and discrete forms and then describe the associated inverse problem of recovering random shear moduli given displacement statistics as input data. Finally, we illustrate how the general stochastic optimization framework using SROMs described in the previous section can be adapted to solve this stochastic inverse problem.

3.4.1 The forward elastodynamics problem

We now present the governing equations for the forward steady-state elastodynamics problem. We will assume small strains and deformations in a material governed by an isotropic elastic model. Furthermore, we shall neglect damping effects in the system and consider real-valued quantities only for simplicity. To begin, consider a linear elastic domain $\mathcal{D}$ undergoing time-harmonic motion described by the following stochastic PDE and boundary conditions

$$\nabla \cdot \boldsymbol{\Sigma} = -\rho\omega^2 \boldsymbol{\mathcal{U}} \qquad \text{in } \mathcal{D} \tag{3.41}$$

$$\boldsymbol{\mathcal{U}} = \mathbf{0} \qquad \text{on } \Gamma_u \tag{3.42}$$

$$\boldsymbol{\Sigma} \cdot \boldsymbol{n} = \boldsymbol{\tau} \qquad \text{on } \Gamma_t \tag{3.43}$$

where $\boldsymbol{\Sigma}$ is the stress tensor, ρ is the mass density, ω is the angular frequency, $\mathbf{U}$ is the displacement field, and $\boldsymbol{\tau}$ is an applied traction. Γ_u and Γ_t represent the portion of the boundary with a specified traction and displacement, respectively, and $\boldsymbol{n}$ is the outward normal along Γ_t. Additionally, we have the following relations for stress and strain $\boldsymbol{\mathcal{E}}$ in a linear, isotropic elastic material

$$\boldsymbol{\Sigma} = 2G\boldsymbol{\mathcal{E}}_d[\boldsymbol{\mathcal{U}}] + b\ \mathrm{tr}(\boldsymbol{\mathcal{E}}[\boldsymbol{\mathcal{U}}])\mathbf{I} \tag{3.44}$$

$$\boldsymbol{\mathcal{E}}[\boldsymbol{\mathcal{U}}] = \frac{1}{2}(\nabla \boldsymbol{\mathcal{U}} + \nabla \boldsymbol{\mathcal{U}}^T) \tag{3.45}$$

where G and b are the shear and bulk modulus, respectively, $\mathrm{tr}(\cdot)$ is the trace operator, $\mathbf{I}$ is the identity tensor, and $\boldsymbol{\mathcal{E}}_d \equiv \boldsymbol{\mathcal{E}} - \frac{1}{3}\mathrm{tr}(\boldsymbol{\mathcal{E}}[\boldsymbol{\mathcal{U}}])\mathbf{I}$ is the deviatoric part of the strain tensor.

For our study, the shear modulus is assumed to be the primary source of randomness in the system while the other stochastic variables (displacement, stress, strain) are considered random through their dependence on it. The remaining

material parameters (bulk modulus, density) will be taken to be deterministic and constant for simplicity. Furthermore, we consider a domain partitioned into d distinct regions $\{\mathcal{D}_i\}_{i=1}^{d}$, each with different shear moduli represented by the components of the vector $\mathbf{G} \in \mathbb{R}^d$. In the spirit of the general formulation in the previous section, the shear moduli represent the parameters of interest $\mathbf{X}$, while the displacements are the state variable $\mathbf{S}$ in the system. Hence, we can refer to the governing elastodynamics equations in (3.41) - (3.45) as the abstract model

$$\mathcal{M}(\boldsymbol{\mathcal{U}}, \mathbf{G}) = \mathbf{0} \tag{3.46}$$

implying that, given a specified shear moduli $\mathbf{G}$, we can obtain a corresponding displacement $\boldsymbol{\mathcal{U}}$ through the model $\mathcal{M}$.

To apply the SROM stochastic optimization approach developed previously, we will work with a discrete form of the model in (3.46). Here, we use the finite element method (FEM) for the discretization but note that in general other methods (finite difference, spectral methods, etc.) could be used. Using the FEM, we assume a solution of the form

$$\boldsymbol{\mathcal{U}}^h = [N]\mathbf{U} \tag{3.47}$$

where $[N]$ is a matrix of FEM basis functions and $\mathbf{U} \in \mathbb{R}^n$ is a vector of displacement values at the nodes of a numerical grid. Using this discrete approximation, the governing equations in (3.41) - (3.45) can be transformed into the following algebraic system of equations

$$\mathbf{M}(\mathbf{U}, \mathbf{G}) = [A(\mathbf{G})]\mathbf{U} - \mathbf{f} = \mathbf{0} \tag{3.48}$$

where

$$[A(\mathbf{G})] = [K(\mathbf{G})] - \omega^2[M] \tag{3.49}$$

and the stiffness matrix $[K]$, mass matrix $[M]$, and force vector $\mathbf{f}$ are given by

$$[M] = \sum_{\text{elements}} \int_{\mathcal{D}^e} \rho \, [N]^T \, [N] \, d\mathcal{D} \tag{3.50}$$

$$\begin{aligned} [K(\mathbf{G})] &= \sum_{i=1}^{d} G_i \left(\sum_{e \in \mathcal{D}_i} \int_{\mathcal{D}_i^e} [B]^T \, [D_s] \, [B] \, d\mathcal{D} \right) + b \int_{\mathcal{D}^e} [B]^T \, [D_v] \, [B] \, d\mathcal{D} \\ &\equiv \sum_{i=1}^{d} G_i \, [H_i] + b \, [J] \end{aligned} \tag{3.51}$$

$$\mathbf{f} = \sum_{\text{elements}} \int_{\Gamma_t^e} [N]^T \, \boldsymbol{\tau} \, dS \tag{3.52}$$

Here, $[B]$ is a matrix containing the derivatives of the FEM basis functions and $[D_s]$ and $[D_v]$ are matrices that separate the deviatoric and volumetric components of the stiffness matrix, respectively. Note that here we have used the discrete material assumption to view the shear portion of the stiffness matrix as a sum of separate contributions from each material, with $e \in \mathcal{D}_i$ signifying a sum over the particular elements that fall within the part of the domain corresponding to material i. For the sake of brevity, we will omit the details of the conversion of Equations (3.41) - (3.45) to (3.48) using the FEM and simply refer the reader to [13, 2] for an illustration of this process.

3.4.2 The stochastic elastodynamics inverse problem

The inverse problem associated with the elastodynamics forward problem that we consider here consists of estimating unknown shear moduli $\mathbf{G}$ given statistical information about the displacements $\mathbf{U}$ in $\mathcal{D}$. Specifically, we assume that we are provided the moments of an observed displacement vector $\mathbf{V} \in \mathbb{R}^n$ at a finite number of locations in the domain

$$\langle V_i^r \rangle = \mathbb{E}[V_i^r], \; r = 1, ..., \bar{r}, \; i \in \mathcal{I}_m, \tag{3.53}$$

up to some order $\bar{r}$. Here, $\mathcal{I}_m$ represents the set of degrees of freedom in the discretized domain where moment data is available ($\mathcal{I}_m \subseteq [1, n]$). Furthermore, let $\mathbf{E}^r \in \mathbb{R}^n$ denote the vector of differences between the r^{th} moment of $\mathbf{V}$ and the computed displacement $\mathbf{U}$ from Equation (3.48) where

$$E_i^r(\mathbf{U}(\mathbf{G})) = \begin{cases} \left(\langle U_i^r(\mathbf{G})\rangle - \langle V_i^r\rangle\right), & \text{if } i \in \mathcal{I}_m \\ 0, & \text{otherwise} \end{cases} \tag{3.54}$$

From here, the inverse problem can be cast as a stochastic optimization problem where we seek the random shear moduli vector that minimizes the discrepancy between the observed and computed displacement moments. To this end, we define the following objective function

$$\begin{aligned} \mathcal{J}(\mathbf{U}(\mathbf{G})) &= \frac{1}{2}\sum_{r=1}^{\bar{r}}\sum_{i\in\mathcal{I}_m} |E_i^r(\mathbf{U}(\mathbf{G}))|^2 \\ &= \frac{1}{2}\sum_{r=1}^{\bar{r}} \|\mathbf{E}^r(\mathbf{U}(\mathbf{G}))\|_2^2 \end{aligned} \tag{3.55}$$

where

$$\|\mathbf{z}\|_2 = \sqrt{\mathbf{z}^T\mathbf{z}} \tag{3.56}$$

In the same fashion as the abstract problem in (3.19), the random material identification problem can now be posed as the following constrained stochastic optimization problem

$$\begin{aligned} &\underset{\mathbf{U},\mathbf{G}}{\operatorname{argmin}} \;\; \mathcal{J}(\mathbf{U}(\mathbf{G})) = \frac{1}{2}\sum_{r=1}^{\bar{r}} \|\mathbf{E}^r(\mathbf{U}(\mathbf{G}))\|_2^2 \\ &\text{such that: } \mathbf{M}(\mathbf{U},\mathbf{G}) = [A(\mathbf{G})]\mathbf{U} - \mathbf{f} = \mathbf{0} \end{aligned} \tag{3.57}$$

Note that the only dependence of $\mathcal{J}$ on $\mathbf{G}$ in this case is implicitly through $\mathbf{U}$, but this need not be the case in general. With the stochastic elastodynamics inverse problem assuming this form, the SROM optimization approach can be

readily applied to estimate $\mathbf{G}$. The details of this are provided in the following section.

3.4.3 SROMs for the inverse elastodynamics problem

We now illustrate how the proposed SROM-based optimization framework described in Section 3.3 can be used to solve the stochastic elastodynamics inverse problem (3.57). As described, we first assume an SROM approximation $\tilde{\mathbf{G}}$ to the unknown shear moduli vector $\mathbf{G}$ and corresponding displacement SROM $\tilde{\mathbf{U}}$. The uncertainty in the stochastic inverse problem can now be expressed in terms of the SROM parameters $\{\tilde{\mathbf{g}}\} \in \mathbb{R}^D$, $\{\tilde{\mathbf{u}}\} \in \mathbb{R}^N$, and $\mathbf{p} \in \mathbb{R}^m$, where, again, $D = d \times m$ and $N = n \times m$ are the dimensions of the SROM sample vectors.

Along the lines of Section 3.3.2, we use $\tilde{\mathbf{G}}$ and $\tilde{\mathbf{U}}$ to transform the optimization problem in (3.57) from stochastic to deterministic. First, the objective function is rewritten in terms of the SROM shear moduli parameters as

$$\hat{\mathcal{J}}(\{\tilde{\mathbf{g}}\}, \mathbf{p}) = \mathcal{J}(\{\tilde{\mathbf{u}}(\tilde{\mathbf{g}})\}, \mathbf{p}) = \frac{1}{2} \sum_{r=1}^{\bar{r}} \|\mathbf{E}^r(\{\tilde{\mathbf{u}}(\tilde{\mathbf{g}})\})\|_2^2 \tag{3.58}$$

where the displacement moments $\langle \tilde{\mathbf{U}}^r \rangle$ that appear in $\mathbf{E}^r$ (3.54) can be straightforwardly computed using the SROM moment estimate in Equation (3.14). Next, in a manner analogous to (3.22), the stochastic elastodynamics model constraint (3.48) can be decoupled using the SROMs as

$$\tilde{\mathbf{M}}^{(i)} = \mathbf{M}(\tilde{\mathbf{u}}^{(i)}, \tilde{\mathbf{g}}^{(i)}) = [A(\tilde{\mathbf{g}}^{(i)})]\tilde{\mathbf{u}}^{(i)} - \mathbf{f} = \mathbf{0}, \ i = 1, ..., m \tag{3.59}$$

Now, similar to (3.23), we can search for the SROM solution $\tilde{\mathbf{G}}^*$ to the original stochastic inverse problem in (3.57) as

$$\tilde{\mathbf{G}}^* \equiv \underset{\{\tilde{\mathbf{g}}\} \in \mathcal{G}, \, \mathbf{p} \in \mathcal{P}}{\operatorname{argmin}} \ \frac{1}{2} \sum_{r=1}^{\bar{r}} \|\mathbf{E}^r(\{\tilde{\mathbf{u}}(\tilde{\mathbf{g}})\})\|_2^2 \tag{3.60}$$

where $\mathcal{P}$ is defined in (3.24) and $\mathcal{G}$ is the set of shear moduli vectors with non-negative components

$$\mathcal{G} = \left\{ \{\tilde{\mathbf{g}}\} | \ \{\tilde{\mathbf{g}}\} \in \mathbb{R}^D, \ \ \mathbf{0} \leq \{\tilde{\mathbf{g}}\} \right\} \tag{3.61}$$

We now focus on obtaining expressions for the gradients of the objective function with respect to the unknown SROM parameters $\{\tilde{\mathbf{g}}\}$ and $\mathbf{p}$ as in (3.27) and (3.34). The latter, $\hat{\mathcal{J}}_{\mathbf{p}}$, is easily obtained by examining the derivative with respect to one component of the probability vector $p^{(k)}$ as follows

$$\begin{aligned} \hat{\mathcal{J}}_{p^{(k)}} &= \frac{1}{2} \sum_r \sum_i \left(\frac{\partial |E_i^r|^2}{\partial \langle \tilde{U}_i^r \rangle} \right) \left(\frac{\partial \langle \tilde{U}_i^r \rangle}{\partial p^{(k)}} \right) \\ &= \sum_r \sum_i (\langle \tilde{U}_i^r \rangle - \langle V_i^r \rangle)(\tilde{u}_i^{(k)}) \\ &= \sum_r (\mathbf{E}^r)^T \tilde{\mathbf{u}}^{(k)} \end{aligned} \tag{3.62}$$

where we have used a straightforward application of the chain rule and the simple linear dependence of the SROM moments (3.14) on $\mathbf{p}$.

Next, we work out the details of computing the gradient with respect to the SROM shear samples, $\hat{\mathcal{J}}_{\{\tilde{\mathbf{g}}\}}$, following the formulation in Section 3.3.3. We must first define the right hand side and coefficient matrix of the adjoint problems (3.31). The right hand side, $\mathcal{J}_{\tilde{\mathbf{u}}^{(k)}}$, can be defined component-wise as

$$\begin{aligned} \hat{\mathcal{J}}_{\tilde{u}_j^{(k)}} &= \frac{1}{2} \sum_r \sum_i \left(\frac{\partial |E_i^r|^2}{\partial \langle \tilde{U}_i^r \rangle} \right) \left(\frac{\partial \langle \tilde{U}_i^r \rangle}{\tilde{u}_j^{(k)}} \right) \\ &= \sum_r \left(E_j^r \right) \left(p^{(k)} r (\tilde{u}_j^{(k)})^{(r-1)} \right) \end{aligned} \tag{3.63}$$

To obtain the coefficient matrix for the adjoint problem, the derivative of the discretized model constraints (Eq. (3.59)) with respect to a particular SROM displacement sample is simply

$$[\tilde{\mathbf{M}}_{\tilde{\mathbf{u}}^{(k)}}^{(k)}] = [A(\tilde{\mathbf{g}}^{(k)})] \tag{3.64}$$

Furthermore, it is straightforward to see from Equations (3.49)-(3.51) that $[A] = [A]^T$ is symmetric. Hence, for the elastodynamics inverse problem we consider, the adjoint problems in (3.31) are given by

$$[A(\tilde{\mathbf{g}}^{(k)})]\tilde{\mathbf{w}}^{(k)} = -\mathcal{J}_{\tilde{\mathbf{u}}^{(k)}}, \text{ for } k = 1, .., m \tag{3.65}$$

where the coefficient matrix remains unchanged between the forward and adjoint problems.

With the adjoint variables obtained via (3.65), we need only the final expression for the gradient vector $\hat{\mathcal{J}}_{\tilde{\mathbf{g}}^{(k)}}$ in (3.32). Since the objective function in (3.55) has no explicit dependence on the unknown SROM parameters $\{\tilde{\mathbf{g}}\}$, the first term in the gradient vanishes ($\mathcal{J}_{\tilde{\mathbf{g}}^{(k)}} = \mathbf{0}, \ \forall k$) and we just need to define $\tilde{\mathbf{M}}^{(k)}_{\tilde{\mathbf{g}}^{(k)}}$. Using Equations (3.59) and (3.51) and considering the expression componentwise for clarity, we have

$$\tilde{\mathbf{M}}^{(k)}_{\tilde{g}_i^{(k)}} = \left[\frac{\partial A(\tilde{\mathbf{g}}^{(k)})}{\partial \tilde{g}_i^{(k)}}\right]\tilde{\mathbf{u}}^{(k)} = \left[\frac{\partial K(\tilde{\mathbf{g}}^{(k)})}{\partial \tilde{g}_i^{(k)}}\right]\tilde{\mathbf{u}}^{(k)} \tag{3.66}$$

$$= [H_i]\tilde{\mathbf{u}}^{(k)} \tag{3.67}$$

Therefore, we arrive at the following expression for a given component of the gradient $\hat{\mathcal{J}}_{\tilde{\mathbf{g}}^{(k)}}$

$$\hat{\mathcal{J}}_{\tilde{g}_i^{(k)}} = \left(\tilde{\mathbf{u}}^{(k)}\right)^T [H_i]^T \left(\tilde{\mathbf{w}}^{(k)}\right). \tag{3.68}$$

3.4.4 A note on random loading

In order to test the SROM optimization framework with multiple uncertainties, we will consider the case where the applied traction $\boldsymbol{\tau}$ is also random. Similar to the Equation (3.35), the discretized elastodynamics model in (3.48) now takes

the form

$$\mathbf{M}(\mathbf{U}, \mathbf{G}; \boldsymbol{\tau}) = [A(\mathbf{G})]\mathbf{U} - \mathbf{F}(\boldsymbol{\tau}) = \mathbf{0} \tag{3.69}$$

due to the dependence of the force vector on $\boldsymbol{\tau}$ in Equation (3.52). Likewise, after an SROM $\tilde{\boldsymbol{\tau}}$ has been formed for the random load, the decoupled model constraints using the SROM approximations are given by

$$\tilde{\mathbf{M}}^{(i,j)} = [A(\tilde{\mathbf{g}}^{(i)})]\tilde{\mathbf{u}}^{(k)} - \mathbf{f}(\tilde{\boldsymbol{\tau}}^{(j)}) = \mathbf{0} \tag{3.70}$$

where the indexing scheme (3.17) is implied for index k. The remaining modifications to the formulation needed to treat the additional random load follow straightforwardly from the developments in Section 3.3.4.

3.5 Numerical examples

The proposed SROM-based approach to the stochastic elastodynamics inverse problem described in the previous section was implemented using the optimization toolbox in MATLAB [18]. The implementation is based on the `fmincon` function for constrained nonlinear optimization, which accepts the objective function (3.58) and gradients (Eq. (3.62) and (3.68)) as arguments to solve the optimization problem in (3.57). As recommended for large-scale problems, the `'interior-point'` algorithm is selected, implementing a quasi-Newton approach with BFGS [20] Hessian approximation to solve the problem.

The stochastic inverse problem framework in MATLAB is used to solve three numerical examples of random material identification in elastodynamics. In Example 1, the random shear modulus of a single homogenous material is estimated using moment data of the displacement field throughout the domain.

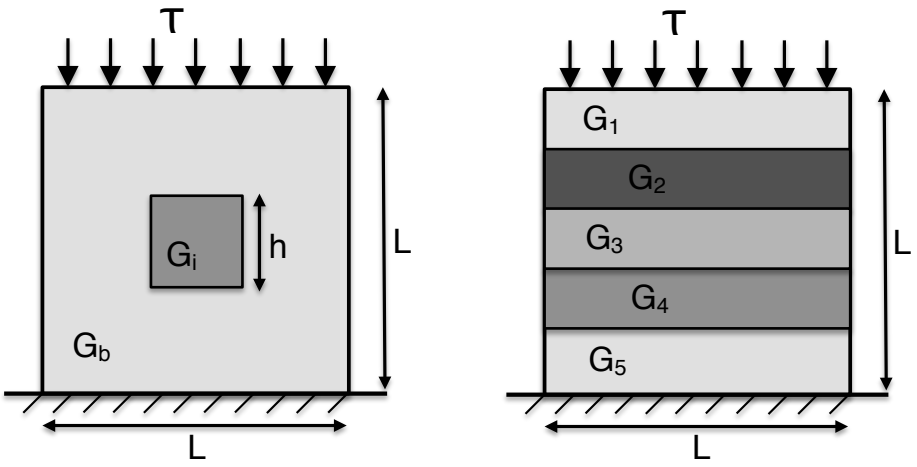

(a) (b)

Figure 3.1: Problem domains for the numerical examples.

This problem is solved considering both a deterministic and random loading and serves as an illustration of the performance of the framework and the convergence of solutions with respect to SROM size. Example 2 considers a random material with an interior inclusion and uses only sparse input data (i.e. on the boundary) to estimate the statistics of the background and inclusion shear moduli. In Example 3, a five-dimensional random vector of shear moduli is estimated in a domain comprised of layered materials under a random loading.

3.5.1 Example 1: Homogenous material

We consider a two-dimensional square domain with a single homogeneous material under plane strain conditions. We seek to recover the statistics of the random shear modulus using moments of the full displacement field as input data. We note that full field information is used in this case despite there being only one unknown for the sake of illustrating the properties of the method in a simple

setting, while problems with sparse data and multiple unknowns are presented subsequently. The problem is first solved for the case where the loading is deterministic and then for the situation when it is random. The performance of the method is studied for varying SROM sizes in both the shear modulus and the random load.

A sketch of the problem domain for this example can be seen in Figure 3.1(a), where we take $G_b = G_i \equiv G$, e.g. a homogeneous domain. We shall consider scaled and dimensionless quantities in this work for simplicity, where the domain is the unit square ($L = 1.0$). The density and bulk modulus are considered known and constant in the examples at $\rho = 1.0$ and $b = 8.33$, respectively. The domain is intentionally loaded at a low frequency of $f = 0.75$ to yield larger wavelengths and permit the use of relatively coarse computational grids for the solution of (3.48) with the FEM.

In this study, we choose to represent the random shear modulus using a scaled beta random variable. The beta distribution is a common and flexible choice for representing random variables with finite range. The shear modulus may then be expressed as

$$G = G_{\text{min}} + (G_{\text{max}} - G_{\text{min}})X_B \tag{3.71}$$

where X_B is a standard beta random variable with probability density given by

$$f(x_B; \beta_1, \beta_2) = \frac{x_B^{\beta_1 - 1}(1 - x_B)^{\beta_2 - 1}}{B(\beta_1, \beta_2)} \tag{3.72}$$

Here, $B(\beta_1, \beta_2)$ is the beta function. The mean and variance of X_B can be defined in terms of the parameters β_1 and β_2 as

$$\mathbb{E}[X_B] = \frac{\beta_1}{\beta_1 + \beta_2} \tag{3.73}$$

$$\text{Var}[X_B] = \frac{\beta_1 \beta_2}{(\beta_1 + \beta_2)(\beta_1 + \beta_2 + 1)} \tag{3.74}$$

Adopting this representation allows us to conveniently specify a target shear modulus in terms of the desired support ($G_{\text{min}}, G_{\text{max}}$) and mean and variance. From here, the parameters β_1 and β_2 are calculated from (3.73) and (3.74) and the resulting beta random variable is appropriately scaled using (3.71).

The displacement moment data (Eq. (3.53)) for this example is generated using Monte Carlo simulation. Here, $15,000$ independent samples of the shear modulus are drawn and each used to compute a corresponding displacement sample by solving Equations (3.41) - (3.45) using the finite element method on a uniform 15×15 grid. The first ten moments ($r = 10$) of the displacements are calculated from the Monte Carlo samples and then interpolated to a coarser 10×10 grid for the stochastic inverse problem. Both meshes are comprised of four-node, bilinear finite elements.

Deterministic load

The SROM approach is first used to solve the stochastic inverse problem in Eq. (3.57) when considering a deterministic loading of $\tau = 1.0$. The target shear modulus in this case has range $[G_{\text{min}}, G_{\text{max}}] = [4, 7]$ and a mean and variance of 5.0 and 0.25, respectively. The initial guess for the SROM $\tilde{G}$ in the optimization problem is samples $\{G\}$ drawn from a uniform distribution in $[G_{\text{min}}-1, G_{\text{max}}+1]$ with equal probability $p_i = 1/m_G, \ \forall i$. The optimization algorithm is terminated based on a tolerance on the relative change in objective function between iterations, specified as 10^{-4} in this case. The problem is solved for a range of SROM sizes m_G from 1 to 10.

First, we study the convergence of the inverse problem in terms of the be-

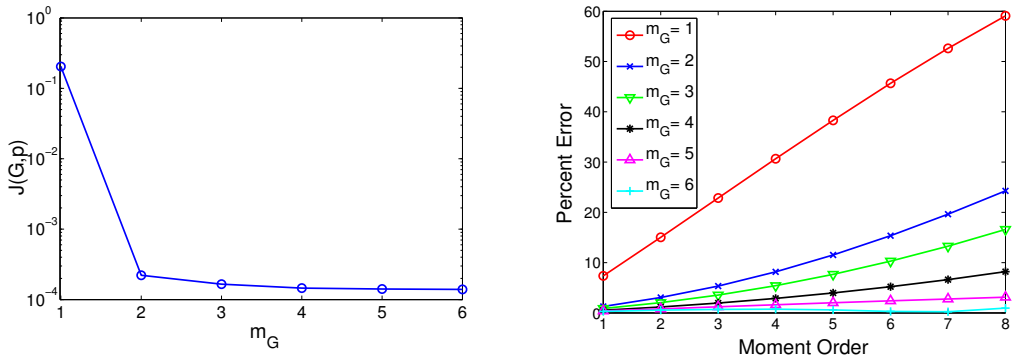

(a) (b)

Figure 3.2: The convergence of the SROM shear modulus approximation in Example 1 with deterministic load. (a) Minimized objective function (3.58) values versus SROM size. (b) The error in the SROM estimates of shear modulus moments for increasing SROM sizes.

havior of the objective function (Eq. (3.58)) for increasing SROM size in Figure 3.2(a). As expected, there is a decrease in minimized objective function value with increasing SROM size. A SROM $\tilde{G}$ with more parameters should be capable of better characterizing the randomness in G and hence producing computed displacements $\tilde{\mathbf{U}}$ that better match those given as input data. From Figure 3.2(a), it is seen that a relatively small number of samples and probabilities defining $\tilde{G}$ are able to produce a small discrepancy between computed and observed moments. Indeed, very little improvement in final objective function value is observed as the model size is increased from 3 to 6. We note that the large error for $m_G = 1$ is expected as in this case we are essentially approximating an unknown random quantity with a deterministic estimate (one sample $\tilde{G}_1$ with probability $p_1 = 1$). The number of iterations needed to obtain the minimum objective function values in Figure 3.2(a) are shown in Table 3.1, where, as expected, we see it takes an increasing number of iterations for termination as the SROM size is increased.

In Figure 3.2(b), we study the accuracy of the SROM approximations to the true moments of the shear modulus for increasing model sizes. Here, the first eight moments are estimated from $\tilde{G}$ using Equation (3.14) and the resulting percent errors with respect to the true beta-distributed shear modulus are plotted for $m_G = 1, ..., 6$. We observe a consistent decrease in moment error as the SROM size is increased, with the most stark improvement from a model size of 1 to 2. Here, the low-dimensionality of SROM uncertainty representations is clear, where it can be seen that surprisingly small model sizes yield accurate moment estimates. Indeed, $m_G = 6$ yields errors less than 1.0% for the first eight moments while SROMs with $m_G >= 2$ produce estimates of the first two moments within 3.0% of the true values.

Finally, we use the obtained SROM $\tilde{G}$ to estimate the distribution of the random shear modulus using Equation (3.13). Figure 3.3(a) shows the resulting error in the SROM CDF estimates versus model size, as computed by

$$e_{\text{CDF}} = \frac{\int_{-\infty}^{+\infty} \left(\tilde{F}_G(g) - F_G(g)\right)^2 dg}{\int_{-\infty}^{+\infty} \left(F_G(g)\right)^2 dg}, \tag{3.75}$$

while Figure 3.3(b) plots the actual CDF estimates versus the true distribution for three different SROM sizes. We observe a general decrease in error with

m_G	Iterations
1	20
2	42
3	83
4	92
5	94
6	126

Table 3.1: The number of iterations taken to obtain the minimum objective function values in Figure 3.2(a).

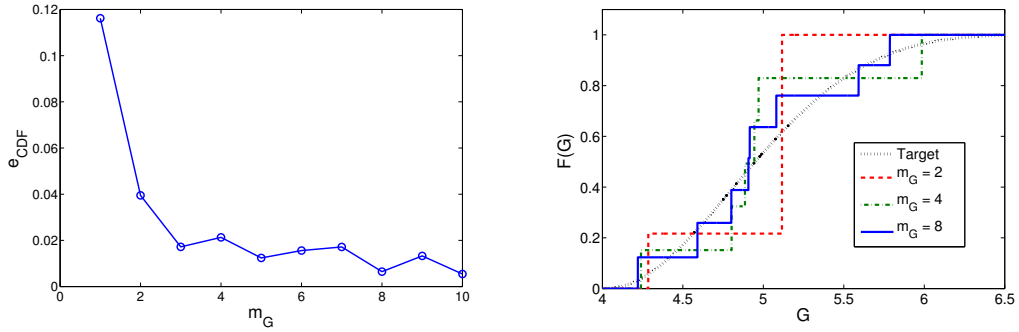

(a) (b)

Figure 3.3: SROM shear distribution accuracy for Example 1 with deterministic loading. (a) The CDF error (Eq. (3.75) versus SROM size. (b) Comparison of the SROM CDFs with the true shear distribution for different SROM sizes.

increasing m_G in (a) and see the corresponding improvement in distribution resolution in (b) when increasing the SROM size from 2 to 4 and from 4 to 8. As seen in Figure 3.3(a), however, the decrease in CDF error is not quite monotonic in this case. This is likely due to the existence of local minima in the objective function and the use of a gradient based optimizer whose solution is sensitive to the particular initial guess used. Overall, however, the SROM CDF estimates provide satisfactory characterizations of the true underlying distribution given the discrete nature of the approximations and relatively low number of parameters.

Random load

We now demonstrate the ability of the SROM optimization framework to handle multiple sources of uncertainty by considering random loading. Here, τ is taken to be a gamma random variable with mean 1.5 and variance 0.25 that is shifted to take a minimum value of 0.5. In this case, the unknown shear is again

beta-distributed but with $[G_{\min}, G_{\max}] = [4, 8]$ and a mean and variance of 6.0 and 0.25, respectively. The displacement moment data for the problem is generated in the same fashion as 3.5.1, using Monte Carlo simulation from 15,000 randomly drawn samples of τ and G. We study the performance of the method with varying SROM sizes for the load (m_τ) in addition to shear modulus (m_G).

The first step is to generate the SROM $\tilde{\tau}$ for the random load, which is done offline as a preprocessing step before the inverse problem solution. With the known expressions for the gamma random variable statistics, the SROM optimization problem in (3.23) for uncertainty propagation in forward models is solved to generate $\tilde{\tau}$ for a range of model sizes from 1 to 15. The distribution and moment error terms ((3.8) and (3.9)) are given equal weight in the objective function ($\alpha_1 = \alpha_2 = 1.0$). The convergence of the load SROM construction problem with increasing SROM size m_τ is shown in Figure 3.4. It is clearly seen that with further refinement of the load SROM, we are able to more closely approximate the statistics of the underlying random load. Note, however, that the computational cost of the inverse problem increases proportionally to the size of the SROM used.

With the SROM $\tilde{\tau}$ generated for the random load, the stochastic inverse problem (3.57) is solved to estimate the unknown shear modulus for different combinations of model sizes m_τ and m_G. The converged objective function (3.58) values versus m_G are plotted for different load SROM sizes m_τ in Figure 3.5. As was the case with the deterministic loading seen previously, the decrease in objective function is most pronounced from $m_G = 1$ to $m_G = 2$ and appears relatively unchanged for larger model sizes for each m_τ. It is also seen that the absolute minimum obtained by the objective function is decreased as the load

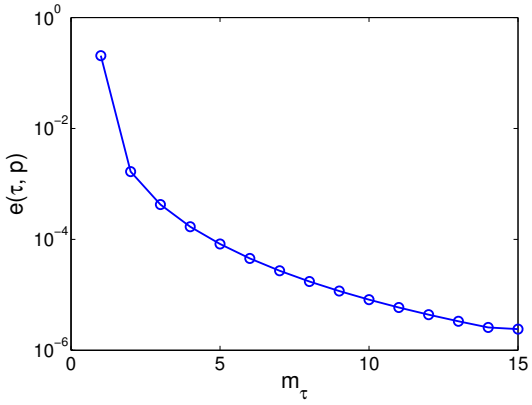

Figure 3.4: Convergence of the SROM construction problem (3.23) for forward uncertainty propagation with increasing SROM size when generating the SROM for the random load in Example 1.

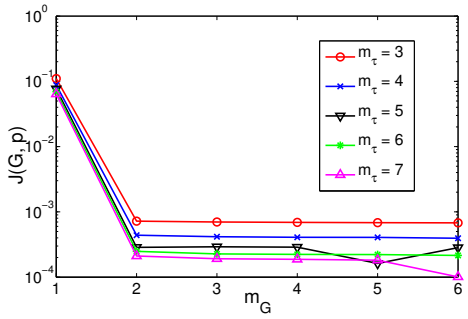

Figure 3.5: Converged objective function (3.58) values for different shear and load SROM sizes for Example 1 with random loading.

SROM size is increased from $m_\tau = 3$ to $m_\tau = 8$. This is intuitive as an accurate characterization of the random load is a prerequisite to being able to obtain computed displacements that effectively approximate the true observed values. Since both SROM approximations $\tilde{\tau}$ and $\tilde{G}$ contribute to the error observed in displacement moments $\mathcal{J}(\{\tilde{G}\}, \mathbf{p})$, we can control and reduce the contribution of $\tilde{\tau}$ to the error by increasing m_τ, at the added expense of more function evaluations per optimization iteration.

Figure 3.6 illustrates the accuracy of the SROM approximations of shear

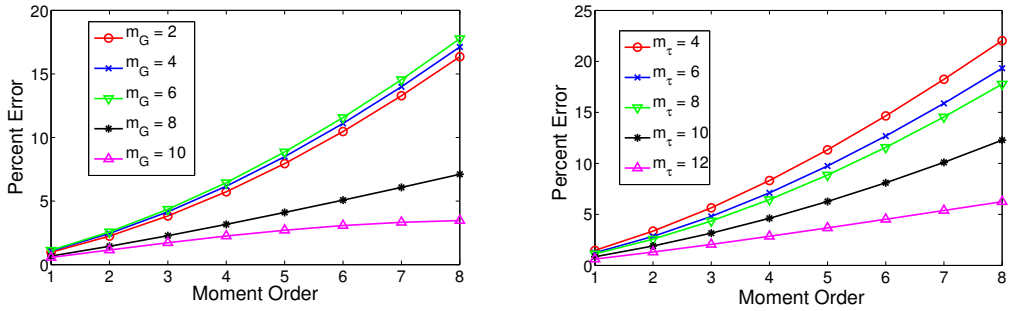

(a) (b)

Figure 3.6: SROM moment accuracy for Example 1 with random loading. a) Shear moment errors versus m_G for $m_\tau = 8$. b) Shear moment errors versus m_τ for $m_G = 4$.

modulus moments for this problem, with (a) plotting the moment estimate errors for increasing m_G with $m_\tau = 8$ fixed and (b) plotting the errors for increasing m_τ with $m_G = 6$ fixed. In Figure 3.6(a), the moment errors are of similar magnitude for $m_G = 2, 4, 6$ and then decrease significantly for the larger models, where $m_G = 10$ yields moment estimates up to order eight within 5% of the true values. Similarly, we see a general improvement in the moment estimates as the random load SROM $\tilde{\tau}$ is refined in Figure 3.6(b). Furthermore, if one is only interested in estimating the random shear modulus up to the first four moments, it can be seen that all combinations of m_G and m_τ depicted in the plots yield errors less than 10%.

In Figure 3.7, we view the accuracy of the SROM estimates of the shear modulus distribution function. Figure (a) plots the CDF error (Eq. 3.75) with increasing m_G for different load SROMs while (b) compares the SROM CDF approximation for different m_G to the true shear distribution with the load SROM size fixed at $m_\tau = 8$. Figure 3.7(a) provides a more comprehensive view of the trending accuracy in SROM approximations when increasing both m_G and m_τ, where it is seen that there is a general decrease in CDF error when refining ei-

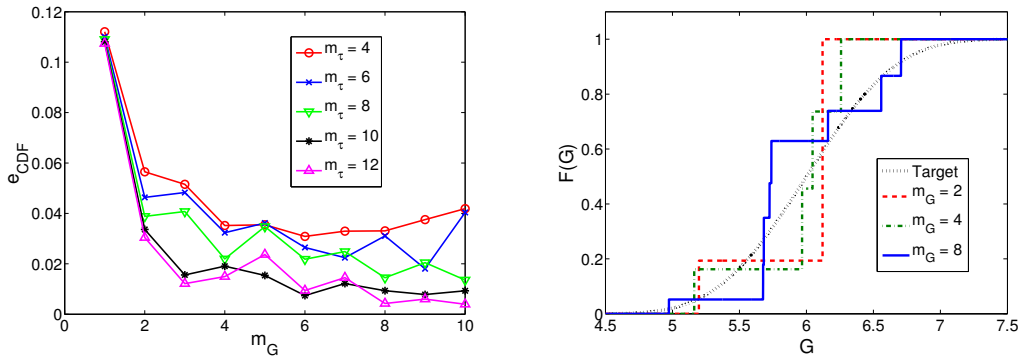

(a) (b)

Figure 3.7: SROM shear distribution accuracy for Example 1 with random loading. a) Shear CDF errors for different shear and load SROM sizes. b) CDF comparison for increasing m_G with $m_\tau = 8$.

ther of the models, $\tilde{G}$ or $\tilde{\tau}$. The improved accuracy with increasing m_G is shown more explicitly by comparing the three sample SROM CDFs in Figure 3.7(b). The discrete nature of the approximation is clearly improved with increased SROM parameters from $m_G = 2$ to $m_G = 8$.

As the primary purpose of this example was to study the performance of the SROM approach for varying-sized SROMs, $\tilde{G}$ and $\tilde{\tau}$, we now summarize with a couple observations on the results. We have generally seen convergence in the SROM approximations in the sense that the accuracy in the estimates of the unknown shear statistics improve with refinement of both the shear SROM $\tilde{G}$ and load SROM $\tilde{\tau}$ (i.e. increasing m_G and m_τ, respectively). The results show, however, that increasing the shear SROM size seems to have a smaller and less consistent impact on the solution accuracy as compared to increasing the load SROM size. This is apparent a number of ways: 1) the converged objective function value in Figure 3.5 is relatively stable for increasing m_G, while it is consistently lower as m_τ is increased, 2) the moment errors in Figure 3.6(b) decrease

monotonically with m_τ while this is not observed for m_G in Figure 3.6(a), and 3) the CDF estimate errors in Figure 3.7(a) show a relatively consistent accuracy trend for a fixed m_G and varying m_τ rather than visa versa.

We conjecture that the objective function may grow more complex with increasing number of optimization parameters (increasing m_G), resulting in more local minima, more sensitivity to initial guesses, and therefore less consistency in solution improvement with refinement of $\tilde{G}$. The SROM solutions corresponding to the true global minima of the objective function would likely show an accuracy trend closer to monotonicity with growing SROM size m_G. The employment of global optimization algorithms with this SROM framework is certainly a viable avenue for future research.

Gaussian noise model

In this section, we briefly demonstrate an alternative means of generating input data for the stochastic inverse problem using a Gaussian noise model and show the resulting performance of the SROM approach. This is convenient, for example, when we have only one realization of the system state variable with an estimate of the noise inherent in the observation, rather than explicit information about its statistics. The Gaussian noise assumption allows straightforward calculation of an arbitrary number of state moments to use as input data for the SROM inverse problem framework.

To test this approach, rather than assuming an explicit distribution for the random shear modulus and generating synthetic moment data using Monte Carlo simulation, a deterministic forward problem is first solved with a con-

stant shear modulus for the displacements $\hat{\mathbf{u}}$. Then, we assume the following Gaussian noise model for the synthetic displacement data

$$V_j = \hat{u}_j(1 + \delta R_j) \tag{3.76}$$

where R_j is a standard normal random variable and δ is the prescribed noise level on the data. The r^{th} displacement moment is then computed according to

$$\mathbb{E}[V_j^r] = (\hat{u}_j^r)\mathbb{E}[(1 + \delta R_j)^r] \tag{3.77}$$

For this problem, the shear modulus is specified as $G = 5.0$ and displacement moments up to order eight are computed using (3.77), with other parameters remaining unchanged from the previous examples. The inverse problem is solved for 1%, 5%, 10%, and 15% noise levels ($\delta = 0.01, 0.05, 0.1, 0.15$) and for shear SROM sizes $m_G = 5$ and $m_G = 10$. Although the target shear modulus has been specified deterministically, we are interested in how the prescribed measurement errors in the input data translate into uncertainty in the solution estimates. Since there is no explicitly known shear distribution for comparison, we instead study the general behavior of the SROM shear approximation as more measurement noise is present in the input data.

Figure 3.8 shows the SROM CDF estimate of the shear distribution for the different noise levels with (a) $m_G = 5$ and (b) $m_G = 10$. Here, the true shear value, $G = 5.0$, is denoted with the vertical dashed line. Noting the way that the SROM CDF range grows with higher noise levels, it is clear that the SROM effectively captures the growing uncertainty in the shear estimate as the variability in the input data increases. With 1% noise, for example, the SROM CDF is nearly aligned with the vertical line representing the true solution, whereas for 15% noise the CDF takes a wider range from about 4.5 to 5.5. This trend is

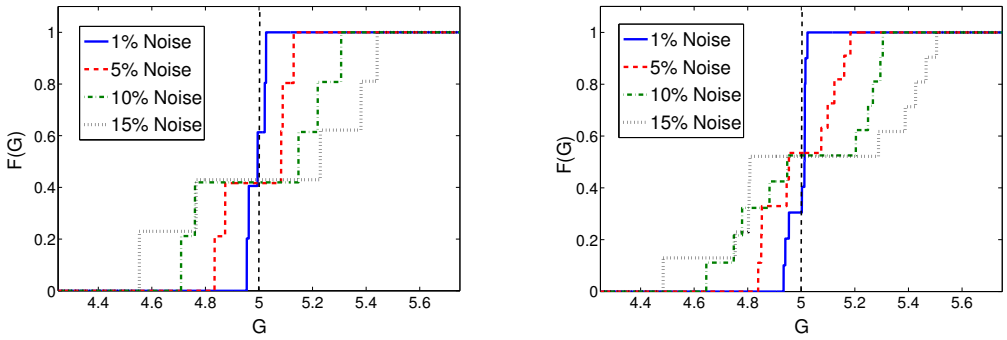

(a) (b)

Figure 3.8: SROM CDF estimates for the shear distribution using the Gaussian noise model (3.76) with different noise levels for (a) $m_G = 5$ and (b) $m_G = 10$. The vertical, dashed line reflects the true shear modulus value, $G = 5.0$.

further verified in Table 3.2, which shows the mean and variance estimates for shear modulus for the different noise levels. The SROM estimate for the mean is seen to be extremely accurate for all noise levels, while the increasing variance at each level is an accurate reflection of the growing uncertainty in the input data.

Noise	Mean	Variance
1%	4.991	0.001
5%	4.998	0.015
10%	5.019	0.061
15%	5.050	0.127

Table 3.2: SROM estimate for the mean and standard deviation for the true shear modulus $G = 5$ under the Gaussian noise assumption (3.76) for different levels of noise.

3.5.2 Example 2: Material with inclusion using sparse data

In this example, we consider a two dimensional domain comprised of a square material inclusion embedded in a softer background material, where both shear moduli are considered random and unknown. The goal of the problem is to estimate the statistics of the unknown moduli using only sparse displacement data on the boundary of the domain, mimicking a practical scenario where only surface measurements are feasible. The accuracy of the SROM estimates is studied in full for the case where explicit distributions are assumed for the unknown shear moduli, and then briefly demonstrated for the case where the Gaussian noise model (3.76) is assumed.

The problem domain is seen in Figure 3.1(a) where the geometry is specified by $L = 1.0$ and $h = 0.33$. The distributions for the unknown shear moduli in the background and inclusion materials, G_b and G_i, respectively, are specified again using Equations (3.71) - (3.74) with parameters shown in Table 3.3. The load is applied deterministically as $\tau = 1.0$. The synthetic displacement moment data is again generated with $15,000$ Monte Carlo samples, solving each forward problem on a 18×18 grid and interpolating onto a coarser 12×12 grid for the inverse problem. The first four ($r = 4$) moments are retained only along the boundary of the domain as input data for the problem.

	G_{min}	G_{max}	$\mathbb{E}[G]$	$\text{Var}[G]$
G_b	3.0	6.0	4.0	0.25
G_i	7.0	10.0	8.0	0.25

Table 3.3: The parameters describing the true shear moduli distributions for Example 2.

The inverse problem is initially solved to estimate $\mathbf{G} = [G_b \; G_i]^T$ with SROM sizes $m_G = 1, ..., 5$. The minimized objective function value for each size is shown in Figure 3.9(a) where we observe that the values decrease up to $m_G = 3$ before leveling off. Here, we will adopt the SROM $\tilde{\mathbf{G}}$ for $m_G = 4$ as the converged solution and proceed to illustrate the results for this case.

First, we view the errors in the first four moments for the background and inclusion shear modulus in Figure 3.9(b). We can see that using only boundary displacement information, we can approximate the first four moments of each modulus within 10% of the true values. If only interested in the mean estimates for the shear moduli, these values are predicted within 0.20% and 2.00% for the background and inclusion modulus, respectively. It is also clear that the estimate for G_b is significantly more accurate than that of G_i. This is likely due to the use of only surface measurements, where there is less sensitivity of this data to the interior inclusion shear modulus as compared to the background modulus.

Next, we compare the SROM approximations of the shear moduli CDFs to the true distributions in 3.9(c). We observe that the range of the background material is well-resolved while the spread of the inclusion material is underestimated, which again may be attributed to a lack of sensitivity to the boundary input data used. However, it can be seen that the means of the distributions appear well-approximated, as was confirmed previously in the moment errors.

Lastly, this example was solved using the Gaussian noise model (3.76) for the input data. This version of the problem could represent an experimental set up in which the displacements are measured just once on the surface of the material being imaged, but we also have a notion of the level of error associated with

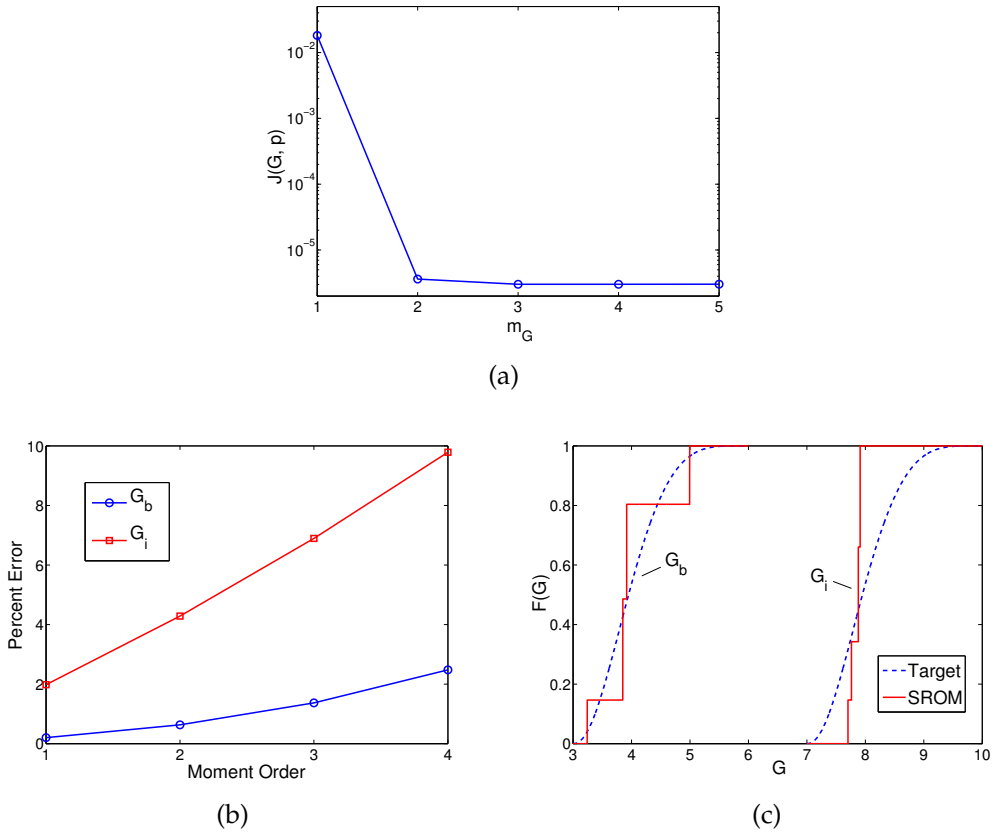

Figure 3.9: Results for Example 2 with explicit unknown distributions for the shear moduli. (a) The convergence of the objective function for increasing SROM size m_G. (b) The percent errors in the SROM moment estimates for the background and inclusion shear moduli with $m_G = 4$. (c) The SROM shear modulus CDFs for $m_G = 4$ compared to the true distributions.

the measurement. The inverse problem is solved for 10% and 20% prescribed noise levels and the results are summarized in Table 3.4. Here, we show the SROM mean approximation with plus/minus two standard deviation intervals for $m_G = 4$. For both noise levels, we see that the mean estimates are very accurate with respect to the true values ($G_b = 4.0$ and $G_i = 8.0$). Also apparent is the increasing uncertainty in the SROM estimate with growing noise, a positive and expected behavior, as the standard deviation intervals in the plot become considerably larger from 10% to 20% noise.

3.5.3 Example 3: Layered materials with random force

This example demonstrates the effectiveness of the SROM optimization framework in problems with higher dimensional random funknowns as well as additional system uncertainties. Here, we seek to recover a five-dimensional random vector of shear moduli in a domain under random loading. In doing so, we illustrate the accuracy of the SROM approach for problems with higher dimensional random spaces. We also include results for the case when there is a practical limitation on the number of model evaluations possible, demonstrating the efficiency of the method in obtaining satisfactory moduli estimates with relatively low computational cost.

A diagram of the domain for this problem can be seen in Figure 3.1(b). Again, we consider a unit square domain ($L = 1.0$), but here it is comprised of five layers of material all characterized by a different random shear modulus. The true shear modulus distributions for each material are given in Figure 3.10, where the defining parameters have been chosen as to create significant variability among the different moduli. The loading τ is random and is consistent with that of Example 1 - gamma distributed with mean 1.5, variance of 0.25, and

		$\mathbb{E}[G]$	$-/+2$ STD
10% noise	G_b	4.02	$(3.66, 4.38)$
	G_i	7.88	$(7.55, 8.22)$
20% noise	G_b	4.09	$(3.23, 4.96)$
	G_i	7.82	$(7.11, 8.53)$

Table 3.4: The SROM mean approximations and minus/plus two standard deviation intervals in Example 2 with 10% and 20% noise. The SROM size is $m_G = 4$ and the target shear moduli values are $G_b = 4.0$ and $G_i = 8.0$.

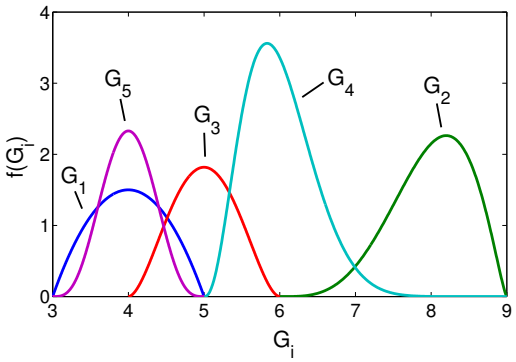

Figure 3.10: The true shear modulus distributions for Example 3.

a minimum value of 0.5. Monte Carlo simulation is again used to generate the first four moments of the full displacement field for input data. The forward problem is solved on a 15×15 grid and interpolated to a 10×10 grid for the inverse problem. Here, $25,000$ samples are used for the Monte Carlo estimates to ensure the moment accuracy given the added number of random variables.

Random shear moduli vector SROM estimates

The inverse problem is initially solved for $\tilde{\mathbf{G}}$ with model sizes $m_G = 1, ..., 5$ as well as varying load SROM sizes $m_\tau = 4, 6, 8$. The convergence of the SROM shear solution is demonstrated in Figure 3.11(a), showing the final minimized objective function (3.58) values as a function of m_G for the different m_τ values. It can be seen that the errors appear to stabilize for a shear SROM size $m_G = 3$ and a load SROM size $m_\tau = 8$. Therefore, we focus mainly on the SROM estimate $\tilde{\mathbf{G}}$ formed from this combination of sizes in the following results.

The accuracy of the SROM shear moment estimates with $m_G = 3$ is demonstrated in Figure 3.11(b). Here, the average and maximum moment error across the five unknown shear moduli is shown for $m_\tau = 4, 6, 8$. Again, the improve-

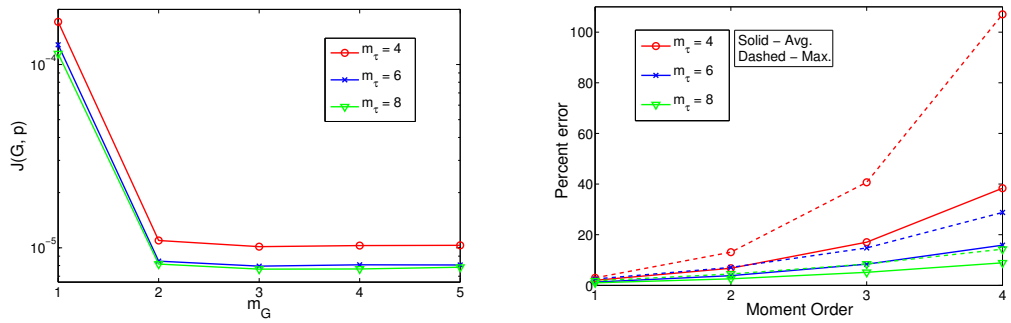

(a) (b)

Figure 3.11: (a) Converged objective function values versus m_G for different m_τ. (b) The maximum and average percent error in the SROM moment estimates for $m_G = 3$ and different m_τ.

ment in overall solution quality as m_τ increases is clear in the plot, most notably with the maximum error in the fourth moment decreasing from 107.0% to just 14.3% for $m_\tau = 4$ and $m_\tau = 8$, respectively. For the solution deemed as converged from Figure 3.11(a) ($m_G = 3$ and $m_\tau = 8$), the moment estimates using $\tilde{\mathbf{G}}$ are very accurate. Indeed, the average moment error across the unknown moduli is under 9.0% for all four moments and is just 1.0% and 2.6% for the first and second moment, respectively. This accuracy is seen in more detail in Figure 3.12, which compares the SROM estimates of the first four moments to the true shear moduli moments for $m_G = 3$ and $m_\tau = 8$. The SROM estimates nearly coincide with the true shear moduli that take smaller values while there is just a small discrepancy in the larger moduli approximations.

Solutions with limited model evaluations

To demonstrate the computational efficiency of the SROM optimization approach, we now briefly show results for the case where there is a limit on the number of forward model evaluations allowed to obtain a solution. Note that

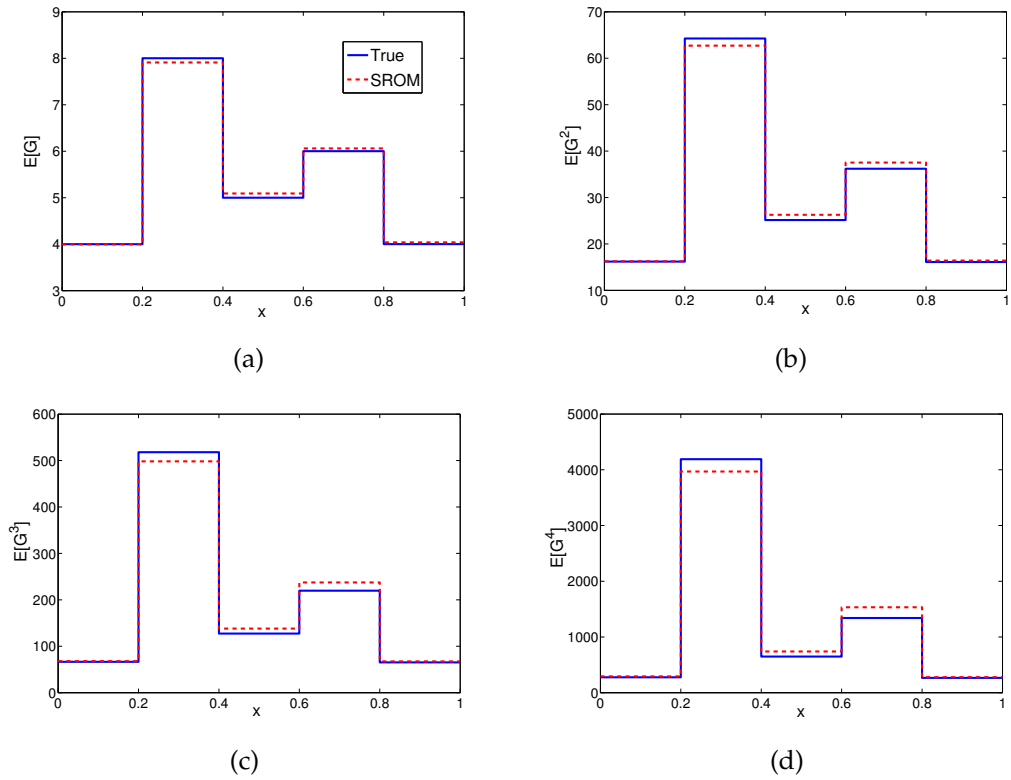

Figure 3.12: Comparison of the SROM estimates for the first four moments versus the true values with $m_G = 3$ and $m_\tau = 8$.

the results shown thus far were generated by terminating the optimization algorithm according to a tolerance on the relative change in the objective function. Due to the simplicity of the elastodynamics forward model considered here, we could afford to choose a stringent stopping tolerance to guarantee the accuracy of the solutions. However, in many problems of practical importance, the number of calls to the deterministic simulator is limited by the complexity of the governing model (3.1). Hence, to mimic this scenario, we revisit this example where we instead terminate the optimization algorithm according to a prescribed maximum number of model evaluations.

From the formulation in Section 3.3.4, the total number of forward model

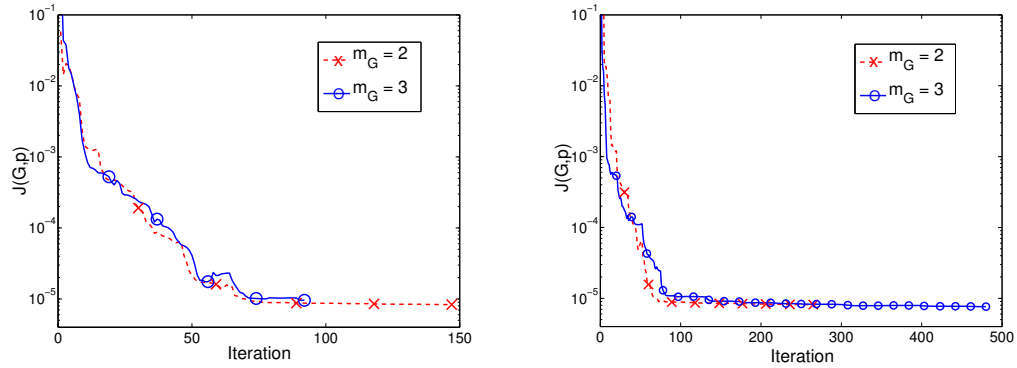

(a) (b)

Figure 3.13: Convergence of the objective function when a) terminating the optimization algorithm according to a maximum number of model evaluations (Section 3.5.3) and b) terminating the algorithm with a strict tolerance on the relative change in objective function (Section 3.5.3). The markers appear on the curves for approximately every 1000 solves.

evaluations to obtain an SROM optimization solution can be expressed as

$$\#\text{ model evaluations} = (2 \times m_G \times m_\tau) \times (\#\text{ objective function evaluations}) \tag{3.78}$$

assuming that the gradient computation is also carried out with each call to the objective function. Hence, given a prescribed number of allowed simulations, we can supply the optimization algorithm with the corresponding number of objective function evaluations at which to terminate using this relation. In this case, we solve the problem for $m_\tau = 8$, $m_G = 2$ and 3, and # model evaluations = $\{1000, 2000, 3000, 4000, 5000\}$.

First, we view the convergence of the objective function with limited model evaluations in Figure 3.13(a), where the markers on the curves represent approximately every 1000 forward solves, up to the maximum of 5000. For comparison, the same plot is shown from the results in the previous section in Figure 3.13(b), when the algorithm terminated according to a strict tolerance on the

relative change in objective function. It is clear from the two plots that accurate solutions can be obtained with far fewer iterations and model evaluations than were carried out previously. Indeed, for the case of $m_G = 3$, the objective function appears relatively unchanged over the last 300 iterations before reaching the stopping criteria in Figure 3.13(b).

Also apparent in Figure 3.13(a) is that using $m_G = 2$ results in a lower objective function value as compared to $m_G = 3$ for the same number of model evaluations. The primary reason, as apparent from the relation in (3.78), is that a smaller model size requires fewer forward solves per iteration of the optimization algorithm and hence more iterations may be carried out for the same number of model evaluations. This is clear in Figure 3.13(a) as well, where for 5000 model evaluations, the optimization algorithm is able to proceed for 144 iterations for $m_G = 2$ and only 92 for $m_G = 3$. Note that the number of iterations need not correspond exactly with the number of objective function evaluations, as line search or trust region optimization algorithms [20] may require multiple calls to the objective function on a single iteration.

It is insightful to now view the errors in the shear moment estimates as a function of the number model evaluations. Figure 3.14 shows the average moment error across the five shear moduli versus number of model evaluations for a) $m_G = 2$ and b) $m_G = 3$. As was also apparent in Figure 3.13(a), the errors here for $m_G = 2$ are substantially lower than using $m_G = 3$ with the same number of model evaluations. For example, it can be seen that it takes 4000 deterministic model solves to reduce the average error in the first four moments under 20% with $m_G = 3$, while it takes just 2000 when $m_G = 2$. In each case, however, it takes relatively few solves to yield satisfactory results. When concerned with

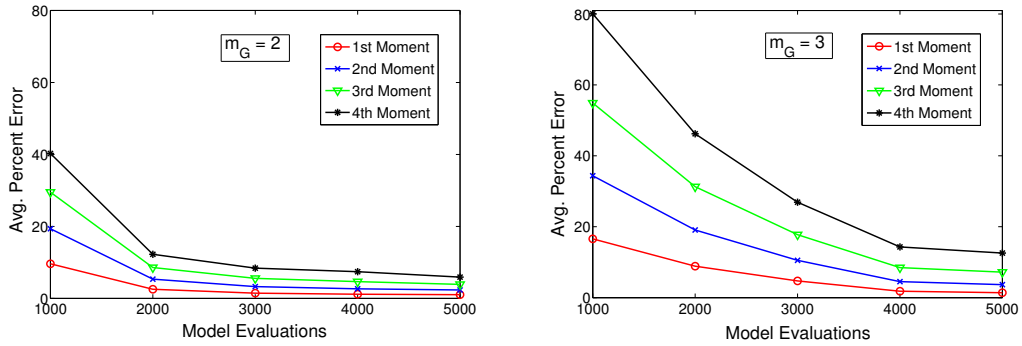

(a) (b)

Figure 3.14: The average percent error in the SROM moment estimates versus number of model evaluations for a) $m_G = 2$ and b) $m_G = 3$.

second moment accuracy, it takes just 3000 and 4000 solves to obtain estimates within 5% of the true values on average for $m_G = 2$ and $m_G = 3$, respectively.

In summary, this example illustrates one of the main strengths of the SROM optimization approach - the ability to yield accurate results in a computationally efficient manner (i.e. with limited calls to the deterministic model). Here, satisfactory solution estimates were obtained for a problem with a six-dimensional stochastic space with just 5000 or less forward solves. It is important to reemphasize the independence of the necessary model evaluations and potential scalability of the method with parallel processing. With access to a computing cluster, one can easily perform the SROM optimization framework on $m_G \times m_\tau$ processors and perform all necessary forward and adjoint solves in roughly the time it takes for two simulations.

3.6 Conclusion

In this study, we proposed a novel framework for inverse problems under uncertainty using stochastic reduced order models (SROMs). Viewing the inverse problem generally as a constrained stochastic optimization problem, the approach was formulated in terms of minimizing an abstract objective function with stochastic model constraint. The low-dimensional, non-intrusive nature of the SROM approximation transforms the constrained stochastic optimization problem into a deterministic one over relatively few parameters with decoupled, deterministic model constraints. In this way, the use of SROMs allows for a widely applicable method that relies solely on calls to existing deterministic forward solvers and standard optimization software. Furthermore, since the necessary forward model evaluations are completely independent from one another, the approach could be easily parallelized and hence scalable to large design and inverse problems. Finally, the SROM-based approach naturally handles problems with multiple sources of uncertainty.

We demonstrated the effectiveness of the proposed SROM inverse problem framework on the problem of random material identification in elastodynamics systems. We showed, through numerical examples, that the approach could accurately and efficiently estimate the statistics of random, unknown shear moduli in an elastic solid given moments of displacements as input data. Moreover, the method was shown to remain effective in the situation where there is only sparse input data available as well as cases where the loading in the problem can only be characterized probabilistically. Lastly, the SROM approach was shown to be capable of satisfactorily estimating several random unknowns with relatively limited calls to the forward solver, in large part due to the low-

dimensionality of the models.

3.7 Acknowledgments

James Warner and Wilkins Aquino were partially supported by the CSAR Program at Sandia National Laboratories and NIH grant# EB 002167

REFERENCES

[1] I. Babuska, F. Nobile, and R. Tempone. A stochastic collocation method for elliptic partial differential equations with random input data. Technical report.

[2] K. J. Bathe. *Finite Element Procedures*. Prentice Hall, Pearson Education, Inc., USA, 2006.

[3] B. Ganapathysubramanian and N. Zabaras. A scalable framework for the solution of stochastic inverse problems using a sparse grid collocation approach. *Journal of Computational Physics*, 227:4697–4735, 2008.

[4] R. G. Ghanem and P. D. Spanos. *Stochastic Finite Elements: A Spectral Approach*. Springer–Verlag, New York, 1991.

[5] M. Grigoriu. *Stochastic Calculus. Applications in Science and Engineering*. Birkhäuser, Boston, 2002.

[6] M. Grigoriu. Reduced order models for random functions. application to stochastic problems. *Applied Mathematical Modelling*, 33:161–175, 2009.

[7] M. Grigoriu. Effective conductivity by stochastic reduced order models (sroms). *Computational Materials Science*, 50:138–146, 2010.

[8] M. Grigoriu. Linear random vibration by stochastic reduced-order models. *International Journal for Numerical Methods in Engineering*, 82:1537–1559, 2010.

[9] M. Grigoriu. Solution of linear dynamic systems with uncertain properties by stochastic reduced order models. *Probabilistic Engineering Mechanics*, 34:168–176, 2013.

[10] M. D. Gunzburger. *Perspectives in Flow Control and Optimization (Advances in Design and Control)*. SIAM, Philadelphia, PA, 2002.

[11] E. Haber and L. Hanson. Model problems in pde-constrained optimization. Technical report.

[12] M. Hinze, R. Pinnau, M. Ulbrich, and S. Ulbrich. *Optimization with PDE Constraints*. Springer, New York, 2009.

[13] T. J. R. Hughes. *The finite element method: linear static and dynamic finite element anaysis*. Dover Publications, Inc., Mineola, New York, USA, 2000.

[14] D. P. Kouri, M. Heinkenschloss, D. Ridzal, and B. G. Van Bloemen. A trust-region algorithm with adaptive stochastic collocation for pde optimization under uncertainty.

[15] P. S. Koutsourelakis. A novel bayesian strategy for the identification of spatially varying material properties and model validation: an application to static elastography. *Int. J. Numer. Meth. Engng*, 91:249–268, 2012.

[16] X. Ma and N. Zabaras. An efficient bayesian inference approach to inverse problems based on an adaptive sparse grid collocation method. *Inverse Problems*, 25:035313. 27pp, 2009.

[17] Y. Marzouk and D. Xiu. A stochastic collocation approach to bayesian inference in inverse problems. *Communications in Computational Physics*, 6(4):826–847, 2009.

[18] The MathWorks Inc., Natick, Massachusetts. *MATLAB Version 7.10.0 (R2010a)*, 2010.

[19] V. A. B. Narayanan and N. Zabaras. Stochastic inverse heat conduction using a spectral approach. *Int. J. Numer. Meth. Engng*, 60:1569–1593, 2004.

[20] J. Nocedal and S. Wright. *Numerical Optimization*. Springer, 2006.

[21] S. Sarkar, J. E. Warner, W. Aquino, and M. Grigoriu. Stochastic reduced order models for uncertainty quantification of intergranular corrosion rates. *Corrosion Science*, 80:257–268, 2014.

[22] J. Wang and N. Zabaras. A bayesian approach to the inverse heat conduction problem. *International Journal of Heat and Mass Transfer*, 47:3927–3941, 2004.

[23] J. E. Warner, M. Grigoriu, and W. Aquino. Stochastic reduced order models for random vectors. application to random eigenvalue problems. *Probabilistic Engineering Mechanics*, 31:1–11, 2013.

[24] N. Wiener. The homogenous chaos. *American Journal of Mathematics*, 60:897–936, 2009.

[25] D. Xiu and S. Hesthaven. High-order collocation methods for the differential equation with random inputs. *SIAM J. Sci. Comput.*, 27:1118–1139, 2005.

[26] D. Xiu and G. E. Karniadakis. The weiner-askey polynomial chaos for stochastic differential equations. *SIAM Journal of Scientific Computing*, 24(2):619–644, 2002.